2017

Electromagnetic Signal Feedback Control For Proximity Detection Systems

Adam K. Smith
Michigan Technological University, adamsmit@mtu.edu

ELECTROMAGNETIC SIGNAL FEEDBACK CONTROL FOR PROXIMITY DETECTION SYSTEMS

By
Adam K. Smith

A DISSERTATION
Submitted in partial fulfillment of the requirements for the degree of
DOCTOR OF PHILOSOPHY
In Mechanical Engineering – Engineering Mechanics

MICHIGAN TECHNOLOGICAL UNIVERSITY
2017

This dissertation has been approved in partial fulfillment of the requirements for the Degree of DOCTOR OF PHILOSOPHY in Mechanical Engineering – Engineering Mechanics.

Department of Mechanical Engineering – Engineering Mechanics

Dissertation Advisor: *Dr. Nina Mahmoudian.*

Committee Member: *Dr. Mo Rastgaar*

Committee Member: *Dr. Gordon G. Parker*

Committee Member: *Dr. RJ Matetic*

Department Chair: *Dr. William W. Predebon*

Dedication

To Savannah

Never stop dreaming, always explore the unknown, and embrace life's challenges.

Table of Contents

List of Figures

List of Tables

Preface

Reference herein to any specific commercial company, product, process, or service by trade name, trademark, manufacturer, or otherwise, does not necessarily constitute or imply its endorsement, recommendation, or favoring by the United States Government or the National Institute for Occupational Safety and Health (NIOSH). The opinions of the author expressed herein do not necessarily state or reflect those of the United States Government or the NIOSH, and shall not be used for advertising or product endorsement purposes.

Acknowledgements

I would like to recognize the support I have received from the Office of Mine Safety and Health Research. Colleagues and fellow researchers in the Electrical and Mechanical Systems Safety Branch provided valuable technical information and administrative support. Specifically, I would like to thank Mr. Peter Kovalchik. He has been a constant source of wisdom and encouragement throughout my various career endeavors.

I would also like to also thank my advisory committee for the support and advice I have received from them. Dr. Nina Mahmoudian provided critical technical consultation and guidance on this research topic. She was a source of inspiration and motivation throughout the dissertation process. Dr. Rastgaar and Dr. Parker provided much needed perspective as research was being conducted. Dr. RJ Matetic has provided me with continual support throughout my career, and I sincerely thank him for serving on my committee.

The Mechanical Engineering - Engineering Mechanics administrative staff
at the Michigan Technological University needs to be especially recognized. Being a distance student pursuing an advanced degree brings forth many challenges and obstacles. I would like to thank Dr. Craig Friedrich and the department staff for helping me through this process.

Lastly, I would like to thank my close friends and family. I am extremely lucky to have a network of amazing people that have nurtured and supported me throughout my life. Without the support of my immediate family, none of this would have been possible. Finally, my daughter Savannah is an inspirational source of curiosity and wonder that perpetually inspires me.

Abstract

Coal is the most abundant fossil fuel in the United States and remains an essential source of energy. While more than half of coal production comes from surface mining, nearly twice as many workers are employed by underground operations.

One of the key pieces of equipment used in underground coal mining is the continuous mining machine. These large and powerful machines are operated in confined spaces by remote control. Since 1984, 40 mine workers in the U. S. have been killed when struck or pinned by a continuous mining machine. It is estimated that a majority of these accidents could have been prevented with the application of proximity detection systems.

While proximity detection systems can significantly increase safety around a continuous mining machine, there are some system limitations. Commercially available proximity warning systems for continuous mining machines use magnetic field generators to detect workers and establish safe work areas around the machines. Several environmental factors, however, can influence and distort the magnetic fields. To minimize these effects, a control system has been developed using electromagnetic field strength and generator current to stabilize and control field drift induced by internal and external environmental factors.

A laboratory test set-up was built using a ferrite-core magnetic field generator to produce a stable magnetic field. Previous work based on a field-invariant magnetic flux density model, which generically describes the electromagnetic field, is expanded upon. The analytically established transferable shell-based flux density distribution model is used to experimentally validate the control system. By controlling the current input to the ferrite-core generator, a more reliable and consistent magnetic field is produced. Implementation of this technology will improve accuracy and performance of existing commercial proximity detection systems. These research results will help reduce the risk of traumatic injuries and improve overall safety in the mining workplace.

Chapter 1: Introduction

This work will expand upon previous research efforts to improve the performance of proximity detection systems used in underground coal mining. The first chapter examines the issues of safety and health in the mining industry, specifically in underground coal mining. Chapter 1 also reviews proximity detection technologies and systems currently being applied to the mining industry.

Chapters 2 and 3 develop theoretical and experimental electromagnetic proximity detection. Fundamental proximity detection systems components are introduced in Chapter 2. The governing equations that describe magnetic field generation and detection is reviewed, and the magnetic shell model is developed. Position triangulation is theoretically established through the application of a 2 generator system. Chapter 3 describes the experimental system that is used to demonstrate electromagnetic proximity detection in a laboratory environment. The magnetic fields produced by the experimental system are used to validate the magnetic shell model and demonstrate position triangulation. The influence of temperature on the performance of the experimental system is also investigated.

The next two chapters develop and demonstrate a control system approach to limit environmental influences observed on the experimental system. A numerical model of the experimental system is established in Chapter 4. A control system is developed to reduce the environmental influences identified in Chapter 3. Different approaches are contrasted and discussed to meet the experimental system requirements. Finally, the control system is experimentally implemented and demonstrated in Chapter 5.

The remaining chapter summarizes the contribution of this work. Conclusions and limitations of this study are examined. Future investigations are also considered.

1.1: Mine Worker Safety and Health

A large part of the energy and raw materials that feed the U.S. economy comes from mining. Copper for electronic products, bauxite for aluminum, and coal for energy generation are just a few examples of how mined commodities are used by modern society. Extracting and processing mined commodities has become increasingly complex and demanding for workers over the last century.

This inherently dangerous industry has historically had some of the highest rates of fatality and injury. During the first part of the last century, more than 1,000 fatal injuries were occurring every year within the mining industry [1]. With the introduction of improved mining methods, regulations, and technology, fatal injury rates have decreased to less than 200 annually in recent years. However, fatal injury rates in mining remain more than four times higher than the average for all other industries [2]. Nonfatal occupational injuries and illness rates are less than in private industry, but are nonetheless a major concern for mine workers due to respiratory diseases and musculoskeletal disorders [3]. This same general trend of fatalities, injuries, and illnesses for the overall mining industry sector can also be observed in the coal industry.

Over the last century, the U.S. government has promulgated legislation aimed at improving the safety and health of coal mine workers. At the turn of the 20th century, there were a number of historic coal mining disasters that resulted in significant loss of life. A series of underground coal mine explosions led to the formation of the U.S. Bureau of Mines (BOM) in 1910, and eventually the creation of the Mine Safety and Health Administration (MSHA) in 1977 [4, 5]. As postmortem medical toxically evolved, it was realized through examination of the victims of various underground coal mine explosions that pneumoconiosis (black lung disease) is a substantial health concern for mine workers. This, along with other mitigating factors, eventually led Congress to pass the 1969 Coal

Act, which drastically increased federal enforcement powers in U.S. coal mines. After the legislation passed, the coal mining fatality rate dropped by 50%, from 202 to 103 fatalities per 100,000 full-time employees in the late 1960s and early 1970s [6].

During the 1980s and 1990s, coal mining research efforts in the U.S. continued to focus on regulation and enforcement. The initial development of mining technology and systems that could reduce worker exposure to underground hazards began to show potential [7, 8]. Reducing fatalities and improving mine worker health continued to be a primary focus. However, refinement and application of new mining methods, procedures, and technologies began to be integrated through the industry. As production and consumption continued to increase, so did mine worker safety [9].

More recently, the U.S. MINER Act was passed by Congress in 2006 to further advance health and safety efforts in the mining industry. The Mine Improvement and New Emergency Response (MINER) Act was drafted in response to tragedies that occurred at the Sago, Aracoma, and Darby coal mines [10]. The law further improves U.S. coal mine safety through increased mandatory training, upgrading mining standards, improving mine emergency response, and requiring enhanced technology underground for post-disaster communications [11, 12]. This new legislation also developed a completive grant system to quickly develop, evaluate, and adapt new safety technologies used in other industries to the mining industry [13]. Although this legislation was enacted almost a decade ago, the full impact on mine worker safety and health has yet to be determined [14]. The goal of "zero harm" will only be realized if government, industry, and academia work together to improve mine worker safety and health.

1.2: Coal Mining

Coal is a basic component of an industrialized society, and has been a valuable asset to the United States since its inception. Coal was first discovered and mined in the United

States near what is today Richmond, Virginia, and was a strategic resource during the revolutionary war [15]. It also provided a needed energy source to fuel the industrial revolution. Because of its abundance, coal will continue to be a component of the national energy strategy for the foreseeable future.

Despite falling production due to declining natural gas prices, coal continues to be a key component of the national energy strategy. Even though coal production fell by 16% between 2008 and 2013, it is nevertheless projected to provide 34% of the fuel for electricity generation in the U.S. by 2040 [16]. Although coal can be extracted through both surface and underground mining operations, over the last 5 years, roughly 30% of U.S. coal production has come from underground mines [17]. While more coal is produced by surface mines, more workers are employed in the U.S. by underground mining operations.

Most coal is formed from sedimentary organic plant life that has been exposed to heat and pressure over time. There are four main types of coal: anthracite, bituminous, subbituminous, and lignite. This classification is based on the carbon content of the coal, which is related to the amount of heat energy that can be produced through combustion. Initially, anthracite was preferred over other types of coal, but today more than 92% of coal produced in the United States is bituminous or subbituminous [17]. Figure 1.1 shows coal reserves and types by geographic location within the United States [18]. While most of the bituminous and anthracite coal is located in the eastern United States, the west has more subbituminous and lignite coal. Due to greater size and higher value of coal deposits, the eastern half of the U.S. has more active surface and underground coal mining operations [19]. The type, geographic location, and seam depth can determine the mining method used to extract the coal.

Historically, coal mining in the United States was done using primitive methods. Visible ore deposits were mined using quarrying or trenching techniques, by which digging was done using hand tools. Underground mines began to replace surface quarries during the 19th century. The first underground coal mines were drift mines that cut into hillsides.

Later, shaft mines were used to trap coal seams deep beneath the surface. Coal was loaded onto carts or boxes and dragged out of the mine [20]. Eventually, tunnels were bored into the coal seam to make a grid-like system of "pillars" to support the mine roof and provide ventilation. Again, simple tools and primitive machinery were employed until the 1830s when blasting methods became popular [21]. With the introduction of compressed air power at the end of the 19th century, engineers began to examine new ways of mining coal underground.

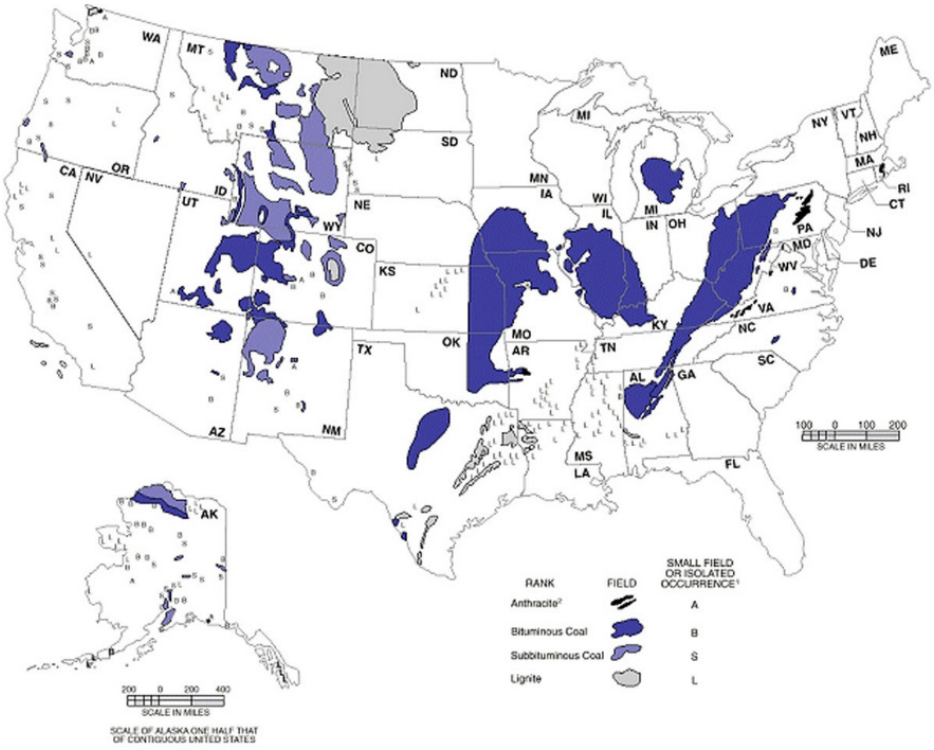

Figure 1.1: Anthracite, Bituminous, Subbituminous, and Lignite coal deposits in the United States [18]

New machinery and better methods were used to mine coal with the start of the industrial revolution. The percussive coal cutter, a drastic improvement over the pick and ax, was light enough to be carried and operated by two men. At the turn of the 19th century, cutting-chain machines were developed to undercut the ore seam for quicker and cleaner extraction [22]. However, industry was slow to implement new technology due to the power and infrastructure requirements of new machinery. It was not until the introduction of the

continuous mining machine (CMM) in 1948 that new mining methods were applied to increase production and reduce operating costs [23]. With the introduction of machinery, mine worker safety was improved, since explosives were no longer required, and the number of workers necessary to operate the mine was reduced. Mechanizing the mining process also allowed underground coal mines to expand in size and depth.

1.2.1. Surface Mining

Due to modern machinery and advanced methodologies, surface mining operations produce a majority of the coal mined in the United States [16]. When a coal seam is relatively close to the surface, overburden soil and rock is removed to expose the coal seam. However, there are various geographical and geological considerations that must be taken into account for a surface coal mine [24-26]. Most surface coal operations can be categorized as open pit or open cast mining. The specific methodologies, processes, and machinery used in surface mines are a function of the coal seam inclination and the surrounding topography.

Removal of overburden and coal extraction at surface mines is done using many different types of equipment. Drilling and blasting methods can be used to initially loosen and cast overburden. Digging and loading functions are completed using shovels and front-end wheel loaders of various capacities. In flat conditions, a surface miner can be used to combine cutting, crushing, and loading functions. For large scale operations, draglines can process massive amounts of overburden. Highwall miners can be used for the extraction of thin coal seams in certain geographical conditions or when overburden removal is cost prohibitive. Finally, haul trucks are the primary equipment used to transport material at surface operations. Auxiliary equipment, such as bulldozers and scrapers, can also be found performing various support functions at a surface coal mine.

1.2.2. Underground Mining

Underground mining operations produce a significant portion of the U.S. coal supply and employ more workers than do surface mining operations. Two basic methods are used to extract coal in underground coal mines: room-and-pillar and longwall [24]. As with surface mining approaches, geological and geographic factors can influence which underground coal mining method is used. Ancillary operations such as roof control, ventilation, and maintenance must also be performed regardless of the mining underground process chosen.

In room-and-pillar mining, intersecting entries are cut into the coal seam. The remaining columns of coal are left in place to help support the mine roof. The general layout and machine interaction of an underground room-and-pillar coal mine is shown in Figure 1.2. After an entry is mined, the mine roof between the coal pillars is further supported by drilling rods into the ceiling, attaching the roof to multiple strata above the coal seam. Mining, haulage, and support functions are carried out using specific kinds of equipment that work in a repeated sequential cycle. Machine interaction between these functions must be optimized to reduce inefficacies and improve mine profit. Underground coal mine entries and cross-cuts in the United States are typically 20–30 ft. wide, and pillars are roughly 100 ft. long. The mine height can be between 42 in. and 12 ft. high, depending on the thickness of the coal seam being mined [24, 27]. The mined coal is moved from the working section by haulage equipment to the section conveyor belt, where it is taken out of the mine for further processing.

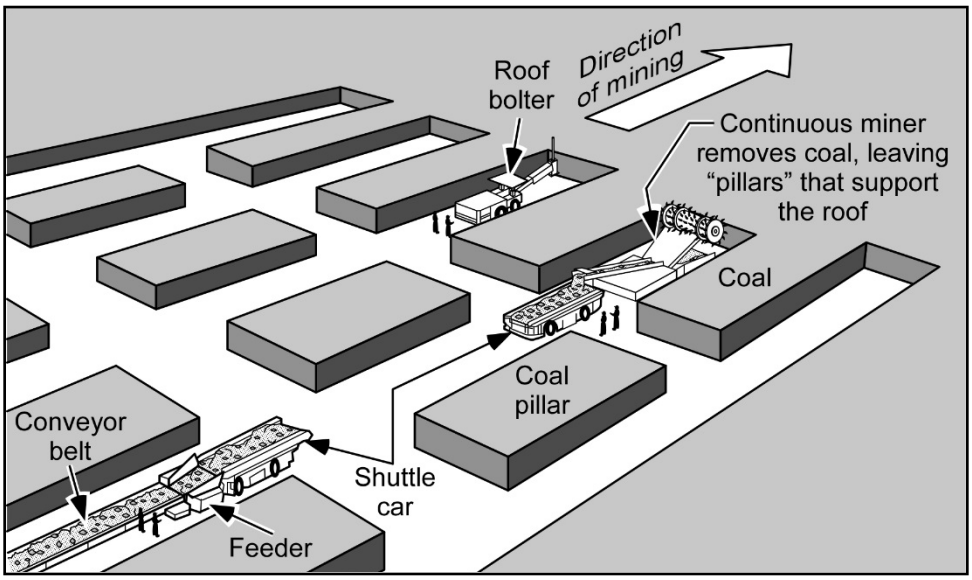

Figure 1.2: Diagram of a Five Entry Room-and-Pillar Underground Coal Mine

The longwall mining method does not require a permanent roof support structure, and, therefore, has a better resource recovery rate than room-and-pillar mining. However, longwall mining can cause surface property damage due to subsidence. Figure 1.3 shows the general layout and components of the longwall mining process used in underground coal mines. Entries are driven similar to room-and-pillar mining to develop the longwall panel, which can be 8,000 to 21,500 ft. long in the United States [24]. The coal seam is cut using an articulating rotary cutting drum called a shearer. As the coal fractures, it falls onto an onboard conveyor system that moves with the shearer. The onboard conveyor system is connected to the mine's continuous haulage system, eliminating the need for individually operated mobile equipment during the mining process. The mine roof is temporarily braced by a system of hydraulic roof supports that advances as the shearer traverses back and forth across the coal seam. As the system advances in the direction of the coal seam, the unsupported overburden collapses behind the hydraulic roof supports.

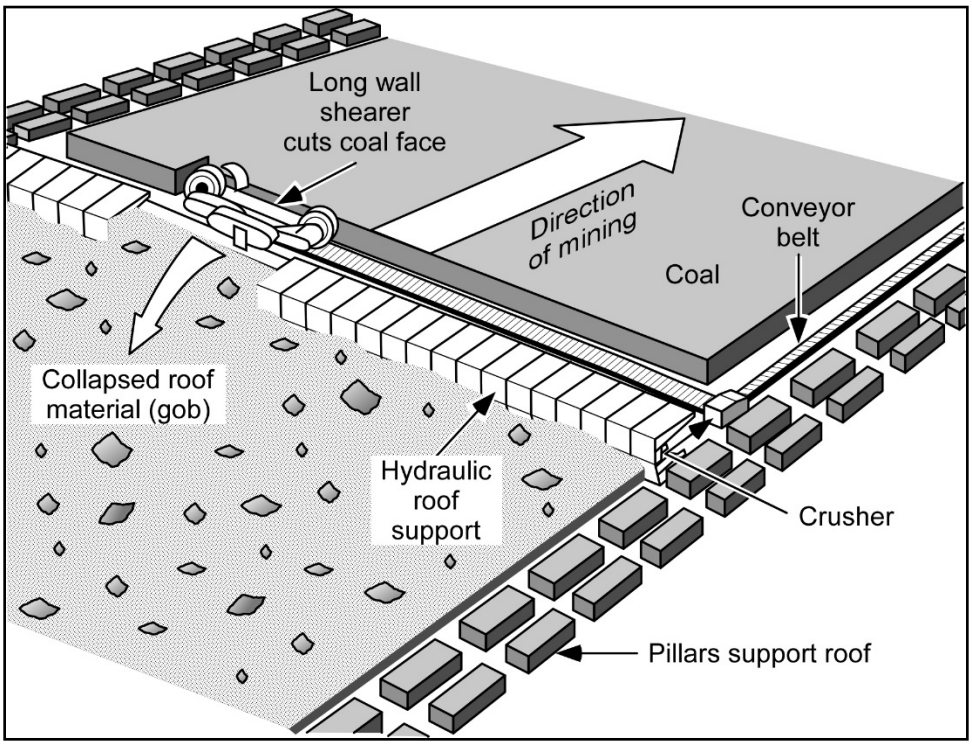

Figure 1.3: Diagram of Layout and Components of an Underground Longwall Coal Mine

Modern underground coal mining methods rely on the use of large and powerful machinery. These methods have led to increased production, reduced operating cost, and overall improved safety for underground mine workers. Unfortunately, machinery is often operated in confined spaces with limited visibility, which can contribute to underground accidents, injuries, and fatalities.

There is a variety of machinery used to extract coal in an underground mine. As described in the previous section, the type of mining method deployed will largely influence which equipment is used. There are also geographical and geological considerations that must be taken into account. However, several types of mobile equipment are fundamental to the underground coal mining process regardless of these considerations.

To move extracted material from the working section, there are many types of equipment used for mine haulage. Different machines, such as cable-reel shuttle cars, articulating

coal haulers, battery-powered scoops, and continuous haulage units, can be put into operation depending on function and mine logistics. These mobile machines are capable of transferring material from the working section to the mine haulage systems, and are powered by electric or diesel motors. Shuttle cars, coal haulers, and scoops are typically four-wheel drive, rubber tire vehicles that have a maximum speed of 6 mph [24]. It is common practice to have multiple mobile haulage units in operation at the same time to increase mine production. Continuous haulage units, while still mobile, are more permanent machines used in low-seam applications that advance with the CMM and connect directly to the main mine conveyor system.

Roof bolting machines are used to develop permanent support for the mine ceiling and walls, called ribs, after an entry has been cut. These machines use high-power electric motors to propel subsystems and components. Most roof bolting machines are rubber tire vehicles but operate at much slower speeds, since they are not used for mine haulage. A hydraulic roof support system is used for temporary support as the rotary drilling mast is operated. After a hole is drilled, a roof bolt is inserted to reinforce the mine roof. The exact type of roof bolt mechanism (i.e., mechanical, resin-assisted, grouted, tensioned rebar, etc.) used for support depends on the mine geology and stress conditions. The entire drilling platform articulates to allow for the drilling of multiple holes without moving the entire machine.

The CMM is an essential piece of equipment used in the development of mine entries to set up both longwall and room-and-pillar operations. A typical CMM used in underground coal mining operations is shown in Figure 1.4. CMMs are used to simultaneously cut, gather, and remove aggregate from the working section(s) of an underground mine. These machines have a series of rotating cutting drums that are fitted with carbide bits that gouge the mine seam (known as the face). Fractured pieces of coal are scooped up by the gathering arms that are located underneath the cutting head. An onboard articulating conveyor system moves aggregate from the front of the machine to the rear, where material is handled by mine haulage equipment.

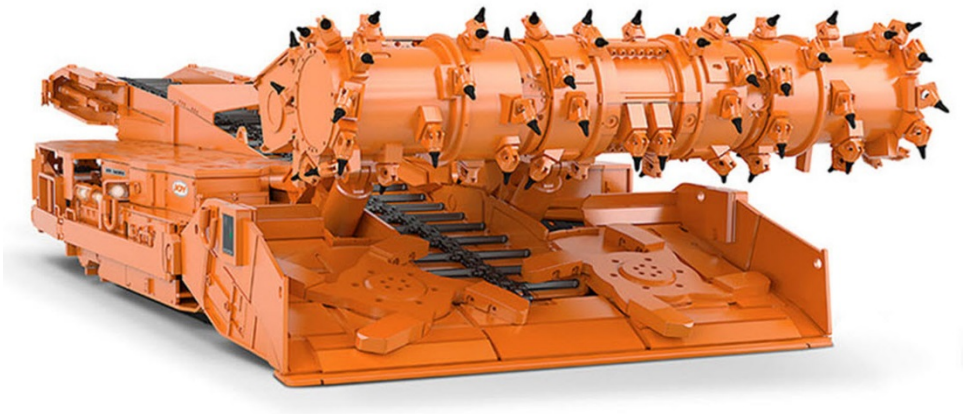

Figure 1.4: Continuous Mining Machine (Courtesy of Joy Global)

To meet a wide variety of underground mining conditions, there are many different models of CMMs that are commercially available. All CMMs are continuous track vehicles, and are capable of pivoting at a high rate of speed [28]. Like roof bolting machines, they rely on high- power electric motors to drive various machine subsystems and components. These machines have a typical cutting width of 12 ft. and can operate in seam heights from 28 in. to 16.5 ft. [24]. The operator maneuvers the machine by remote control, and is typically positioned close to the end of the conveyor tail section. The size and power of these machines can make them difficult to manipulate in the confines of an underground coal mine.

1.3: Machine-Related Accidents and Injuries

Accidents, injuries, and fatalities associated with the operation of equipment and machinery are a major concern for the mining industry. Mine workers interact with large and powerful equipment on a daily basis. While technology and methods have improved, there are still many risks that a mine worker can encounter [28-30]. When comparing

health and safety surveillance statistics, most severe machine-related accidents occur during the extraction of and production of coal. However, across all commodities it has been observed that a majority of accidents occur at surface operations [30]. Often these machine-related accidents and injuries can have long-term health effects and can also have a significant economic impact [31].

Surface mine workers are typically responsible for having a constant situational awareness over an expansive geographical area. For example, 9 out of 16 fatal collision-related accidents over a seven-year period happened while the machine was in reverse [30]. Incidental examination of MSHA accident, injury, and illness statistics across all mining commodities show that "powered haulage" and "machinery" account for a majority of fatalities at surface mining operations [32]. Closer inspection reveals that non-powered hand tools are a significant contributor to non-fatal injuries, while off-road ore haulage is a common source of fatalities [33]. Similar findings are observed when comparing surface and underground accident, injury, and illness statistics.

Underground workers must often perform work tasks around machinery in confined environments that are not properly illuminated. They must also be aware of the ever-changing geology that surrounds them. Similar to the trends observed for all mining commodities, examination of MSHA accident, injury, and illness statistics for underground mining operations show that the 'powered haulage" and "machinery" categories also account for most of the fatalities. However, "fall of ground" has the most associated fatalities out of all individual categories [32]. This risk is unique to underground mine workers, as opposed to surface workers, due to the support and control of the underground environment.

Pinning, striking, and crushing accidents involving underground mobile equipment are a particular safety concern for underground coal mine workers. Specifically examining MSHA fatality data for the ten-year time period of 2004 through 2014, shows that an average of 6.5 deaths occurred per year involving interactions between workers and under-

ground machine operation. Table 1.1 shows the MSHA equipment classification and resulting fatalities from powered haulage and machinery in underground coal mines during this period. A majority of these fatalities involved mobile equipment (continuous miner, load-haul-dump, and shuttle car) used during the mining process. Similar findings have been reported in other coal-producing countries [28, 34-36].

Table 1.1: Underground Coal Mining Equipment and Associated Fatalities from MSHA Accident, Injury, and Fatality Data from 2004 to 2014

Mining Equipment Type	No. of Fatalities
Continuous miner, Tunnel borer, Road header	12
Conveyor, Belt feeder, Stage loader, Hopper shaker, Belt structure	12
Load-haul-dump, Scoop tram, Transloader, Unitrac, S&S Battery	13
Locomotive, (motor) - rail-mounted (Battery, Steam, Electric, Air)	6
Longwall subparts, Duke, Dowdy jack, Ramjack, Longwall shield	3
Mancar, Mantrip, Personnel carrier, Porta bus, Jeep, Jitney, ATV	3
Mine car, Timber truck, Nipper truck	3
Rock or roof bolting machine, Pinning machine, Truss bolter	1
Shuttle car, Buggy, Ram car, Young buggy, Teletram car	11
Tractor, Supply car	1

Repeated machine-related accidents have resulted in the promulgation of new laws and regulations. Initial legislation and rulemaking efforts in the U.S. have focused on reducing injuries and fatalities around specific equipment types in underground coal mines [37, 38]. South Africa has recently produced legislation to ensure collisions between trackless mobile machinery and pedestrian workers do not occur [39]. Although mining is a significant economic component of other countries around the world, there are no other mandates or proposed legislation related to the prevention of machine-related accidents and fatalities.

Legislative efforts in the U.S. have concentrated on the CMM and mobile mining equipment used in underground coal mines. Since the introduction of remote control operation in 1984, 40 fatalities have occurred involving a CMM in underground coal mines. An analysis determined that a proximity detection system with the capability to automatically disable machine motion could have been a preventative factor in 32 of the fatalities involving CMMs [40]. To address this problem, MSHA introduced a rule requiring proximity detection systems on all CMMs used in underground coal mines [37]. Initial rule-making efforts are underway to require proximity detection on all mobile equipment used in underground coal mines [38]. This effort is just one part of a concerted effort to reduce machine-related accidents and injuries across the mining industry.

1.4: Collision Avoidance and Proximity Detection

Many technologies are available to reduce machine-related accidents and fatalities within the mining industry. Collision avoidance systems can rely on a wide variety of technologies such as GPS, radar, laser-based distance sensing, and camera object recognition. Proximity detection senses the presence of nearby objects and typically employs technologies based on electromagnetics. Applications of collision avoidance and proximity detection systems can be found throughout the mining industry across multiple commodities. However, the commodity type and mining method determine which technologies are applicable. For example, open pit surface mines can utilize collision avoidance technologies, while underground coal mines must rely on proximity detection technologies.

Innovation by the automotive industry has led to the advancement of collision avoidance technology. The automotive industry has conducted extensive research and development into obstacle detection, trajectory prediction, and collision avoidance [41-44]. Features such as forward collision warning, autobrake, lane departure warning and prevention, adaptive headlights, and blind spot detection are common options on late model highway vehicles. Most of these systems rely on a combination of radar, vision-based detection,

and internal trajectory tracking [45, 46]. While no country in the world has legislated collision avoidance for automobiles, the U.S. Department of Transportation is conducting the largest trail of vehicle-to-vehicle (V2V) communication systems for collision avoidance [47, 48]. Information sharing between vehicles is expected to greatly improve safety, mobility, and the environment. Combining collision avoidance technologies with V2V communication systems provides the possibility of fully autonomous automobiles without drivers.

The mining industry has also begun to adopt autonomous systems in an effort to increase productivity and improve safety. Teleoperation and driverless haul trucks are beginning to emerge at surface mining operations [49-52]. There have also been various efforts to implement autonomous systems in an underground mining environment [8, 53, 54]. While related, it should be noted that design criteria for eliminating machine-related fatalities and accidents are different from the development of autonomous systems. Although they may reduce some injuries and fatalities, many considerations must be taken into account due to worker interactions with automated technologies [55].

Some of the collision avoidance technologies developed for the automotive industry have transferred to the surface mining operations. However, some important considerations include large mining vehicles used at surface mining operations have considerable blind spots. In addition, vehicle operators must be ever aware of environmental conditions, in-vehicle management systems, navigation systems, and radio communications. Trajectory prediction is also more difficult for mining applications due to unconventional vehicle dynamics, loading, and inconsistent terrain. Despite these constraints, there has been successful application of collision avoidance technologies at surface mines [56-58]. These technologies have also been successfully applied to off-highway and construction vehicles [59-61]. There are further constraints that must be taken into account when implementing collision avoidance in an underground mining environment.

Due to the environment and location, GPS-based collision avoidance systems are not available for underground mining applications. Further complicating matters, mobile mining equipment used in underground stone and metal/non-metal applications often travel between the surface and underground. These systems must be able to operate seamlessly between the surface, when GPS is available with other surface-only equipment, and the underground environment, when there is no GPS available. However, some methods have been developed to determine coordinate location in an underground and/or indoor environment [62-64]. Most systems used in underground mining environments combine proximity detection and collision avoidance technologies due to the confined spaces and interaction with pedestrian workers.

There are more stringent requirements that limit technologies available for machine safety systems used in underground coal mines compared to the other commodities. The presence of methane and the possibility of ignition during the mining process restrict the use of electronic components in underground coal mines. These restrictions vary based upon geological conditions and the regulations imposed by the country in which the mine is located [65].

Several technologies have been investigated despite the limitations on sensors and electrical components for proximity detection systems used in underground coal mines. Many industries use Radio Frequency Identification (RFID) for tracking the movement of objects or people. The mining industry has implemented RFID technologies for the tracking and movements of people, equipment, and supplies throughout mines [62, 66]. These systems are capable of providing information on whether a receiver worn by a person or mounted on a machine is within range of the transmitter, but they are ineffective at providing an accurate distance from the transmitter to the receiver. Another emerging technology is intelligent video utilizing either mono- or stereo-vision to identify and visually locate people and objects [58, 67, 68]. Application of this in underground mines, however, is likely to be very challenging due to poor lighting, dust, and the extreme diffi-

culty in keeping the camera lenses clean. Electromagnetic-based proximity detection systems have demonstrated promise to overcome some of the limitations imposed the underground coal mining environment. Due to their operating frequency, these systems are not affected by the confined space of an underground mine [69]. There are currently four commercially available electromagnetic-based systems approved to meet the permissibility standards for use in U.S. underground coal mines [70]. The widespread adoption of proximity detection technology is expected to significantly improve mine worker safety and health.

Chapter 2: Electromagnetic Proximity Detection

This chapter examines the generation and detection of magnetic fields that are used for proximity detection systems. A description of electromagnetic proximity detection system parameters and components are examined. Theoretical development of magnetic fields produced by ferrite core generators will be used to establish the relationship between magnetic flux density and distance. Methods are then examined to model and approximate the magnetic fields used by proximity detection systems. Finally, triangulation and localization methods are investigated using shell-based magnetic field modeling.

2.1: Proximity Detection for Underground Coal Mining

Due to the mining process and environment, electromagnetic-based proximity detection systems have been developed to reduce machine-related accidents in underground coal mines. The first proximity detection systems installed in underground coal mines were developed for CMMs. However, first generation electromagnetic-based systems were also tested on other types of mining equipment [71]. Using electromagnetic fields, these systems warn underground workers and disable the machine motion when they enter known hazardous areas around the machine.

There are several basic components that interact within an electromagnetic-based proximity detection system. Examples of proximity detection system components for a CMM are shown in Figure 2.1. A machine-mounted field ferrite-core generator produces a magnetic field that covers a geographic area of interest around the machine. Due to the size and geometry of mining equipment, more than one generator is often deployed to fully cover the machine. A worker-worn sensor detects the field strength, which correlates to a general distance from the generator. All workers who interact with and/or are within close vicinity to the machine must wear the sensor for the system to function properly. Magnetic field strength information is sent to the proximity system controller through a

900 MHz transmitter and receiver. Depending on the field strength reading, either a warning alarm or machine shutdown is issued.

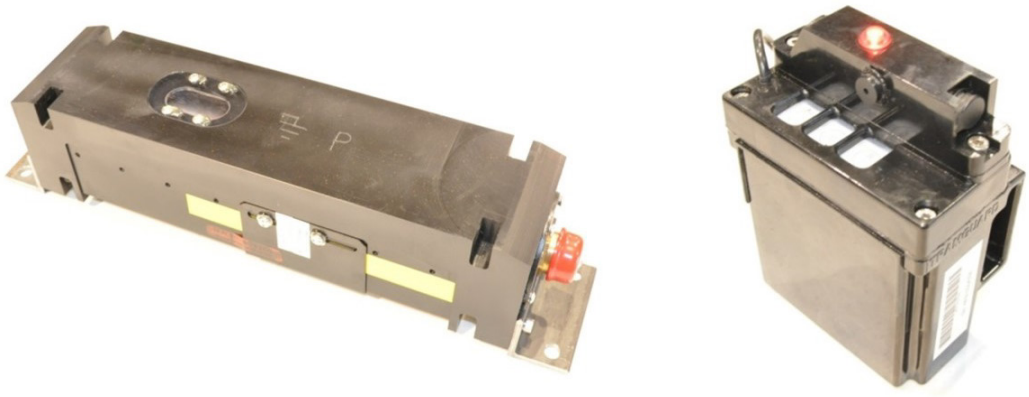

(a) (b)

Figure 2.1: CMM Electromagnetic Proximity Magnetic (a) Field Generator and (b) Sensor

Proximity detection components are used to construct safety zones around a given machine. An example of a warning and shutdown zones around a CMM is shown in Figure 2.2. The magnetic field generators (represented by blue rectangles) are mounted on the machine and transmit a magnetic field that is received by the worker-worn magnetic field sensor. Each generator is adjusted so that a specific magnetic field strength correlates to hazardous areas around the machine. The generators are pulsed at a rapid rate so they do not interfere with the field produced by each given generator. A coordinate system can be defined around the machine using the field strengths to describe different zones of safety around the machine. An alarm is triggered when the receiver enters the warning zone (yellow area around the CMM), and the machine is disabled when the receiver trespasses into the stop zone (red area around the CMM).

The shape and size of the safety zones are defined by the magnetic field generators and machine characteristics. The shape of the zones are spherical in nature due to the magnetic fields produced by the ferrite-core generators. The size of safety zones are defined

based on the specific piece of equipment on which the proximity detection system is installed. For example, machine motion and human interaction was examined to determine the minimum safety zone sizes for the CMM [72].

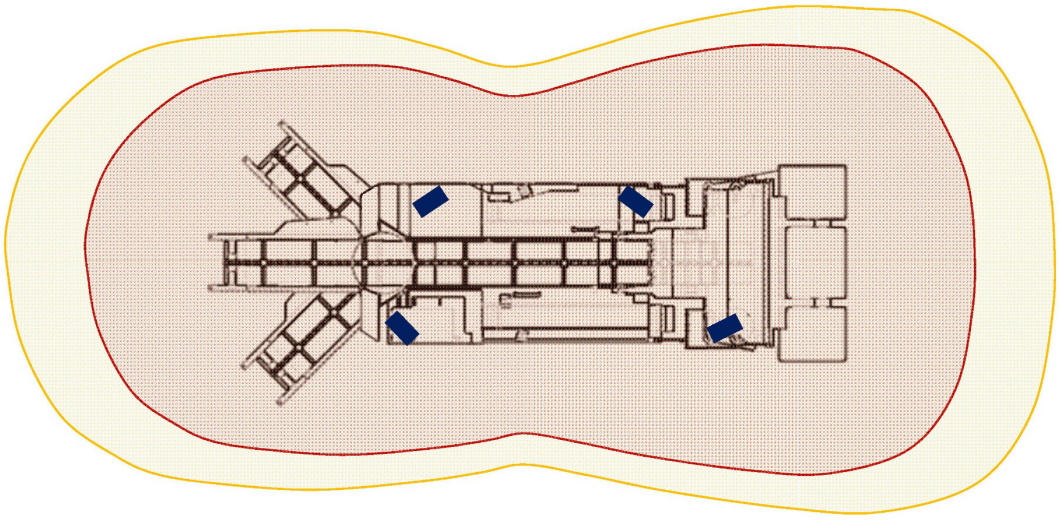

Figure 2.2: Proximity Detection Warning and Shutdown Zones on a Continuous Mining Machine

Further refinements have been made on CMM proximity detection systems to improve performance and worker acceptance. Because of the complex shape of the magnetic fields, accurately determining distance can be difficult. This results in a somewhat ambiguous protection zone around the machine that does not provide for situational or intelligent response to hazards. However, a mathematic model has been developed that can be used to triangulate exact worker location using the magnetic fields produced by multiple generators [73, 74]. Using this approach, zone sizes and boundaries can be based on predefined distances and configured by software.

Intelligent design has been incorporated to limit only machine functions that would induce harm to surrounding workers rather than disabling all machine functions. This technology accurately calculates worker position relative to the CMM and issues situation-specific alarms to warn or disable machine functions to protect the workers from machine

movements that could result in injury [75, 76]. An example of intelligent proximity detection is shown Figure 2.3. Each numbered box represents a safety zone that is linked to specific machine motion capability depending on where workers are located. For example, if a worker is located in zone 2, functions such as reverse and pivot right would be disabled, while functions such as forward and pivot left would be enabled. These intelligent systems have demonstrated superior performance and increased user acceptance [77, 78] .

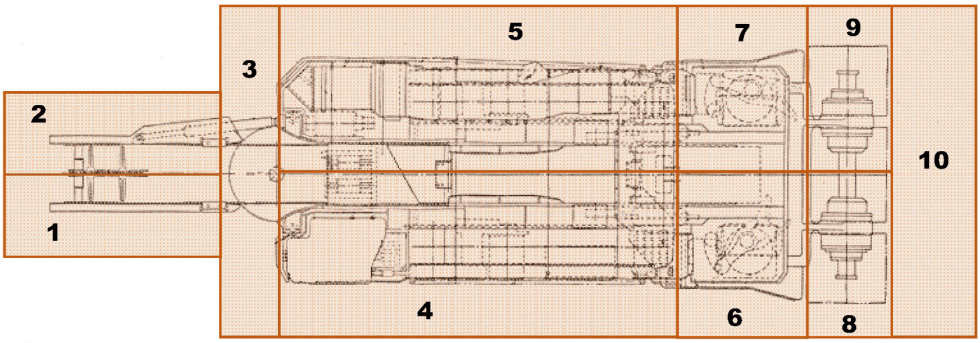

Figure 2.3: Example of Intelligent Proximity Detection Safety Zones for a CMM

The performance of proximity detection systems used in underground coal mines can vary site to site. Several studies have investigated the performance of proximity detection systems used in underground coal mines. The studies examined different scenarios to try to quantify proximity detection system performance in an underground environment [69, 79]. Several factors influence the accuracy and repeatability of proximity detection systems. Extreme temperature change can affect electromagnetic components and circuits. Parasitic coupling of the magnetic field with power cables. Other metal objects in the mine can also alter magnetic field distribution patterns. While proximity detection systems generally performed as designed during these evaluations, a wide range was observed.

2.2: Electromagnetic Field Generation and Detection

Proximity detection systems for underground coal mining equipment use electromagnetic fields to estimate worker distance to a machine. The system uses this information to issue warnings and/or disable machine functions. To establish magnetic fields around entire machines such as the CMM, multiple ferrite core generators are used. The magnetic field is detected by a sensor that is worn by workers and measures the magnetic field flux density. The value of magnetic field flux density from each sensor is used to derive a relative distance between the worker and the machine.

2.2.1. Magnetic Field Generation

The generation of magnetic fields for proximity detection systems can be understood by examining the low frequency application of loop antennas. The field radiation pattern of a small loop is derived by considering a square loop consisting of four linear dipoles. The same field equations can also be obtained by realizing a small square loop is equivalent to a short linear dipole [80, 81]. The analytic equations describing the fields of a short magnetic dipole will be the basis for the modeling efforts of electromagnetic proximity detection systems used in underground coal mines.

An elementary antenna or radiator, such as a short linear dipole, can be examined to understand basic magnetic and electric field radiation patterns. The magnetic field radiation pattern for a short linear dipole is similar to the electrical field radiation patterns. Although actual linear dipoles would be very thin and have plates at either ends for capacitive loading, the electromagnetic fields produced by the system shown in Figure 2.4 are examined here. The medium surrounding the dipole is air, and the center of the dipole is located at the origin. The length of the dipole Δz is small compared to the wavelength λ, which ensures uniform current I along the entire length of the antenna.

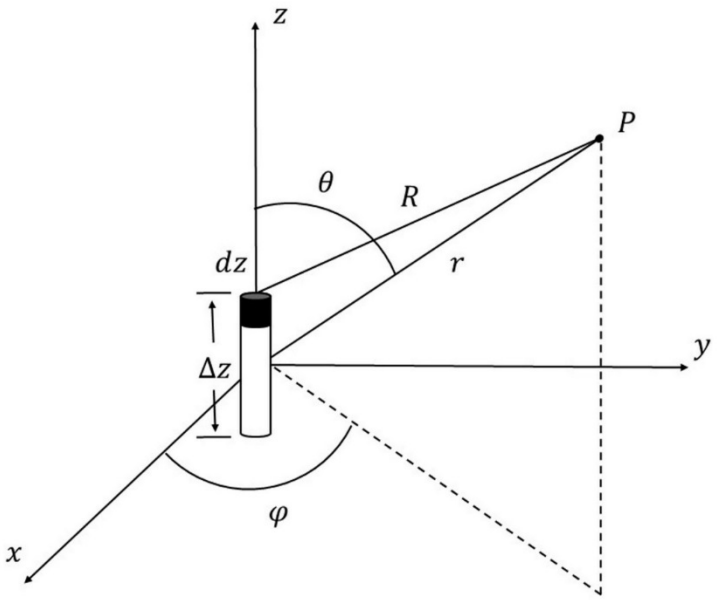

Figure 2.4: The ideal dipole antenna with a uniform current

The magnetic field intensity $\boldsymbol{H}$ can be obtained through the relationship with the magnetic vector potential $\boldsymbol{F}$.

$$\boldsymbol{H} = \frac{1}{\mu}\boldsymbol{\nabla} \times \boldsymbol{F} \tag{2.1}$$

The electromagnetic wave propagation is observed at a point P in space from an antenna as illustrated in Figure 2.4. The vector potential for a short dipole antenna with a constant electric current amplitude I can be expressed as:

$$\boldsymbol{F} = \hat{\boldsymbol{z}}\mu I \int_{-\Delta z/2}^{\Delta z/2} \frac{e^{-j\beta R}}{4\pi R} dz \tag{2.2}$$

where the electromagnetic wave propagation phase constant β is represented by:

$$\beta = \frac{2\pi}{\lambda} \tag{2.3}$$

The distance R from the current element to a field point P in Figure 2.4 is roughly equal to the distance r, between the origin and the same field point. Setting these distances equal and integrating Equation (2.2) yields the relationship:

$$\boldsymbol{F} = \frac{\mu I e^{-j\beta r}}{4\pi r} \Delta z \hat{\boldsymbol{z}} \tag{2.4}$$

Substituting Equation (2.4) into Equation (2.1) yields:

$$\boldsymbol{H} = \frac{1}{\mu} \nabla \times \boldsymbol{F} = \frac{I\Delta z}{4\pi} \left[\frac{j\beta}{r} + \frac{1}{r^2}\right] e^{-j\beta r} sin\theta \hat{\boldsymbol{\varphi}} \tag{2.5}$$

The magnetic field vector $\boldsymbol{H}$ is perpendicular to z axis in Equation (2.5). This demonstrates that even simple antennas, such as an ideal dipole, have a complicated field radiation pattern at a distance close (near-field) to the antenna. For a given current, the magnitude of the magnetic field $|\boldsymbol{H}|$ can be obtained from Equation (2.5) to give:

$$|\boldsymbol{H}| = \left|\frac{I\Delta z}{4\pi} \left[\frac{j\beta}{r} + \frac{1}{r^2}\right] e^{-j\beta r} sin\theta \hat{\boldsymbol{\varphi}}\right| = \frac{I\Delta z}{4\pi} \left|\left[\frac{j\beta}{r} + \frac{1}{r^2}\right] e^{-j\beta r}\right| sin\theta \tag{2.6}$$

Dividing constant current on both sides of Equation (2.6) produces the relationship:

$$\frac{|\boldsymbol{H}|}{I} = \frac{\Delta z}{4\pi} \left|\left[\frac{j\beta}{r} + \frac{1}{r^2}\right] e^{-j\beta r}\right| sin\theta \tag{2.7}$$

By inspection, the right hand side of Equation (2.7) is a constant at a point P in space for a given frequency and antenna dimensions. Equation (2.7) also implies that there are a number of points around the antenna that will have the same value, which can form a closed shell. For a given point at a distance from the antenna, there exists only one shell for that point. Moreover, each shell is unique in size, shape, and position with respect to

the antenna. These shell values can be used to approximate distance between the antenna and magnetic field.

A small dipole antenna has a fixed radiation pattern for given antenna dimensions and frequency. However, other types of antennas have their own radiation patterns that are dependent on loop dimensions and operating frequency. A circular loop of electric current produces a magnetic field that is nearly identical to the field of two oppositely charged magnetic monopoles. The magnetic radiation pattern of a small loop antenna is shown in Figure 2.5. The space pattern consists of doughnut-shaped figures of revolution about the axis of the antenna and is proportional to the sine of θ. Basic understanding of the electromagnetic fields produced by generators can be used by proximity detection systems.

The above analysis examines the magnetic field $\boldsymbol{H}$ that is produced by an antenna. Proximity detection systems measure the magnetic flux density $\boldsymbol{B}$, which can be found through the relationship:

$$\boldsymbol{B} = \mu \boldsymbol{H} \tag{2.8}$$

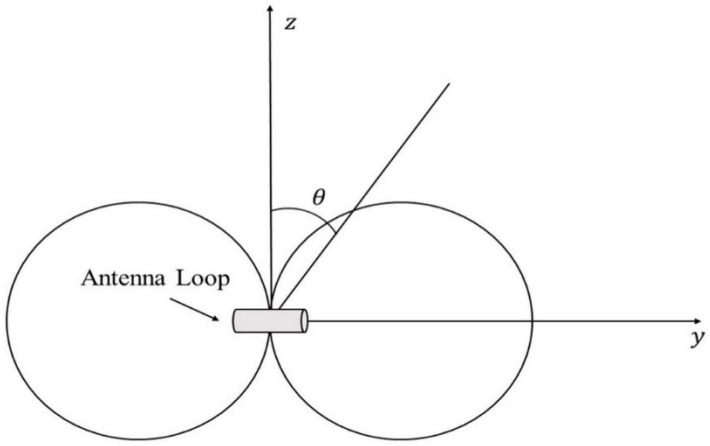

Figure 2.5: Radiation Pattern for a Small Loop Antenna

Constant values of magnetic flux density $\boldsymbol{B}$ at various points in the magnetic field can also be represented as a shell. The relationship between constant magnetic flux density $\boldsymbol{B}$ and distance from the magnetic field generating antenna can be exploited by proximity detection systems. Modeling the magnetic field as shells of constant flux density can define a safe zone perimeter or exact worker location around a machine.

2.2.2. Electromagnetic Field Detection

When using proximity detection systems in underground coals mines, workers wear a sensor that detects the signal produced by magnetic field generators. These sensors measure the magnetic flux density $\boldsymbol{B}$ using small loop antennas on each of the three orthogonal axes. Voltage induced by the magnetic field in each of these antennas is measured and converted to the magnetic flux density $\boldsymbol{B}$ along each axis. The vector sum of these measurements is used to calculate total magnitude of the magnetic field. The value of the magnetic flux density $\boldsymbol{B}$ can be used to estimate the distance between the generator(s) and sensor.

To determine the magnetic field density at a point in space, an induced voltage ε is produced when a change in magnetic flux passes through a conductive loop [82]. This can be expressed using Faraday's law as:

$$\varepsilon = \oint \boldsymbol{E} \cdot dl = -\frac{d\phi}{dt} = \int \frac{\partial \boldsymbol{B}}{\partial t} \cdot d\boldsymbol{A} \tag{2.9}$$

Where the loop antenna has a total area $\boldsymbol{A}$ and the total magnetic flux ϕ that passes through it. With a uniform magnetic field within a loop antenna that has a radius r and number of turns N, the induced voltage can be determined by:

$$\varepsilon = N \oint \boldsymbol{E} \cdot dl = -N\frac{d\phi}{dt} = -N\pi r^2 \frac{d\boldsymbol{B}(t)}{dt} \cdot \hat{A} \tag{2.10}$$

Due to a uniform current input, the time dependent magnetic field can be expressed as a continuous sinusoid with:

$$B(t) = B_{\boldsymbol{m}} \sin \omega t \tag{2.11}$$

Substitution of Equation (2.11) into Equation (2.10), and taking the derivative of $\boldsymbol{B}(t)$ gives the relationship:

$$\varepsilon = -N\pi r^2 \omega B_m \cos(\omega t) \cos(\alpha) \tag{2.12}$$

Where the angle α is between the surface plane of the loop antenna and the magnetic flux density passing through the plane. Considering the Root Mean Square (RMS) value of Equation (2.12), the measured magnetic flux density can be represented by:

$$B = \frac{-\varepsilon}{N\pi r^2 \omega \cos(\alpha)} \tag{2.13}$$

For a single loop antenna, the measured magnetic flux density can be determined using Equation (2.13). Three orthogonal coils each aligning to their coordinate system can measure separate and distinct magnetic field values since the angle α is unique in each direction. The magnitude of the magnetic flux density at a point in space can be expressed using the relationship:

$$B = \sqrt{B_x^2 + B_y^2 + B_z^2} \tag{2.14}$$

Several considerations should be examined when developing systems to measure magnetic fields. To accurately measure the magnetic flux density at a point in space, the magnetic probe should be small. This reduces the error produced by a variation of magnetic flux density within the enclosed area of each coil in a probe. However, small coils complicate system design of the probe.

As discussed in the previous section, magnetic field radiation patterns can be expressed as a shell. Many points having a different distance from an antenna can have the same measured value of magnetic flux density, and therefore reside on the same shell. Magnetic flux density at a point in space can only be used to determine the shell on which the point resides, giving an approximation of distance from magnetic field source. These magnetic flux density shells are not easily described by standard geometric shapes. An analytical model has been developed that describes the magnetic shell patterns [73]. This model can be used to improve proximity detection performance by more accurately determining the worker position around a machine.

2.3: Electromagnetic Field Modeling

Magnetic field generators can be positioned so that the magnetic shell surfaces represent a geographical boundary. Using time-sequenced pulse generators and logical threshold values of magnetic flux density, the complex point shell zones can be defined. If a magnetic flux density is measured by the wearable component of a proximity detection system that traverses a zone boundary, then an alarm is issued or the machine is shut down. However, discrepancies can occur between magnetic shell surfaces and desired zone boundaries. The zone boundaries are predefined and physically decoupled from the measured magnetic shell surfaces. Differences between the shell surfaces and zone boundaries produce false alarms and limit proximity detection performance.

2.3.1. Magnetic Shell Model

Defining the relationship between the magnetic field generator distance and flux density magnitude allows for a more precise estimate of sensor location. Several methods have been developed to model the magnetic field patterns generated by ferrite core coils used

by proximity detection systems [73, 83]. While these models can be used to describe the spherical nature of magnetic flux density point shells, the two-dimensional (2-D) forms are easier to evaluate and hold true due to the axial symmetry of magnetic fields.

The magnetic shells produced by ferrite core generators can be defined in either polar or Cartesian coordinates. The diagram in Figure 2.6 shows a magnetic field generator coil and the associated 2-D coordinate system. Each point P of a shell can be uniquely associated with a constant magnetic flux density B and coordinate.

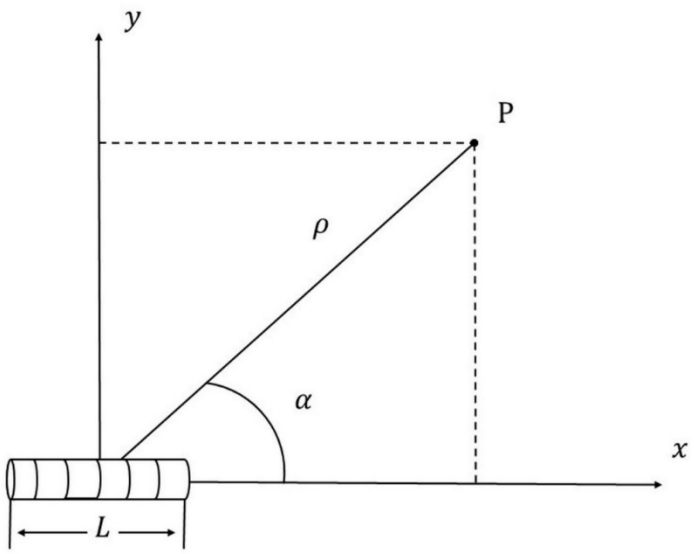

Figure 2.6: Ferrite Core Generator and 2-D Coordinate Systems

Constant magnetic flux density is used to describe the distance from the ferrite core antenna to the measurement point shell. The magnetic fields can be described as shell-based magnetic flux density distribution patterns. Through regression analysis, magnetic field measurements are used to model specific magnetic fields [74, 83]. The generalized expression for describing a shell produced by a magnetic field generator in polar coordinates is:

$$\rho = a(\cos 2\alpha) + b, \qquad for \begin{cases} a + b > L/2 \\ |\alpha| \leq 2\pi \end{cases} \tag{2.15}$$

The radial distance ρ is measured from the center of the ferrite core antenna with a length L at an angle α to a point in space. The shell shape parameter a and size parameter b are determined from the measured magnetic field and defined as:

$$\text{Shell}(\rho, \alpha|B) = \begin{cases} a = c_a B^{-d_a} \\ b = c_b B^{-d_b}, \end{cases} \quad for\ B > 0 \tag{2.16}$$

The measured magnetic flux density $\boldsymbol{B}$ increases with decreasing distance from the magnetic field generators to the magnetic field shell. The positive constants c_a, c_b, d_a, and d_b are dependent of the physical and electrical properties of the ferrite core generator. These constants are determined such that $0 < c_a < c_b$ and $0 < d_a < d_b < 1$, and govern how the shell varies in shape and size with magnetic field.

Further insight about the magnetic shell model can be gained by graphically examining these governing equations. The solid blue line in Figure 2.7 represents the magnetic shell shape that is described by Equations (2.11) and (2.12). The shell radius ρ varies between the parameters $a + b$ and $b - a$, which can be represented circles (dotted lines). The sum of these parameters is represented by the circle with a radius value of ρ at 0° and 180°. The difference of these parameters is represented by the circle with a radius value of ρ at 90°. At an angle of 45° the shell intersects a circle that has a radius equal to the parameter b.

By applying these graphical relationships, insight can be gained on how the shell model will behave. A large value of the parameter a in relation to parameter b will produce a more irregular shape. Conversely, a small value of the parameter a in relation to parameter b will produce a shape resembling a circle. As distance from the generator increases the magnetic flux density decreases, and the parameter b becomes large in comparison with parameter a. This creates a more uniform shell shape approximating a circle with increasing distance from the generator.

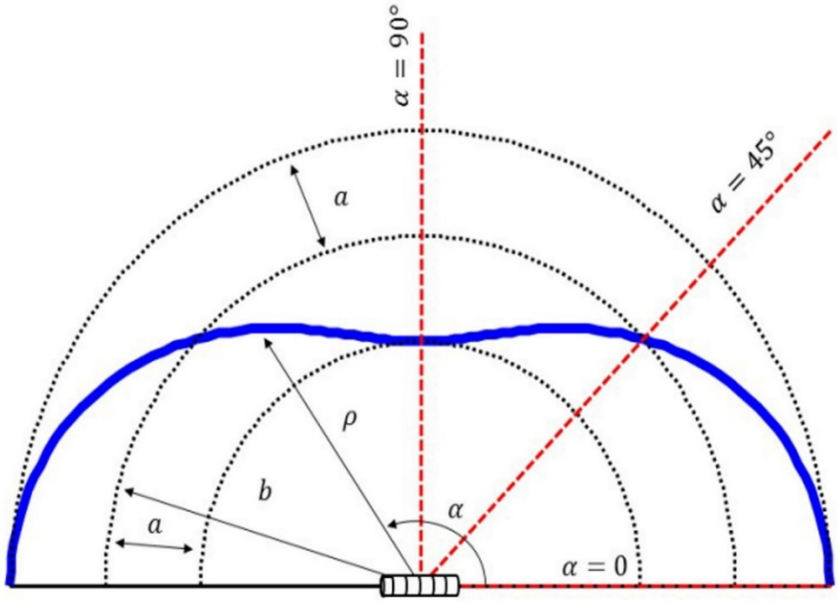

Figure 2.7: Magnetic Flux Density Shell Model

A shell-based model describing the magnetic fields can be used to improve the performance of electromagnetic proximity detection systems. Multiple ferrite core antennas are used to produce the magnetic field around the machine. Each magnetic field generator has a magnetic shell that is dependent on the magnetic flux density. The intersection of these shells can be used to triangulate and track location. Advanced capabilities, such as selective machine shutdown, rely on accurate determination of worker positions around the machine.

2.3.2. Transferable Shell-Based Model

Electromagnetic proximity detection systems rely on consistent magnetic flux density distributions from multiple generators to function properly. During installation, proximity detection systems are calibrated and adjusted before being deployed. Magnetic flux density readings from each generator are used to identify zone boundaries. The overlapping

electromagnetic field distribution around the machine is used to define the different safety zones.

Set-up and calibration of proximity detection systems in this way can affect and limit performance. Manually calibrating based on the magnetic flux density readings is a time consuming process that can lead to zone detection errors. In addition, maneuvering a piece of equipment in an underground coal mine to correctly map the magnetic field distribution can be unsafe. By adjusting the output of the magnetic field generators to modify safety zone boundaries, the burden of calibration is reduced and performance improved.

As explained in the previous section, antennas have specific electromagnetic radiation patterns in the far field. The Biot-Savart law can be used to estimate magnetic flux density at a point that is the result of electric current applied to the coil [84]. The diagram shown in Figure 2.8 shows the relationship between the instantaneous magnetic flux density dB and constant electric current I in a coil wire. An infinitesimal segment of the coil wire is represented by length dl, and the distance to the instantaneous magnetic flux density dB is represented by the vector length r.

Assuming electric charge does not accumulate anywhere in the coil, the cross product between dl and r determines the magnitude and direction of the magnetic flux density B. This relationship can be expressed as:

$$d\boldsymbol{B}(r) = \frac{\mu_0}{4\pi}\frac{I\, d\boldsymbol{l} \times \hat{\boldsymbol{r}}}{|\boldsymbol{r}|^2} \tag{2.17}$$

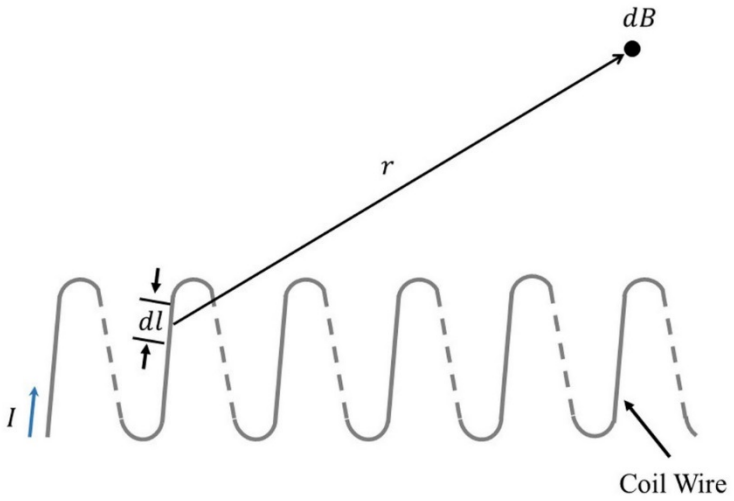

Figure 2.8: Magnetic Flux Density at a Point Near a Wire Coil with Applied Electric Current

The integral form of Equation (2.17) can be expressed as:

$$\boldsymbol{B} = \int_L \frac{\mu_0}{4\pi} \frac{I\, d\boldsymbol{l} \times \hat{\boldsymbol{r}}}{|\boldsymbol{r}|^2} = \frac{\mu_0 I}{4\pi} \int_L \frac{d\boldsymbol{l} \times \hat{\boldsymbol{r}}}{|\boldsymbol{r}|^2} \tag{2.18}$$

Considering the constant electric current I and taking the absolute value, Equation (2.18) can be rewritten as:

$$\frac{B}{I} = \frac{|\boldsymbol{B}|}{I} = \frac{\mu_0}{4\pi} \left| \int_L \frac{d\boldsymbol{l} \times \hat{\boldsymbol{r}}}{|\boldsymbol{r}|^2} \right| \tag{2.19}$$

The ratio between magnetic flux density and electric current in Equation (2.19) can be used to establish a relationship to predict the magnetic field. The magnitude of the magnetic flux density B changes proportionally to the supplied electric current I. The integral in Equation (2.19) will always produce a scalar constant for a given point P within the magnetic field. This suggests that a given ratio between B and I can be used to identify a unique point P on a shell of constant magnetic flux density.

The ratio relationship between magnetic flux density and electric current can be incorporated into the magnetic shell model. A changed electric current will correspond to a changed magnetic shell. This concept can be expressed through a mapping transfer function as:

$$\tau = \frac{I_b}{I_c} \tag{2.20}$$

The base electric current is represented by I_b, and the changed electric current is represented by I_c. The relationship in (2.20) can be incorporated into the shape and size shell-based modeling equation of (2.16) to find the changed magnetic flux density B_c:

$$\text{Shell}(\rho, \alpha|B) = \begin{cases} a = c_a(\tau B_c)^{-d_a} \\ b = c_b(\tau B_c)^{-d_b}, \end{cases} \quad for\ B_c > 0 \tag{2.21}$$

The ratio relationship τ in Equation (2.21) allows for the conversion of a current specified field-invariant model to a general transferable field-variant model. A magnetic field generator has a distribution pattern that is independent of the magnetic flux density and supplied electric current. The relationship between B and I can be used to express the magnetic fields as nested shells, with surfaces representing a constant value.

Using a transferable magnetic shell-based model has many advantages for electromagnetic proximity detection systems. There is no need to obtain an additional shell based model for each generator with a supplied electric current. This can reduce the effort required to set up and calibrate electromagnetic proximity detection systems. Field adjustments can be made by simply adjusting the electric current supplied to the magnetic field generators. A transferable model also lays the foundation for automatic magnetic field control against drift and environmental influences.

2.4: Positions Triangulation

Several technologies and methods can be used to determine the position of a person or object. The most commonly used localization systems for outdoor applications are satellite navigation. For indoor and underground application, navigation and tracking systems are GPS denied. However, extensive research has been conducted during the last decade to develop accurate and reliable measurement of position in indoor environments [85-87]. Much of the research has been specifically targeted to applications involving existing wireless networks or for mobile devices such as smart phones [63, 88, 89]. Most of this technology is not applicable to the mining industry due to unique work conditions and safety requirements.

Tracking systems have been developed and deployed in the mining industry to provide the location of personnel in an underground mine. There are a variety of technologies and techniques currently in use for underground tracking systems [90]. Some of the concepts and techniques used for miner tracking could be incorporated into hazard recognition and intervention systems. However, more research and information are needed for an integrated and multipurpose systems approach. Underground workers near equipment can be tracked using electromagnetic proximity detection systems. By taking advantage of electromagnetic shell-based modeling, worker position around the machine can be determined.

The shell-based magnetic model can be used to describe the electromagnetic fields produced by proximity detection system used in underground coal mines and determine worker location. A specific value of magnetic flux density can be related to a relative distance from a given generator. However, the intersection of two or more magnetic shells at the sensor location is the approximate position of the worker in two-dimensional space. Triangulated position provides system intelligence rather than simplified warning and stop zones.

The intersection of two constant magnetic flux density shells can be examined graphically. A two-generator system is shown in Figure 2.9. The magnetic shells produced by Generators1 and 2 are represented by solid blue and green lines, respectfully. As also demonstrated in Figure 2.7, the dashed red lines ($\alpha = 45°$ and $\alpha = 90°$) represent the magnetic shell model constants, and the dotted circles represent the relationship between them. The intersection of the magnetic shells occur at $\rho_1 = \rho_2$ with the angles α_1 and α_2 in their respective coordinate systems.

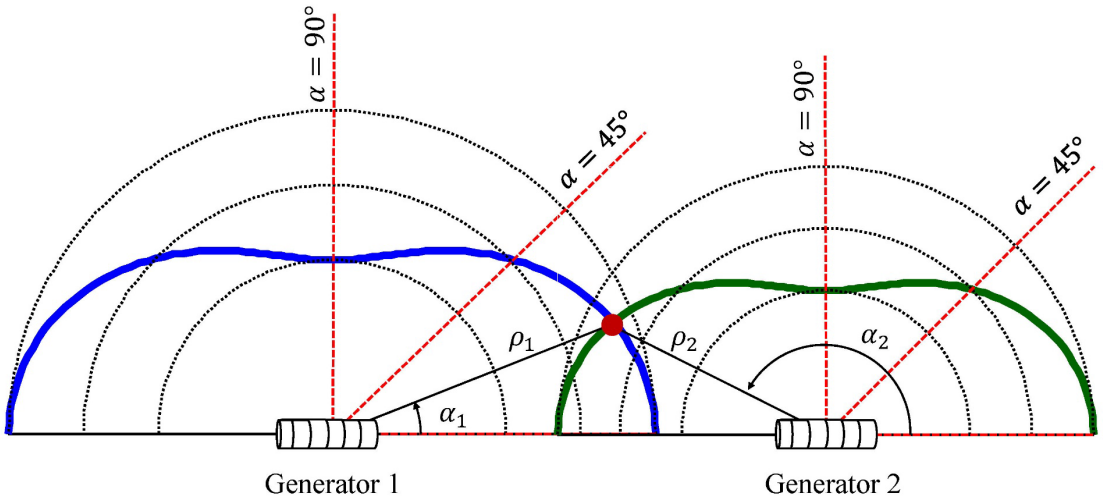

Figure 2.9: Two-Magnetic Field Generator System Triangulation

Analysis of a generator system can be used to develop a simplified version of proximity detection triangulation, but it has some limitations. Due to the spherical three-dimensional nature of the magnetic field model, a third generator is needed to accurately determine worker position. This can complicate the data visualization and the process of determining and converging a solution [91]. The coordinate values of the intersection must also be mapped back to the machine coordinate system. However, the simplified two-generator system has some practical uses. It can be used to accurately study the influence of environmental factors and improve overall proximity system performance. Findings from a two generator system can be extended to systems with more than two magnetic field generators and will help increase system accuracy.

Chapter 3: Experimental Electromagnetic System

In this chapter, an experimental proximity detection system consisting of two magnetic field generators is developed and demonstrated. Although a two-generator system does not have practical application in an underground working environment, it can be used to study and improve electromagnetic proximity detection system performance. With an electromagnetic field generating system established, field measurements are used to develop a shell-based model for each generator. Position triangulation, at the intersection of magnetic flux density magnetic shells, is evaluated against magnetic field measurements. The effects of temperature on magnetic field generators are examined, as is the pulsing of magnetic fields. The experimental system developed in this section will be used as the basis for development of a control system in the next chapter.

3.1: Experimental System Components and Layout

A two-generator system was constructed in a laboratory environment to minimize the effects of environmental factors. Large metal objects can alter the magnetic field distribution produced by the generators. This was taken into account when determining the test location, which was free of large masses of metal. The general layout of the experimental two-generator system is shown in Figure 3.1. A large wood table (4.3 x 1.2 x 1.5 m) was constructed to lay out the coordinate systems and measure the electromagnetic field data. The ferrite-core antennas are positioned on the edge of the table, each 1 m from the centerline. The magnetic fields are measured with a single IDR-325 Gauss meter (s/n: 0420). Surface temperatures of the ferrite-core magnetic field generators are measured using J-type thermocouples bonded to the surface of the antenna. Two A.H. Systems Inc. model BCP-611 Current Transformer (CT) probes (s/n: 1304 and s/n: 1342) are used to measure electric current across each ferrite-core antenna.

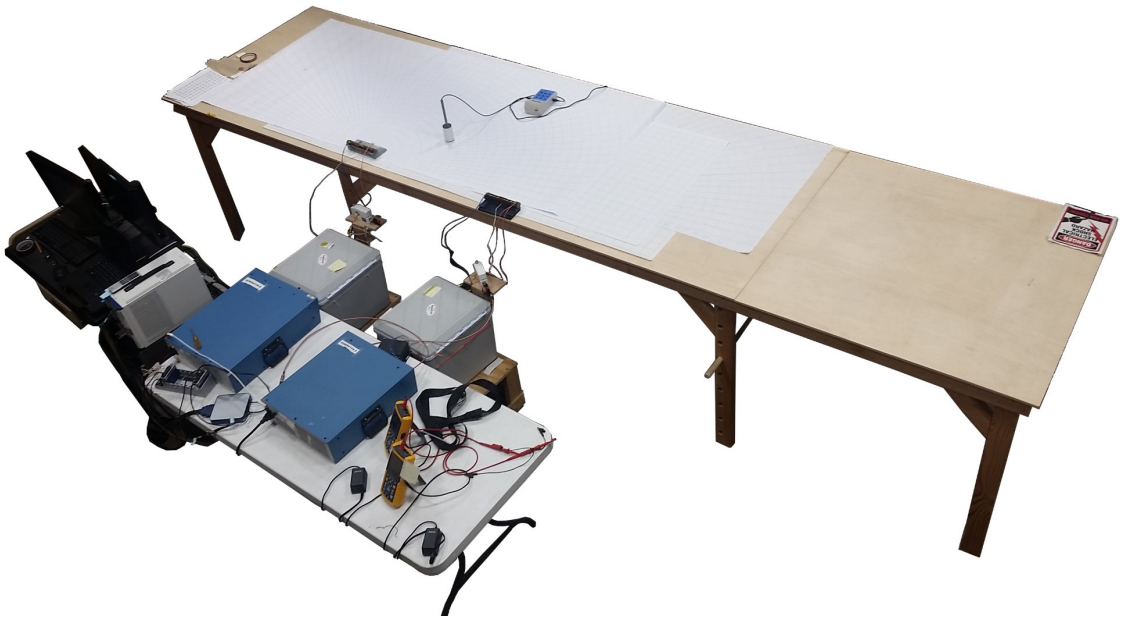

Figure 3.1: Experimental Two-Generator Electromagnetic Proximity Detection System

Several subsystems and subcomponents are required to produce the magnetic fields. The amplifiers and impedance-matching circuits are located directly behind the wooden coordinate measuring table in Figure 3.1. The signal generator and pre/post processing computer is located to the left of the amplifiers. Each generator subsystems uses a separate Electronic & Innovation model 1020L power amplifier (s/n: 1040 and s/n: 2021) capable of producing 200 W of adjustable power. A circuit that matches the impedance of each generator is housed in 12V 36-Quart Kool Thermoelectric Cooler. The coolers protect and insulate the high-voltage components of the circuit and minimizes temperature fluctuations.

To achieve maximum magnetic field generating efficiency at the ferrite-core antenna, an impedance-matching transformer and capacitor bank is used. The impedance-matching circuit components for magnetic field generator 1 is shown in Figure 3.2 (a). These separate sets of components are connected in series to the ferrite-core antennas, which produce the magnetic fields. The ferrite-core antenna for magnetic field generator 2 is shown in Figure 3.2 (b).

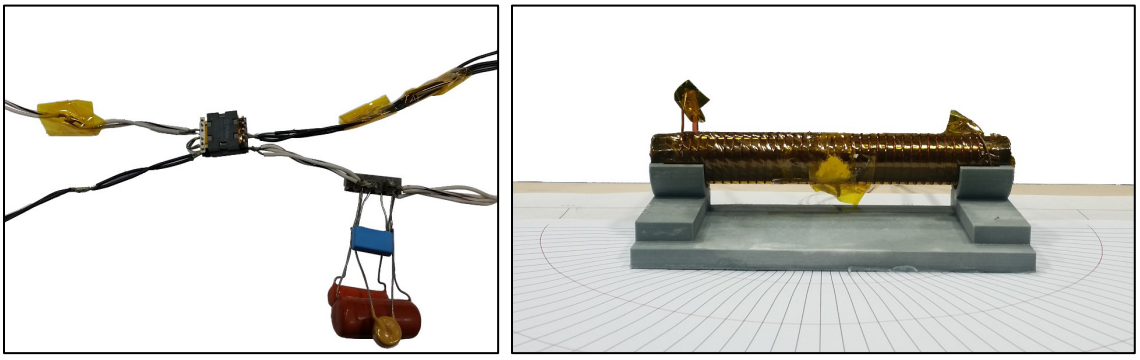

(a) (b)

Figure 3.2: Experimental Magnetic Field Generator components (a) Transformer and Capacitor Bank, and (b) Ferrite-Core Antenna

Data input, output, and processing is monitored and controlled through several specialized computer boards. A Dell OptiPlex 760 computer (s/n: HM40SK1) with a 3 GHz processor and 4 GB of RAM is used for data processing and visualization. A National Instruments PXIe-1082 with a PXIe-8840 controller (s/n: 30E0600) and PXI-7854R analog input/output board (s/n: 19B6BB3) is used to generate the 73 kHz signal to the power amplifiers. A National Instruments cDAQ-9178 (s/n: 17F9993) with NI-9211 (s/n: 157B561) and NI-9223 (s/n: 1AD7DA6) input modules observe temperature and input voltages from the CT and thermocouples. Although the PXIe-1082 system is capable of acquiring this data, the cDAQ-9178 is used to improve computational efficiency and data visualization. A schematic of the both magnetic field generators is shown in Figure 3.3. A National Instruments SCB-68A shielded 68-Pin connector block (s/n: 1B929CC) was used to make all interface connections for the experimental system. Input and output information is processed and displayed through a custom-built National Instruments LabVIEW Program (see Appendix A).

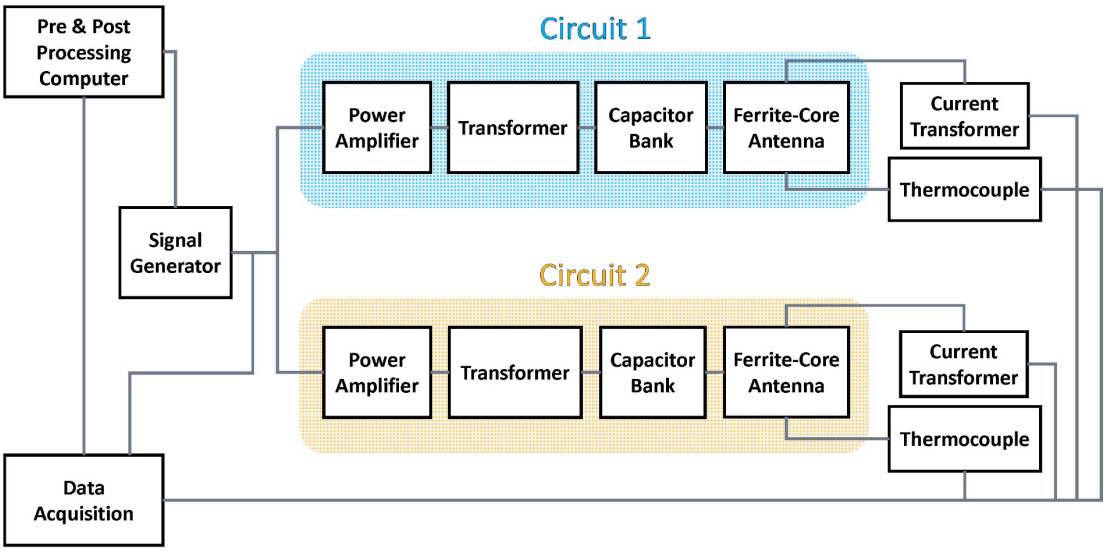

Figure 3.3: Schematic of Experimental Magnetic Field Generator Systems

3.2: Magnetic Field Generator Circuit Design

The physical characteristics of the ferrite- core antennas determine the magnetic field generator circuit parameters. The ferrite- core antennas used in the experimental system have been repurposed from a commercial Strata Worldwide proximity detection system. These systems have an operating frequency of 73 kHz, and is are a design constraint of the experimental system. Each ferrite rod has a length of 19.1 cm, radius of 1.27 cm, and coil of 36 turns. The antennas are generically referred to as Antenna A (s/n: 6603), used for magnetic field Generator 1, and Antenna B (s/n: 6558), used in magnetic field Generator 2, to differentiate them from one another.

The magnetic field generating circuits are designed separately and independently of one another, since each antenna has different electrical properties. The electronic circuit parameters are identified by investigating the electrical properties of each ferrite-core generator. An Agilent E4980A Precision LCR Meter (s/n: MY46207864) is used to examine the electrical resistance, inductance, and impedance for each antenna. The experimental

setup is shown in Figure 3.4 (a). Short 14 gauge copper lead wires are used to connect the LCR meter and antenna. The antenna properties from 20 Hz to 500 kHz were collected and inspected. The inductance between Antenna A (solid red line) and Antenna B (dotted blue line) is shown in Figure 3.4 (b). Values vary across the frequency spectrum of interest. Similar results, showing distinct electrical properties for each antenna, are observed but not shown for brevity. Information about the electrical properties for each antenna is used to select the magnetic field generating circuit components.

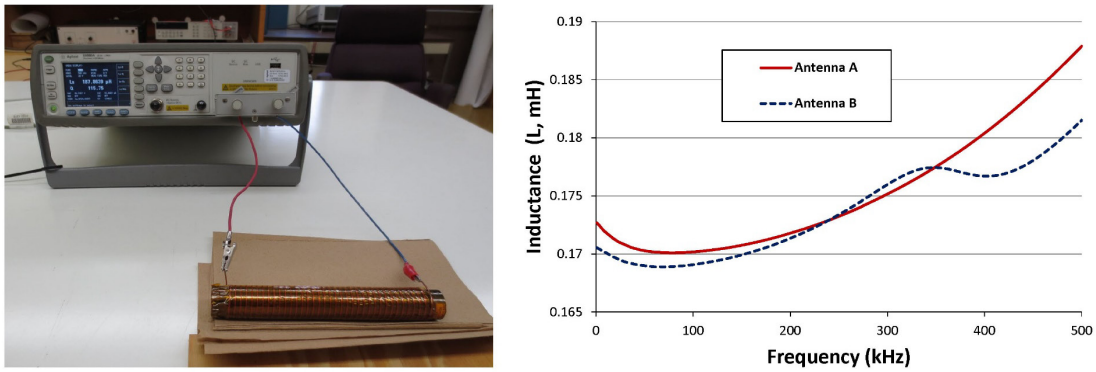

(a) **(b)**

Figure 3.4: Electrical Properties Testing Showing (a) LCR Meter Experimental Setup (a) and Resulting Inductance of the Ferrite Core Antennas

Independent circuits, with specific electronic components, are developed to produce stable and measureable magnetic fields based on the material properties of the ferrite-core antennas. Each circuit consists of resistive, inductive, and capacitive (RLC) elements connected in series that is tuned to the broadcasting frequency. Electrical resonance occurs in an AC circuit when inductive and capacitive reactances are opposite and equal, canceling each other out. In a series resonant circuit, the resonant frequency is defined as:

$$2\pi fL = \frac{1}{2\pi fC} \tag{3.1}$$

where f is the resonant frequency, L is the inductance, and C is the capacitance of the series resonant circuit. With the resonant frequency identified at 73 kHz and the inductance of

each ferrite-core antenna determined experimentally, the capacitance required for each circuit is determined through Equation (3.1). Standard electrolytic capacitors values are connected in parallel to achieve the total overall circuit capacitance required for resonance at the desired frequency. Each circuit also requires that sufficient electric current is supplied from one circuit component to another.

An impedance match is needed for the high-efficiency electrical energy transfer from the power amplifiers to the ferrite-core antennas. The impedance for a series RLC circuit is determined through the relationship:

$$Z = \sqrt{R^2 + \left(2\pi fL - \frac{1}{2\pi fC}\right)^2} \tag{3.2}$$

where R represents the total circuit resistance, and the other variables are the same as in Equation (3.1). The circuit resistance is determined experimentally with the capacitor bank and ferrite-core antenna connected in series to the LCR meter. The electric impedance between each amplifier and antenna pair is matched through the addition of a circuit transformer. The type of transformer required for the circuit is determined through the relationship between primary and secondary windings by:

$$N = \sqrt{\frac{Z_P}{Z_S}} \tag{3.3}$$

The transformer turn ratio N represents the number of turns on the primary coil to turns on the secondary coil. The transformer input primary coil impedance is represented by Z_P, and the output secondary coil impedance is denoted by Z_S. A Pulse PA0815NL transformer, with a 12-turn primary winding and two turn secondary winding, is applied to both circuits to match the impedance between the amplifier and ferrite-core antenna.

Each magnetic field generating circuit contains similar components. A schematic layout of the circuit components for the experimental magnetic field Generator 1 is shown in Figure 3.5 (a), and the schematic layout of the circuit components for Generator 2 is shown in Figure 3.5 (b). The same transformer is used for both circuits, but capacitors of various values are used to achieve the desired circuit response.

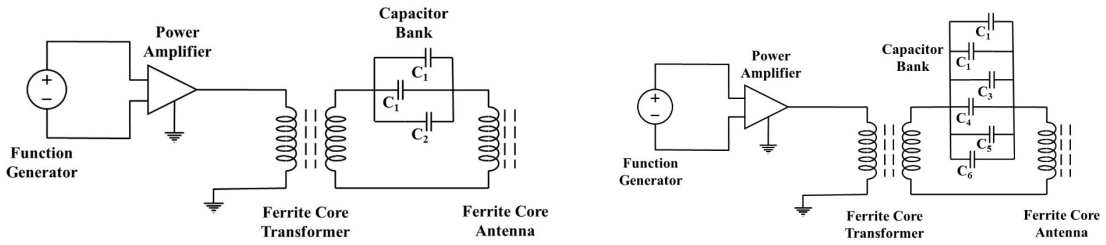

Figure 3.5: Circuit Diagrams for (a) Magnetic Field Generator 1, and (b) Magnetic Field Generator 2

A capacitor bank is designed for each circuit to ensure proper and efficient broadcasting of the magnetic fields. Table 3.1 shows the capacitor values used for the circuits displayed in Figure 3.5. The transformer and capacitors are arranged so that sufficient electric current flows through the ferrite-core antenna to produce the magnetic fields.

Table 3.1: Capacitor Values for Magnetic Field Generator Circuits

Capacitor	Value
C_1	10,000 pF
C_2	7,500 pF
C_3	5,100 pF
C_4	2,200 pF
C_5	220 pF
C_6	30 pF

Input and output signals must also be taken into consideration when designing the magnetic field generating circuit. Electric current across the ferrite-core antenna, measured by

the current transformers, does not affect the circuit design. However, the voltage supplied to each circuit is limited by the power amplifiers. An independent adjustable analog 73 kHz sinusoid input, with an adjustable amplitude of 0.1 mV_{rms} to 1 V_{rms}, is required for each circuit that is supplied by the software controlled signal generator.

These system subcomponents form the field generators, which are capable of producing stable and consistent magnetic fields. If the broadcasting frequency is modified, the circuit parameters change and different circuit components would be needed. This may in turn influence the input signal amplitude required to produce a stable magnetic field. The magnetic fields produced by the generators are the foundation of the shell-based model that is used to triangulate position.

3.3: Electromagnetic Field Distribution and Modeling

The generator circuits produce electromagnetic fields that are used to develop the shell based model. In addition, magnetic flux density data is collected to produce the shell based model. With a field invariant model established, the transferrable model is developed and demonstrated. Finally, position triangulation is investigated as a baseline for the control system implementation.

3.3.1. Magnetic Field Data Collection

Magnetic flux density measurements were collected at known positions around the magnetic field generators. Although the magnetic fields are three-dimensional in nature, only the 2-D case is considered here for simplicity. A diagram showing test setup and procedure for collecting magnetic shell data is displayed in Figure 3.6. Enough AC electric current needs to be supplied to the ferrite-core antenna to ensure that a stable magnetic field is produced. Radial lines in 5.5° increments were drawn from the center of the antenna for reference. The Gauss meter determines the intersections between the radial lines

and a constant value of magnetic flux density. Each measurement is manually recorded in Cartesian (B, x, y) and later converted to Polar (B, ρ, α) coordinates.

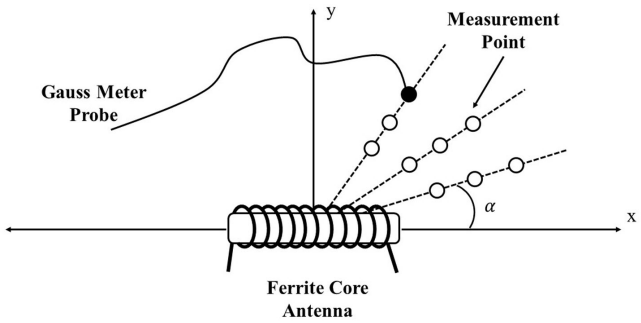

Figure 3.6: Schematic and Setup for 2-D magnetic flux density and location measurements

The points on each shell represents the distribution of constant magnetic flux density. An example of the shell-based measurements is shown in Figure 3.7. Measurements were collected to form a total of 16 constant magnetic flux density shells for each generator, which were placed at the origin. Each shell consists of 33 individual measurement points covering a total area of about 4 m^2.

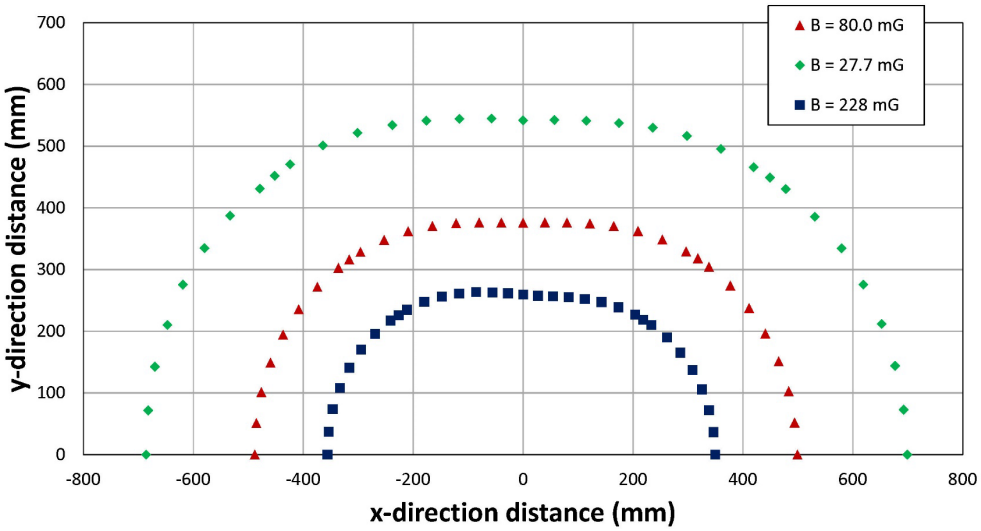

Figure 3.7: Example of Magnetic Shells from Generator 1 Measurement Data

Multiple data sets were collected to appropriately characterize the magnetic fields produced by each generator. The smallest shell for each generator is constructed at 300 mm

from the origin, and the largest is 1,100 mm from the origin. Each shell is incremented 50 mm larger than the previous shell. The magnetic flux density values ranged from 7.8 mG to 378 mG for Generator 1, and 7.6 mG to 404 mG for Generator 2. The largest value of magnetic flux density is associated with the smallest size shell in the data set. Conversely, smaller values of magnetic flux density are associated with larger shell sizes. The data also shows the nonlinear relationship between magnetic flux density and shell size.

The shell constants are determined through examination and analysis of the magnetic field data. The shell-based models for each generator are specific to the magnetic fields where the measurement data is collected. The magnetic field data collected for each generator determines the shell-model constants.

3.3.2. Determination of Shell Based Model

Multiple data sets are collected for each magnetic field generator that contain the information needed to determine the shell model parameters. A number of data sets M are constructed, each having a fixed magnetic flux density B and a number of measurement points N. Each individual measurement point is represented as $(B_j, \rho_{ji}, \alpha_{ji})$, where B_j is the constant magnetic flux density shell for data set j, ρ_{ji} is the i^{th} distance from the origin for data set j, and α_{ji} is the i^{th} angle from the origin for data set j.

The shell size and shape parameters are determined by examination and data processing of each magnetic shell data set. A least squares regression is used to uncover the shell model parameters a and b from Equation (2.15). The squared error R is defined as:

$$\mathrm{R} = \sum_{i=1}^{N} [\rho_i - (a\cos(2\alpha_i) + b)]^2, \qquad for\ i = 1,2,3,\ldots,N. \tag{3.4}$$

Minimizing the squared error in Equation (3.4), the optimum shell-size parameters a and b can be expressed as:

$$\begin{bmatrix} a \\ b \end{bmatrix} = \frac{\begin{bmatrix} N\sum_{i=1}^{N}\rho_i\cos(2\alpha_i) - \sum_{i=1}^{N}\rho_i\sum_{i=1}^{N}\cos(2\alpha_i) \\ \sum_{i=1}^{N}\rho_i\sum_{i=1}^{N}\cos^2(2\alpha_i) - \sum_{i=1}^{N}\rho_i\cos(2\alpha_i)\sum_{i=1}^{N}\cos(2\alpha_i) \end{bmatrix}}{N\sum_{i=1}^{N}\cos^2(2\alpha_i) - \left(\sum_{i=1}^{N}\cos(2\alpha_i)\right)^2}, \ldots \quad (3.5)$$

$$for\ i = 1,2,3,\ldots,N.$$

The size and shape coefficients are used to produce a shell function for the measured constant magnetic flux density data sets. The measured data is then compared to the shell based model. An example comparison of the measured magnetic shell and shell based model is shown in Figure 3.8, where the magnetic field generator is placed at the origin. Two different constant value magnetic flux density shells are compared for magnetic field generator 2. The dotted red shell has a constant measured magnetic flux density of 22 mG, while the dotted blue shell has a steady value of 108 mG. The shell-based model size and shape coefficients for the solid red line is a = 52.63 mm and b = 399.24 mm, and for the blue solid line is a = 78.94 mm and b = 675.62 mm, respectively. The model shows a good fit comparison to the measured data and can be used to uncover the shell-based model constant coefficients.

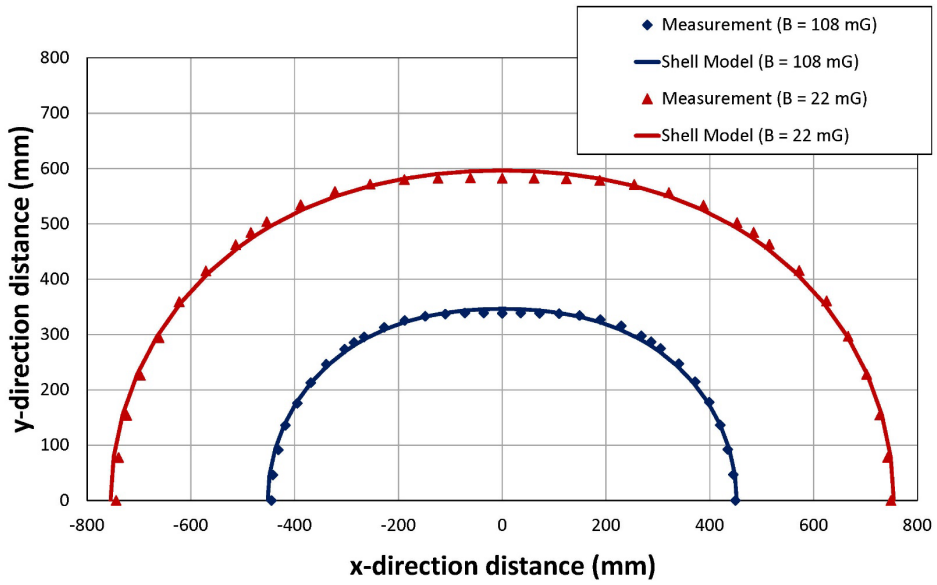

Figure 3.8: Comparison of Magnetic Generator 2 Measured Shells (points) and Shell Based Models (solid lines)

The shell-based model constant coefficients are determined by comparing the size and shape parameters against the magnetic flux density. The constant coefficients defined in Equation (2.16) are estimated through a regression fit with respect to B for each magnetic field generator. The shell-based model constants c_a, d_a, c_b, and d_b can then be determined through the relationship:

$$\begin{cases} c_a = \exp\left(\dfrac{\sum_{j=1}^{M}\ln a_j \sum_{j=1}^{M}\left(\ln B_j\right)^2 - \sum_{j=1}^{M}\left(\ln B_j\right)\sum_{j=1}^{M}\left(\ln a_j \bullet \ln B_j\right)}{M\sum_{j=1}^{M}\left(\ln B_j\right)^2 - \left(\sum_{j=1}^{M}\ln B_j\right)^2}\right) \\ d_a = \left(\dfrac{\sum_{j=1}^{M}\ln a_j \sum_{j=1}^{M}\ln B_j - M\sum_{j=1}^{M}\left(\ln a_j \bullet \ln B_j\right)}{M\sum_{j=1}^{M}\left(\ln B_j\right)^2 - \left(\sum_{j=1}^{M}\ln B_j\right)^2}\right) \\ c_b = \exp\left(\dfrac{\sum_{j=1}^{M}\ln b_j \sum_{j=1}^{M}\left(\ln B_j\right)^2 - \sum_{j=1}^{M}\left(\ln B_j\right)\sum_{j=1}^{M}\left(\ln b_j \bullet \ln B_j\right)}{M\sum_{j=1}^{M}\left(\ln B_j\right)^2 - \left(\sum_{j=1}^{M}\ln B_j\right)^2}\right) \\ d_b = \left(\dfrac{\sum_{j=1}^{M}\ln b_j \sum_{j=1}^{M}\ln B_j - M\sum_{j=1}^{M}\left(\ln b_j \bullet \ln B_j\right)}{M\sum_{j=1}^{M}\left(\ln B_j\right)^2 - \left(\sum_{j=1}^{M}\ln B_j\right)^2}\right) \end{cases}, \ldots \quad (3.6)$$

$$for\ j = 1,2,3,\ldots,M.$$

The nonlinear relationship between shell size and magnetic flux density requires a large number of data sets to ensure accuracy. The $M = 16$ data sets of constant magnetic flux density shells are used to produce the model contestants. An example of the model parameter accuracy is shown in Figure 3.9 for the Generator 1 shape constant a. The shell-shape constants c_a and d_a are obtained from Equation (3.6) and used in Equation (2.16) to obtain the shell shape function. The 16 shape constants (red square) and shell equation (blue line) are compared in Figure 3.9. A similar relationship can be observed for the size constants c_b and d_b for Generator 1. These shell constants can now be used to describe an arbitrary magnetic field around the ferrite-core generator. The same procedure can be used to find the constant coefficients for magnetic field Generator 2.

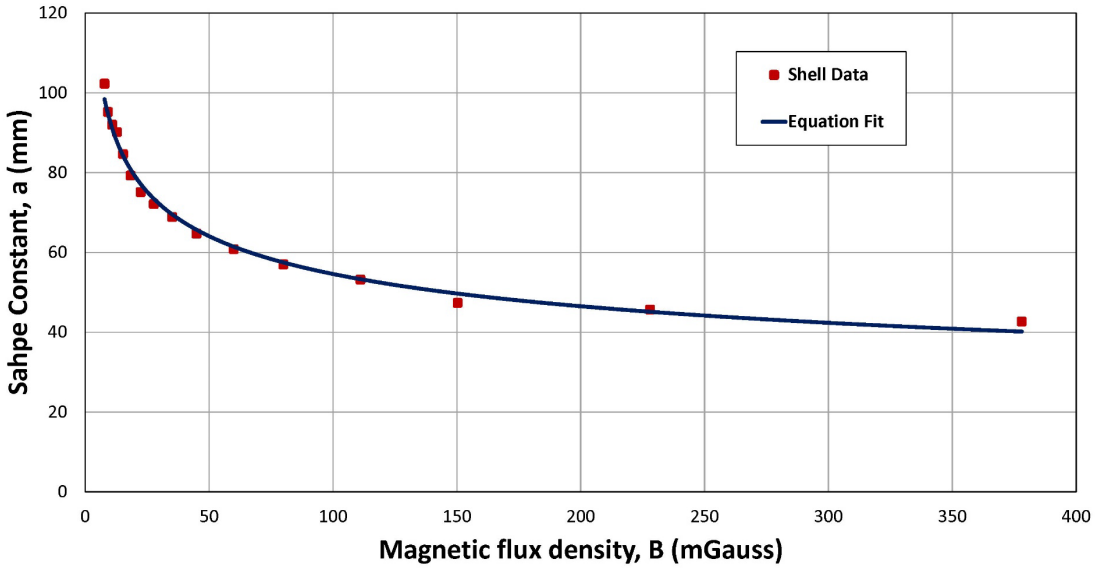

Figure 3.9: Example of Shell Model Accuracy for Generator 1 Size Parameter

The magnetic field data is used to produce an accurate invariant field distribution model for both experimental magnetic field generators. The model shape and size coefficient constants, used by Equation (2.15) to describe the magnetic fields, are shown in Table 3.2. The electric current, kept the same for simplicity during model setup, is also displayed in the table.

Table 3.2: Shell Based Model Parameters for Experimental Proximity Detection System

Parameter	Generator 1	Generator 2
c_a	158.14 mm	159.87 mm
d_a	0.231 mm	0.228 mm
c_b	1,886.1 mm	1,184.5 mm
d_b	0.331 mm	0.332 mm
I	2.835 A	

The model is only valid for a specific steady state applied electric current across the ferrite core antennas. If the electric current fluctuates in magnetic field generator circuits, then the shell based model loses accuracy. The transferable field variant model addresses

changes in magnetic field generator electric current, but only in the linear portion of the magnetic flux density and current relationship. Subsequently, this in can affect performance of the proximity system to appropriately define safety zones and triangulate position.

3.4: Experimental Position Triangulation

The shell-based model can be used to triangulate position for a proximity detection system. To determine the triangulated position of the sensor using the experimental system, each generator produces a magnetic field asynchronously. The same electric current is applied to the ferrite core antennas that was used during the shell model development. The sensor data is used to produce a constant magnetic flux density shell specific to each generator. The sensor is then found at the location of two intersecting magnetic shells.

A common coordinate system is used to examine the performance of the experimental system. A triangular point grid of known locations is constructed between the two magnetic field generators. At each grid point measurement location, the Gauss Probe measures the magnetic flux density for each field generator independently. The intersections of the magnetic fields are compared to the actual grid location to assess performance.

The localization performance of the experimental two-generator system is quantified by comparing the calculated position and the actual grid point measurement location. An example of this comparison is shown in Figure 3.10. The actual predetermined measurement locations form a triangle (blue dots). This measurement pattern insures unique measurement locations with respect to both generators. The shell intersection locations are also displayed on the chart (red x marks) for comparison against actual measurement locations. The shell-based model accurately determines the sensor location. The shell

based magnetic model intersections have an average of 1.5% error difference from the known measurement locations.

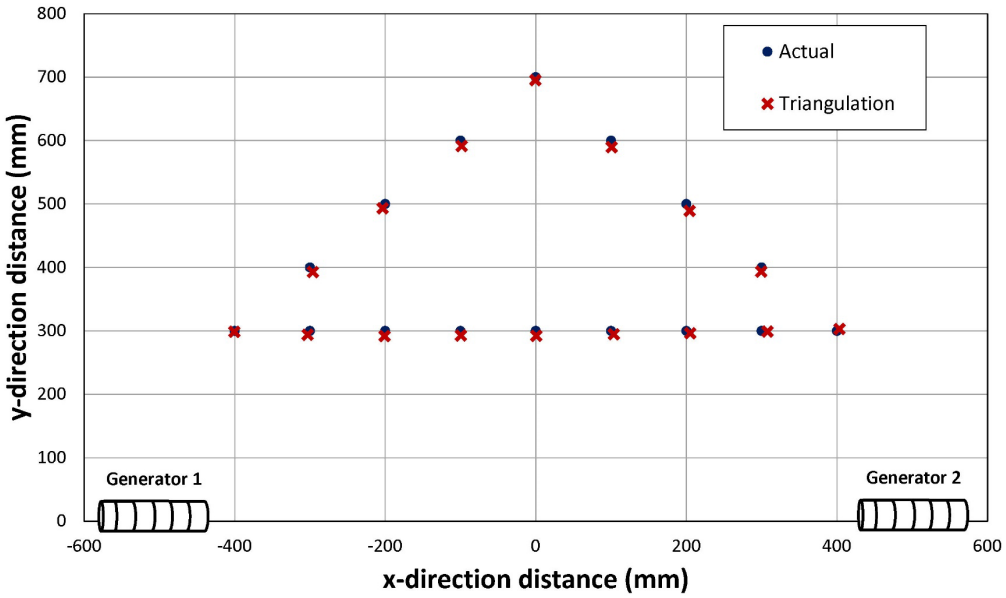

Figure 3.10: Comparison of Actual Measurement Locations (blue dot) and Shell-Based Triangulation (red x)

Variation in electric current can have an adverse effect on the shell based model and diminishes triangulation accuracy. Electric current fluctuations can be caused by the non-linear components of the power amplifier, environmental changes, and as changes in temperature occur. Even simple changes, such as manually adjusting current during field calibration of deployed systems underground, can lead to degraded performance. To demonstrate this phenomena, only the electric current supplied across ferrite-core antenna 1 is increased from 2.835 A to 3.181 A. The resulting magnetic shell intersections and measurement locations are shown in Figure 3.11. The error between measurement locations (blue dots) and triangulated position of the magnetic field sensor has increased to an average of 8%. This error is expected to be greater for larger differences in supplied electric current between the magnetic field generators.

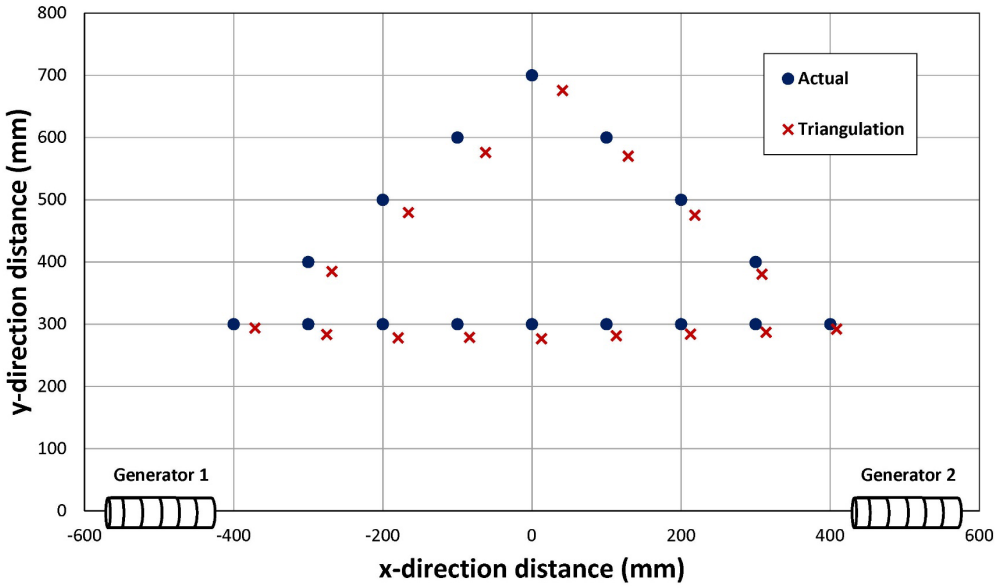

Figure 3.11: Shell Based Triangulation with Uncompensated Increase in Electric Current

If no compensation is made, inconsistent current supplied to the ferrite-core antennas will result in an incorrect calculation of sensor locations. The magnetic field can be changed or adjusted to a desirable distribution by modifying electric current supplied to the magnetic field generating circuit. Within the linear region of the B and I relationship, the transferable shell-based field invariant mode can be applied. Figure 3.12 shows the results of the transferable model of Equation (2.21) being applied to the experimental system. The electric current modification is compensated for, and the triangulation accuracy from the shell-based model is improved. An average percent error difference of 1.5% between the actual measurement locations and calculated locations is observed.

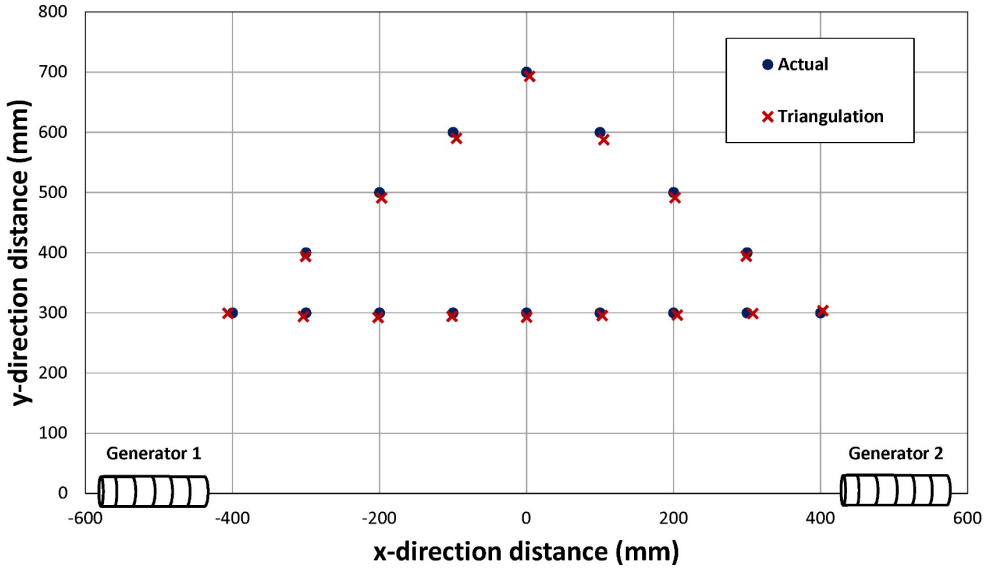

Figure 3.12: Application of the Transferrable Shell-Based Model to Triangulate Sensor Position

While the field variant transferrable model can improve the position triangulation of proximity detection systems, it has some limitations. The magnetic flux density and electric current relationship is physical property unique to each field generator. Therefore, the transferrable model is best used to adjust proximity detection magnetic fields to environmental influences that are reasonably constant. Another limitation is the transferrable model requires a known sensor and measurement location to compensate the system. Variations of magnetic field generator electric current is better regulated by more tradition control system approaches.

3.5: Pulsed Magnetic Fields

Commercial proximity detection systems used for underground mining equipment operate differently than the experimentally developed system. While the examples from the previous section show how the experimental system can be used to set up safety zones and triangulate position, it does not represent an important characteristic of how commercial systems work. The presence of a magnetic field from one generator can influence the

size and shape of the magnetic field produced by another generator. To overcome this issue, commercial systems use sequenced pulsed signals to prevent multiple magnetic field generators from distorting the safety zones around the machine.

While the use of pulsed signals is a necessary feature of commercial proximity systems, it is not fully integrated into the experimental system. Using a pulsed signal would inhibit the development of a shell-based magnetic field model. Since the experimental system can be operated asynchronously to determine sensor location, the capability to pulse the magnetic field signal adds unnecessary complexity. However, use of a pulsed signal is an important component to consider for the examination of proximity detection system performance. Environmental influences, such as temperature, need to be examined with a pulsed signal deployed.

Characteristics of the pulsed magnetic generator signal are determined experimentally on a commercial proximity detection system. Figure 3.13 shows the experimental test setup on a proximity detection system installed on a Joy 14CM-9. Tests were conducted on the surface in an area free of environmental influences such as other equipment or machinery. A single turn loop antenna was constructed and connected to a Tektronix RSA5100A Real-Time Signal Analyzer (s/n: XXXX). While these measurements do not relate the exact electric current across the generator circuit, it does measure induced voltage that is proportional to magnetic flux density and provides valuable information about the signal.

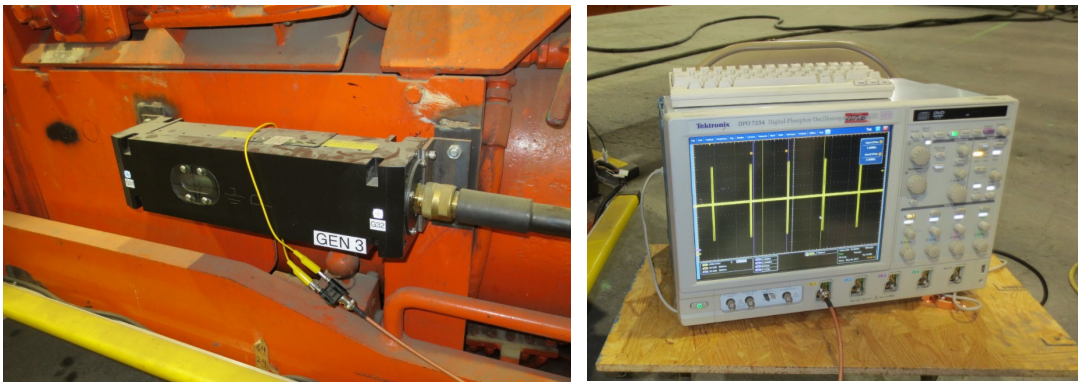

Figure 3.13: Experimental Setup to Determine Pulsed Signal on a Commercial Proximity Detection System

Important signal characteristics such as rise time, pulse width, transient decay, and timing can be determined by examination of the test results. The plot shown in Figure 3.14 (a) displays one second of time data, which corresponds to five pulse peaks. Further inspection of the data, shown in Figure 3.14 (b), shows each peak contains two pulses. The duration of each pulse is roughly 0.3 milliseconds, and each peak is approximately 0.2 seconds apart. This information is used to create a pulsed signal for the experimental system

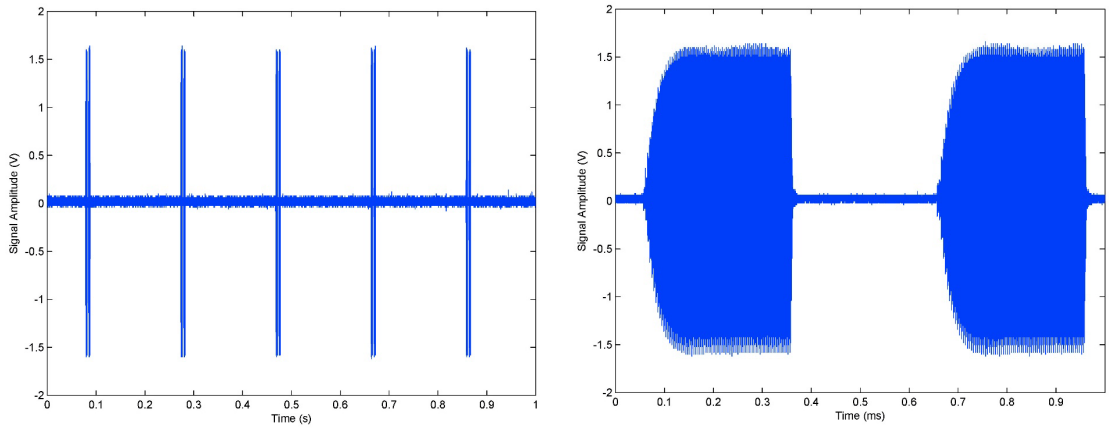

(a) **(b)**

Figure 3.14: Commercial Proximity Detection System Magnetic Field Signal (a) over One Second and (b) Expanded View of Two Pulse Peaks.

The capability to produce pulsed magnetic fields was created for the experimental system based on the observed characteristics of the commercial system. The experimental system pulsed magnetic field output signal, as measured by the CT (blue line), is displayed in Figure 3.15. Also shown in Figure 3.15 is the input signal to the power amplifier (orange line) for comparison purposes. The timing and amplitude of the experimental system pulsed magnetic field signal closely resembles the characteristics of the commercial proximity detection system magnetic field signal. However, there are some observed differences between the signals produced by the two systems. Some of differences can be attributed to variability in the material properties of the ferrite-core generators. Others dissimilarities are attributed to how the electronic components are configured.

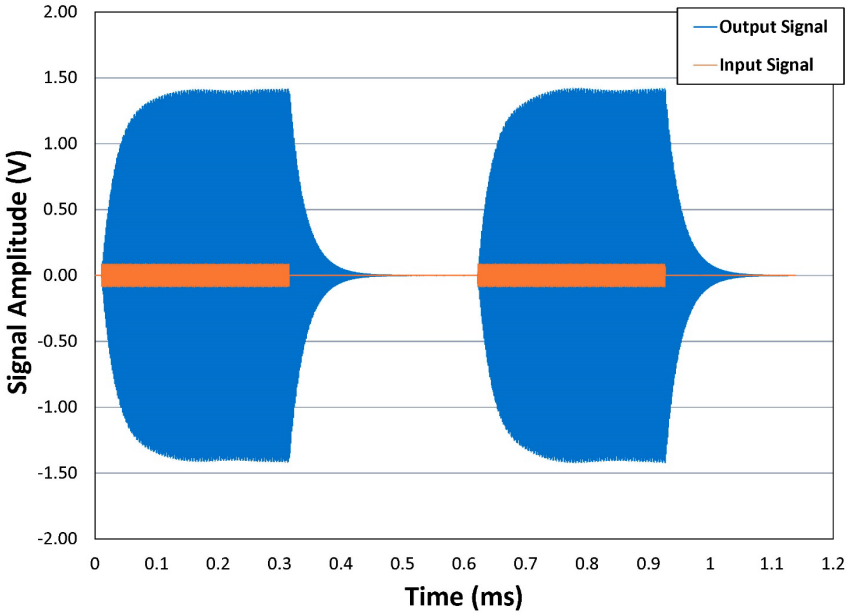

Figure 3.15: Experimental Proximity Detection System Pulsed Magnetic Field Signal

The ideal magnetic field signal is a rectangular pulse with equal positive and negative components. This ideal signal is difficult to achieve due to the electronic components used within magnetic field generating circuit. The experimental system has a significant transient decay response, as shown in Figure 3.15. Commercial proximity detection systems deploy a shunt to the power absorbing components that can reduce the transient response of the signal, as displayed in Figure 3.14 (b). However, this approach has no effect on the rise time, which is observed to be uniform between the two systems. These characteristics are important to quantify and understand in relation to the development of a control system approach.

3.6: Effect of Temperature on Magnetic Field Generation

There are a number of environmental influences that affect the size and shape of the magnetic fields produced by proximity detection system generators. The influences of many environmental factors have been studied for proximity detection systems used in underground coal mines[79, 92]. Temperature within an underground mine environment can

fluctuate drastically [93]. However, it is not known how temperature variation affects the performance of proximity detection systems used in underground mines.

The experimental system has been configured to examine the effect of temperature on the magnetic fields produced by the generators. The temperatures of magnetic field generators were monitored using Type J thermocouples bonded to the surface of the ferrite-core antennas. The magnetic field generator current was measured using a CT probe, as described in the previous sections.

The relationship between magnetic field generator current and temperature can vary significantly. An example of this relationship is shown in Figure 3.16. An input signal of 2.52 V at 73 kHz was supplied to the power amplifier, which corresponds to an initial value of 6.65 A across the magnetic field generator. The surface temperature of the ferrite-core antenna (blue line) follows the response of a first order system. The electric current across the magnetic field generator (yellow line) initially increases and then decays uniformly until the temperature reaches steady state. The observed difference between the maximum and minimum current is 1.1 A, which is a significant variation across the magnetic field generating circuit.

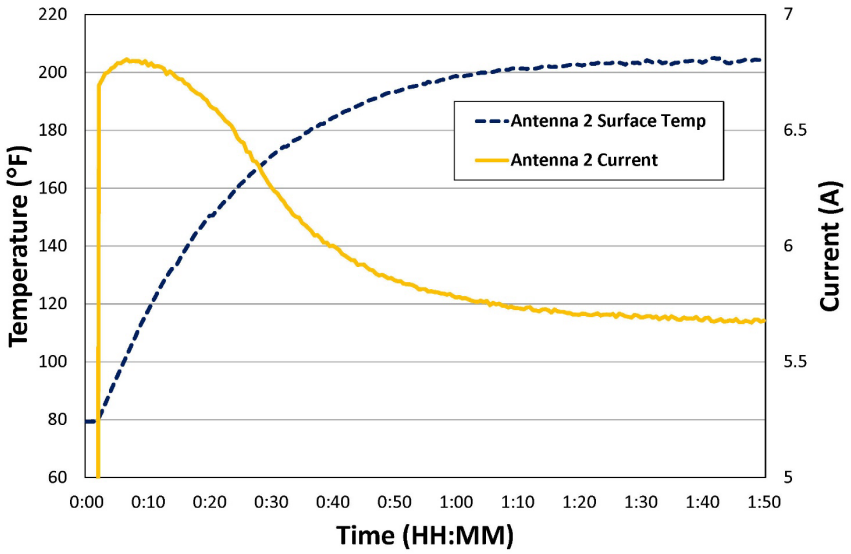

Figure 3.16: Generator 2 Surface Temperature vs Current

Variation between generator current and temperature can have a profound effect on the magnetic field produced. To demonstrate this, the magnetic field shells produced from the minimum and maximum electric current values, during the temperature rise to steady state in Figure 3.16, are displayed in Figure 3.17. The smaller shell (solid green line) corresponded to the minimum electric current observed at 5.7 *A* when the surface temperature reached steady state. The larger shell (dashed turquoise line) coincides with an electric current observed at 6.8 *A* when the system was initially turned on. The difference between the minimum electric current shell and the maximum electric current shell is at intervals of 6.0% and 6.5%, depending on location. The same general observations are made for Generator 1, but are not shown here for brevity.

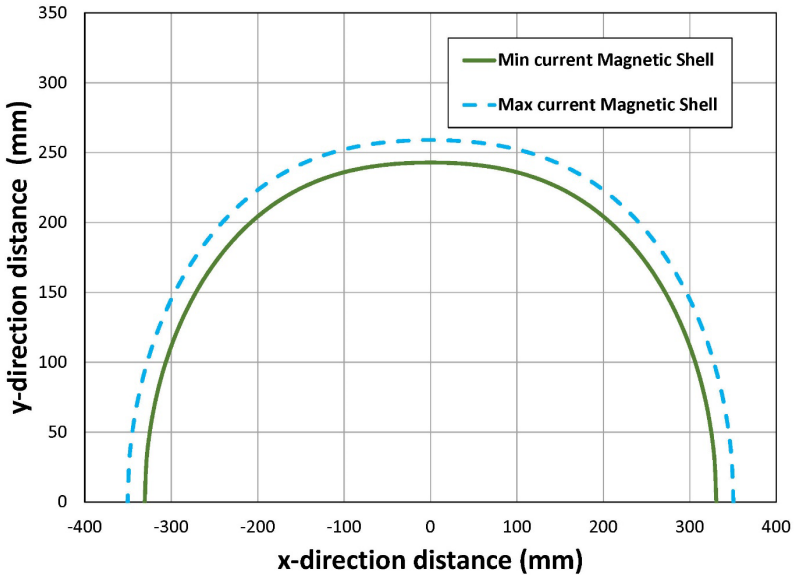

Figure 3.17: Magnetic Shells Produced During Temperature for Generator 2

Inconsistent magnetic fields can be problematic for electromagnetic based proximity detection systems. While the example above focuses on temperature change that is a function of the ferrite-core antenna material properties, other environmental influences can also affect the temperature and performance of proximity detection systems. Ambient temperature in an underground coal mine is dependent on many factors, such as depth and ventilation air flow, and can influence the size and shape of the magnetic fields used

by an electromagnetic proximity detection system. Not only will this affect the performance of traditional magnetic field-based systems, but also zone-based systems employing triangulation and selective shutdown logic.

Examining the effect of cooling to an ambient temperature, while using a pulsed signal, will further demonstrate the effects of environmental influences on the magnetic field generators. This is a more realistic scenario of what underground commercial proximity detection will experience, while using the experimental system in a laboratory environment. Again, a 2.52 V 73 kHz sinusoidal signal was supplied to the power amplifier. Using the pulsed signal developed in the previous section, the ferrite-core antenna in Generator 2 was brought to a constant and steady surface temperature 180 °F. A 36-Quart Kool thermoelectric cooler (same used for the capacitor banks) kept the ambient temperature constant at 35 °F. Once the ferrite-core antenna reached a constant surface temperature, it was placed in the cooler to observe the electric current and temperature changes.

As with the previous case shown in Figure 3.16, significant changes are observed between electric current across the magnetic field generator and the surface temperature of the ferrite-core generator. The results of using a pulsed magnetic field signal while cooling to a constant outside ambient temperature is shown in Figure 3.18. The ferrite-core antenna of magnetic field Generator 2 (blue dashed line) exponentially decays to a constant surface temperature. The electric current across the magnetic field generator (orange line) quickly increases to compensate for the change in temperature and then remains uniform until the temperature reaches steady state. The observed difference between the maximum and minimum current is again 1.1 A. This difference will introduce errors between the magnetic field expected and the magnetic field produced by the magnetic field generator.

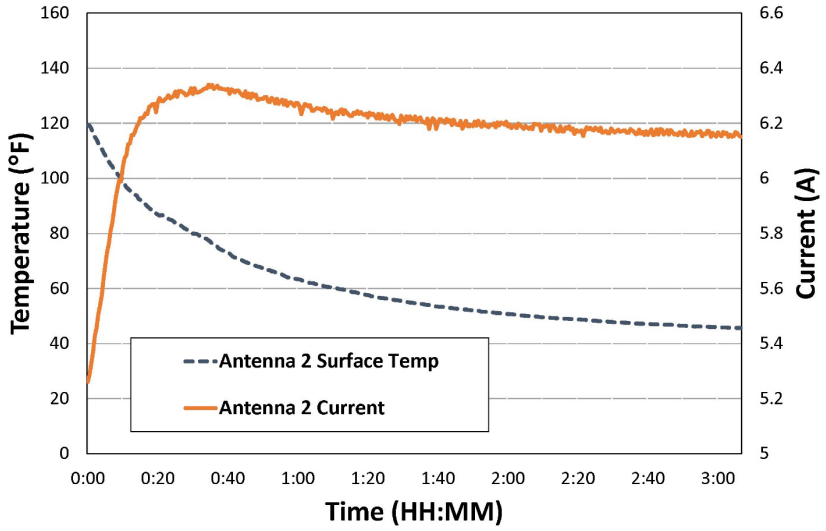

Figure 3.18: Temperature Change of Generator 2 using a Pulsed Magnetic Field Signal

Changes in temperature can influence the electric current across the magnetic field generators used in underground proximity detection systems. These influences can affect the performance of proximity systems by introducing inconsistent magnetic fields. If the generator is not producing a strong enough magnetic field, the safety zones might not provide adequate protection. Similarly, systems relying on position triangulation and intelligent machine shutdown will not function properly. Field adjustments can be made to compensate, but underground mine temperature fluctuates between work shifts and day to day. These errors can, however be overcome through the implementation of a control system to limit electric current fluctuations.

Chapter 4: Control System Design and Simulation

This chapter will focus on the development of a control system that governs input to the experimental electromagnetic field generators. The system components and architecture are defined to develop the proposed closed-loop system. Analytic approximations of the electromagnetic field generating circuits are established to model the behavior of the system. A controller is developed through simulation that provides an improved signal to the electromagnetic field generating circuits. Design parameters for the proximity system are further examined through simulation. The simulated response of the controlled system is compared and contrasted to the simulated open-loop system. The controller developed in this chapter will be the basis for the control system to be applied on the experimental electromagnetic system.

4.1: Electromagnetic Proximity System Numerical Model

A numerical model is developed of the experimental two-generator system from the previous chapter. The governing equations describing the magnetic field generators are determined by examining the electronic circuit components. The schematic shown in Figure 4.1 describes the general electronic component layout used for each magnetic field generator circuit. The diagram contains the simplified circuit elements that define the generator components used to produce each magnetic field. The impedance matching transformer elements of the experimental systems are denoted by the subscript *T*. The magnetic field generating components of the ferrite core generator is designated by the subscript *G*.

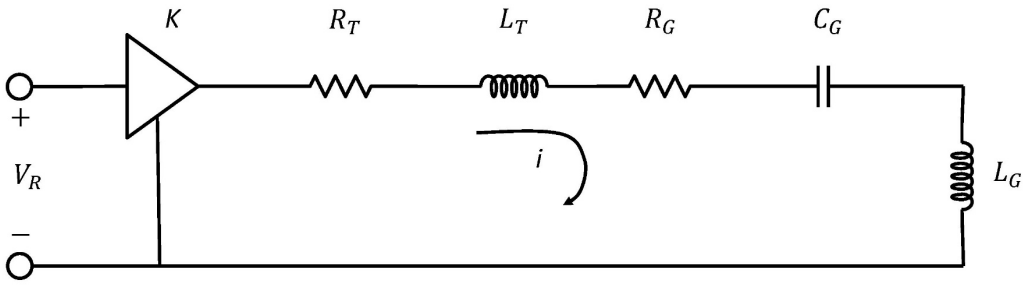

Figure 4.1: Magnetic Field Generator Circuit Diagram

To determine the input/output relationship of the magnetic field generating circuit, the voltage drop across each element is expressed as:

$$R_T i(t) + L_T \frac{di(t)}{dt} + N^2 R_G i(t) + \frac{N^2}{C_G} \int i(t)dt + N^2 L_G \frac{di(t)}{dt} = K V_R(t) \quad (4.1)$$

where I and V_R represent the circuit current and supplied voltage, respectively. The constant gain value, K, is supplied by the power amplifiers. The circuit's transformer resistive and inductive elements are represented by R_T and L_T, respectively. The components R_G, C_G, and L_G denote the resistive, capacitive, and inductive elements of the magnetic field generating circuit. The ratio of primary to secondary transformer windings is represented by N, which is 6 for both circuits. Equation (4.1) represents a second-order homogenous linear differential equation with constant coefficients

Rearranging Equation (4.1) and converting to the frequency domain yields:

$$\frac{I(s)}{V_s(s)} = \frac{K}{R_T + \boldsymbol{s}L_T + N^2 R_G + {}^{N^2}/_{\boldsymbol{sC}} + \boldsymbol{s}N^2 L_G} \quad (4.2)$$

Further simplification and rearranging of Equation (4.2) produces the transfer function:

$$\frac{I(s)}{V_s(s)} = \frac{Ks}{s^2(L_T + N^2L_G) + s(R_T + N^2R_G) + {N^2}/{C}} \tag{4.3}$$

Several important characteristics of the magnetic field generating circuit can be determined by examining the system's transfer function. The transfer function displayed in Equation (4.3) describes the behavior and response of a series resonant RLC circuit. Determination of the system poles reveals three distinct cases. If the characteristic equation contains two different real poles, then the system will be overdamped. The system will be critically damped if the poles are real and repeated. Finally, if the poles are complex, then the system will be underdamped. The numerator of Equation (4.3) displays a zero at the origin, which will also affect the steady state response.

The resistive, capacitive, and inductive circuit components were determined experimentally, as described in the previous chapter. The measured values for each magnetic field generating circuit are displayed in Table 4.1. These values are incorporated into the transfer function in Equation (4.3) to obtain the numerical representation of each magnetic field generating circuit.

Table 4.1: Experimentally Measured Circuit Component Values

Variable	Generator 1 Value	Generator 2 Value
R_T	0.2179 Ω	
L_T	1.8177 x 10^{-6} H	
K	52.6	51.6
R_G	0.6395 Ω	0.7589 Ω
C_G	2.7820 x 10^{-8} F	2.7912 x 10^{-8} F
L_G	1.7011 x 10^{-6} H	1.6890 x 10^{-6} H

The damping ratio and undamped natural frequency are determined by values of the circuit components, and establish which response the system will exhibit. The system damping is determined through the values obtained in Table 4.1 and the general RLC series circuit relationship:

$$\zeta = \frac{R}{2}\sqrt{\frac{C}{L}} \tag{4.4}$$

where the variables in Equation (4.4) represent the total values measured for each circuit component. The undamped natural frequency is a design criteria and the sinusoidal input to the system. Examination of the poles in Equation (4.1) with the values inserted from Table 4.1 reveals that both systems have complex real roots and display an underdamped transient response.

The numerical model transfer functions are compared to the experimental system developed in the previous chapter. A Matlab computer program was written to model Equation (4.4) and simulate the magnetic field generating circuits (See Appendix B). A frequency response is generated by the experimental system and then compared to the numerical frequency response function (FRF). The results of the experimental frequency response are shown in Figure 4.2 (a), and the results of the numerical FRF are shown in Figure 4.2 (b). There is close agreement between the measurement and simulation of magnetic field Generator 1 (solid blue line) and Generator 2 (dashed green line). The resonant peak and phase shift at 73 kHz is recognized for both the experimental and numerical systems. Slight variation observed in the experimental frequency response of Generator 2 is due to the material properties of the ferrite-core antenna. The numerical approximation of the experimental magnetic field generators is the basis for the development a control system approach.

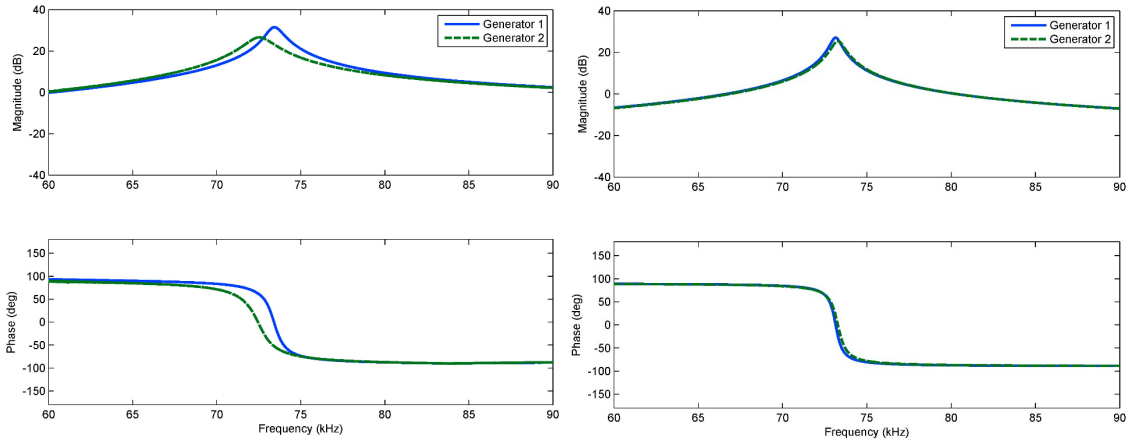

(a) **(b)**

Figure 4.2: Frequency Response of Magnetic Field Generator (a) Experimental System (b) Numerical Model

An important parameter that influences the response of the circuit can be derived from the magnitude of the frequency response at resonance. The Quality factor, Q, is a measure of the resonant peak "sharpness" at the driving frequency. The maximum energy stored in the circuit to the energy dissipated during each cycle of oscillation is related to Q, and is defined as:

$$Q = \frac{1}{R}\sqrt{\frac{L}{C}} \tag{4.5}$$

Equation (4.5) is closely related to the circuit damping ratio and natural frequency. The ability to reject any frequencies outside of the resonant peak bandwidth is determined by the Quality factor. A more selective magnetic field generating circuit will have a narrower bandwidth whereas a less selective circuit will have a wider bandwidth. In addition, the time required for a series resonant circuit to reach full amplitude takes approximately Q cycles.

To further validate the numerical model, the system response to a pulsed sinusoidal input is examined. An input signal similar to the one defined in Section 3.5 is used to simulate the numerical model. The results of the numerical simulation are displayed in Figure 4.3

for magnetic field generator 1. The output signal (blue line) represents a numerical approximation of the signal measured by the CT in the experimental system. The input signal (organ line) represents a numerical approximation to the signal being sent to the power amplify. The numeric results shown in Figure 4.3 closely resemble the experimental magnetic field pulses displayed in Figure 3.15.

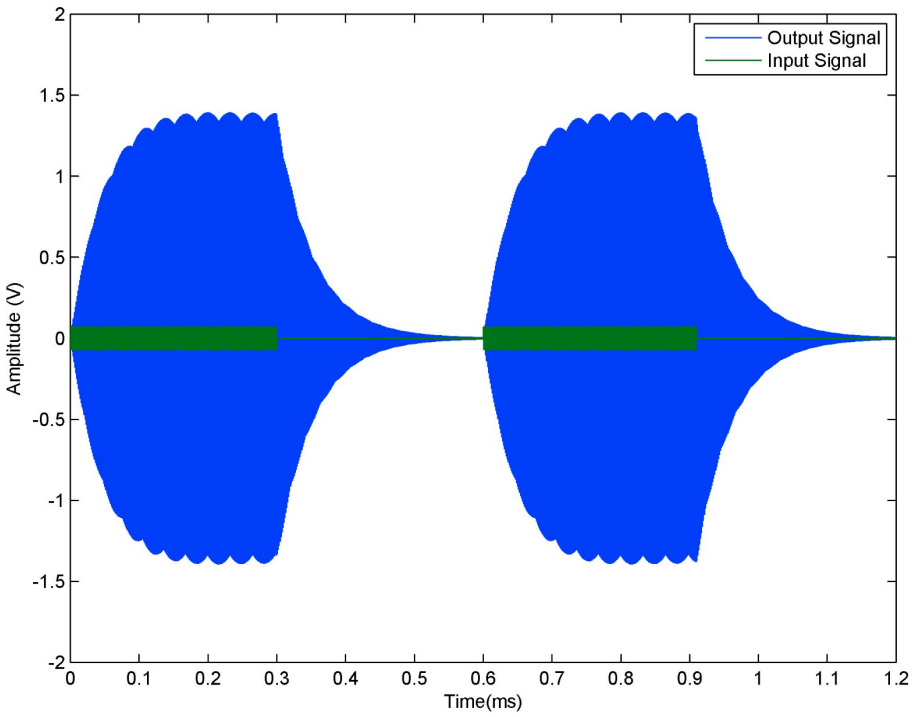

Figure 4.3: Simulated Pulsed Magnetic Field Signal for Generator 1

System response to a pulsed sinusoidal input is an important consideration when developing and evaluating control system strategies. However, other input types provide a better prediction of global system stability and performance. The overall control system performance will be evaluated on the ability to reduce rise time and settling time of the circuit response to the 73 kHz sinusoidal input. With the development and verification of the magnetic field generator numeric models, simulations can be used to develop the control system.

4.2: Control System Development

The input/output relationship developed in the previous section determines how the magnetic field generating system will behave and the desired performance required of the controller. The system damping determines which response will be observed (overdamped, underdamped, or critically damped), with the resonant frequency held constant. Several important transient characteristics can be determined by examining the unit step response. The overall design criteria for the controller is to reduce the settling time, preserve or slightly improve the peak response, and maintain an acceptable quality factor. The natural frequency of the system must also match the input signal frequency of 73 kHz, so the sufficient current is supplied to the ferrite-core antenna.

The control system is developed by first considering the unit step response of the magnetic field generating circuit. Figure 4.4 shows the unit step response of the uncompensated system for magnetic field generator one. Due to the numerator of Equation (4.3), the system response to a unit step input is zero at steady state. After the peak amplitude is achieved, the system oscillations decay exponentially to a final value of zero. The circuit designed for the second magnetic field generator demonstrates identical characteristics, but is not shown for brevity.

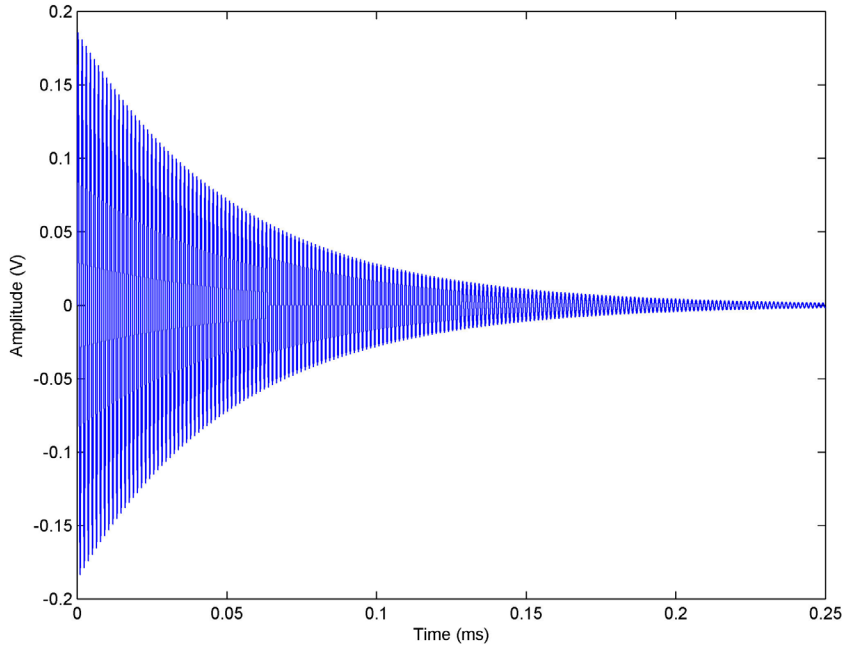

Figure 4.4: Simulated Unit Step Response of Generator Circuit 1

The magnetic field generating series resonant circuit requires sufficient energy input without DC bias offset, which can saturate the inductors. However, the long settling time in relation to the input sine wave pulse is responsible for the undesirable transient response shown in Figure 4.3. While the uncompensated system can accurately track reference input, it also has poor disturbance rejection as demonstrated by the temperature variation in Section 3.6.

A feedback controller architecture is examined to improve the magnetic field generating circuit system performance. Figure 4.5 shows a block diagram schematic of the feedback control system and is used to develop the closed-loop transfer functions. The reference input is represented by *R(s),* and the system output is represented by *Y(s)*. The generator circuit disturbance corresponds to *W(s)*, while *V* relates the current probe sensor noise.

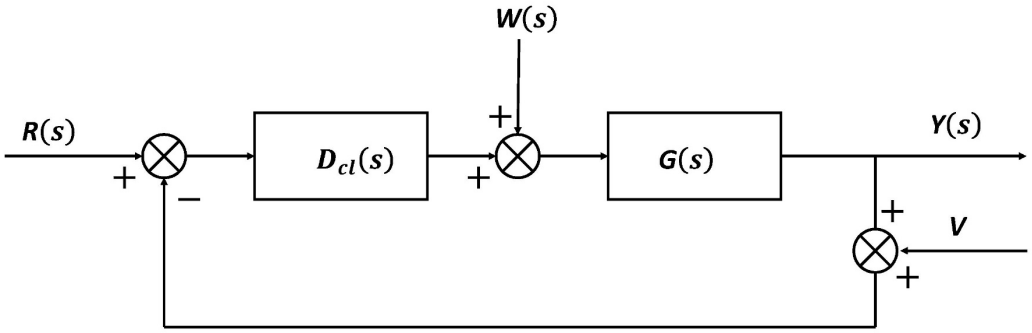

Figure 4.5: Control System Architecture

These relationships are used to analyze the control system architecture and develop the basic control equations for the feedback system. The closed-looped transfer function for the magnetic field generating feedback system is defined by:

$$\frac{Y(s)}{R(s)} = \frac{D_{cl}(s)G(s)}{1 + D_{cl}(s)G(s)} \tag{4.6}$$

The poles and zeroes of the closed-loop transfer function are examined in relation to transient response characteristics. The Root locus plot of the circuit transfer function is shown in Figure 4.6. A polar grid with lines of constant radial damping and angular natural frequency is used to determine proportional gain values that could improve system performance. The infinite gain relationship between the system complex poles (blue x marks) and zero (blue circle) is displayed, and can be used to infer dynamic properties of the closed-loop system. The complex conjugate poles are shown on the Left Hand Plane (LHP) with the numerator zero at the origin. The pole/zero placement determines the Root Locus path, where increasing gain follows the 73 kHz radius until a damping factor of unity is reached.

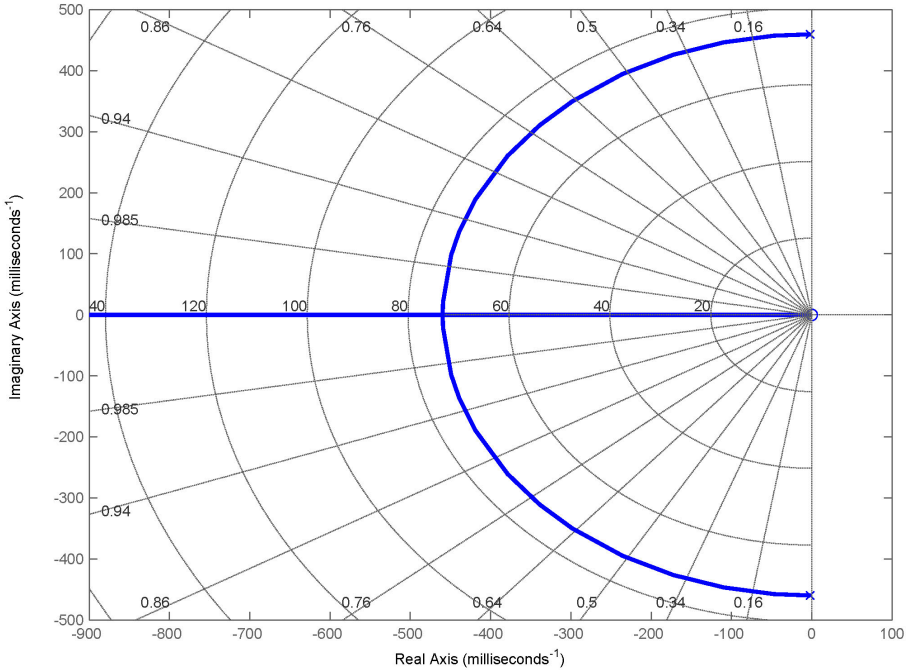

Figure 4.6: Root Locus of Magnetic Field Generating Circuit

Several proportional gain values are identified that could improve the performance of the magnetic field generating circuit. To evaluate these values, the unit step and frequency response is examined. Figure 4.7 shows the unit step response (a) and frequency response (b) with several different values of proportional gain. Less than unity (blue line), unity (green line), and greater than unity (red line) values of proportional gain are considered.

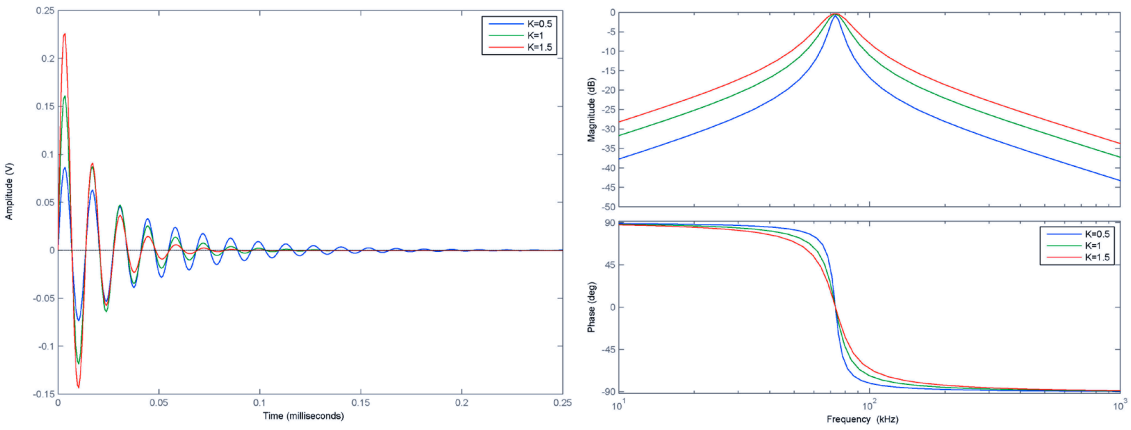

Figure 4.7: Unit Step (a) and Frequency Response (b) of Closed-Loop System with Proportional Gains

Several observations can be made by examining the step and frequency response simulations using different proportional gain values. The gain values and resulting time response characteristics, as well as the frequency domain Quality Factor, are displayed in Table 4.2. As the settling time, T_s, decreases, the peak response, P_k, increases. However, this improvement in performance comes at a cost of the band-pass filter quality factor, Q. As the quality factor is decreased, the "sharpness" of the resonant peak will become broader. This will result in less-efficient energy transfer between the amplifier and ferrite-core antenna, and potentially allow noise to enter the system.

Table 4.2: Proportional Gain Closed-Loop Performance Characteristics

Gain, K	Quality Factor, Q	Settling Time, T_s	Peak Response, P_k
Open-Loop	121.13	1.731 ms	0.183 V
0.5	9.83	0.168 ms	0.086 V
1	5.12	0.087 ms	0.161 V
1.5	3.46	0.059 ms	0.226 V

By implementing feedback control, the closed-loop system error is less sensitive to plant gain variation than the open-loop system. However, further inspection of the closed-loop transfer function reveals important information about overall system error. Since the system is type 0, the circuit output has a constant steady state error for a unit step input reference tracking. Furthermore, the system is also type zero for disturbance rejection and will also have a constant steady state error for a unit step input. Reference tracking and disturbance rejection can be improved by adding an integral term to the proportional controller.

A proportional integral (PI) controller is developed to improve the performance and response of the magnetic field generating circuits. Using a proportional controller produces an output that is commensurate with the system error. Adding an integral control to the proportional controller integrates the error over a time period and reduces the steady state

error. A derivative term for the controller is not needed due to the system stability and required rise time response to the reference input. The PI controller is implemented of the form:

$$D_{cl}(s) = K_p + \frac{K_i}{s} \tag{4.7}$$

Where K_p is the proportional gain tuning parameter, and K_i is the integral gain tuning parameter. The controller gain values are determined by examining the Root locus infinite gain relationship of the closed-loop system.

To determine appropriate gain values, the Root locus of the PI controller and magnetic field generating plant is examined. The Root locus of the controller and plant is shown in Figure 4.8. The real pole of the PI controller is placed close to the origin of the real/imaginary axis, at -50, to maintain the circuit natural frequency. The overall Root locus shape with the PI controller is similar to the Root locus of the proportional only controller shown in Figure 4.6. However, reference tracking and disturbance rejection have been improved since the closed-loop system is type 1 with respect to error. Root locus gain values are determined based on the system damping, which is directly related to the Quality factor, and transient response.

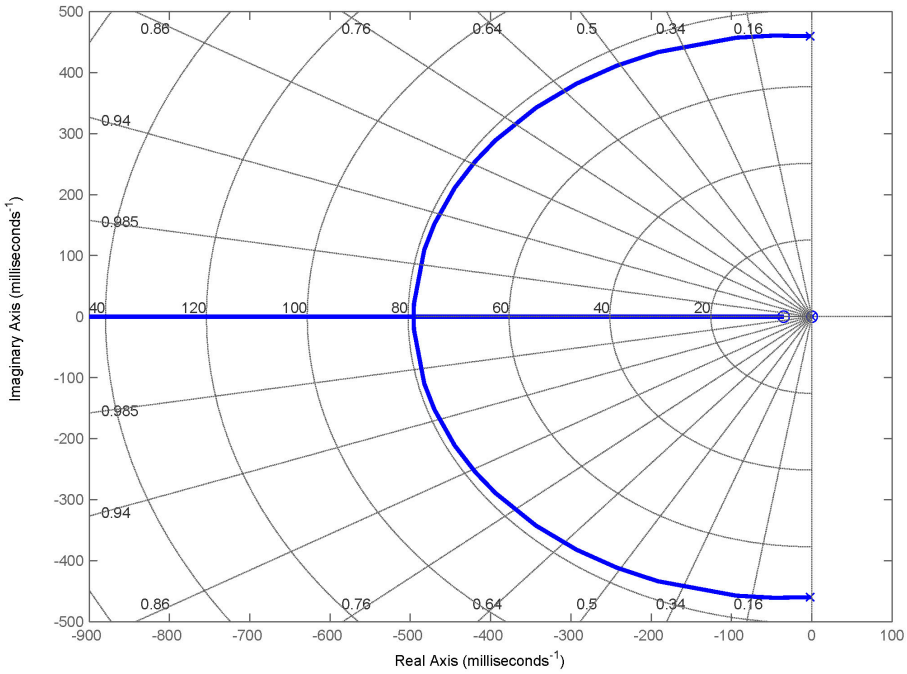

Figure 4.8: Root Locus of PI Controller and Magnetic Field Generating Circuit

The unit step and frequency response is examined to evaluate the performance of the PI controller. The closed-loop response with PI control for a unit step input is shown in Figure 4.9 (a), and closed-loop frequency response with PI control is shown in Figure 4.9 (b). The controller provides appropriate peak response and quickly arrives at steady state in response to the unit step input compared to the open-loop system. The frequency response displays a resonant peak with a narrow passband at 73 kHz. The system frequency and unit step response gives an approximation to how the system will respond to other reference input signals.

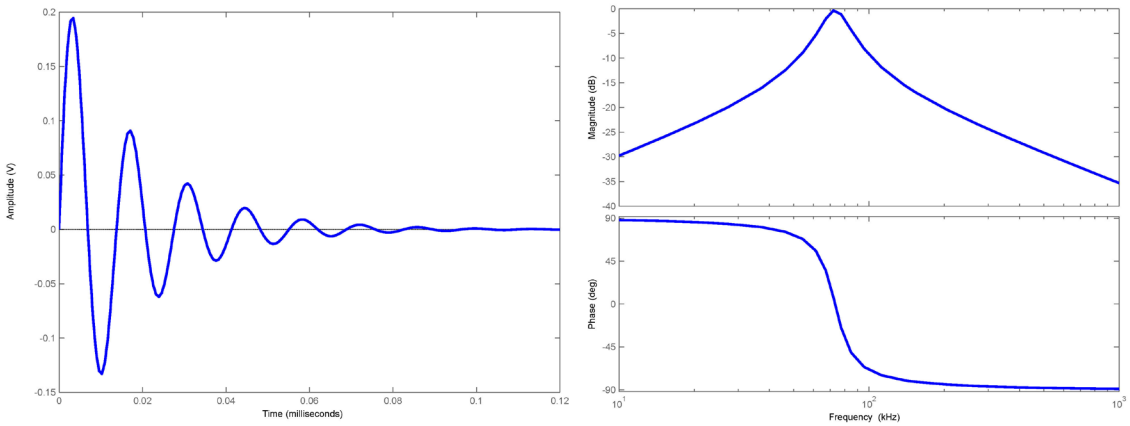

(a) **(b)**

Figure 4.9: Unit Step (a) and Frequency Response (b) of Closed-Loop System with PI Controller

4.3: Control System Simulation

This section explores the simulation and application of the feedback controller with a sinusoidal reference input. As demonstrated in Section 3.5, proximity detection systems rely on synchronized pulsed sinusoidal input signals to generate magnetic fields. The feedback system with a proportional and a PI controller is simulated using a 73 kHz pulsed sine wave similar to the one that is measured experimentally.

The proportional gain controller provides an output signal that is the difference between the set point and the process variable. To provide easy comparison and analysis, the amplitude for the simulated input sine wave is set to one. The closed-loop system response to a sinusoidal burst input using proportional gain is shown in Figure 4.10. The input signal set point is represented by the green-dashed line. The output is shown in blue, and the error signal is displayed in red.

Using a proportional gain controller, the magnetic field generating circuit response is greatly improved. The output tracks the reference input amplitude, and the transient response is improved. However, there is still significant system error. If more proportional

gain is used to compensate for the steady state error overshoot becomes a complication. The system error is reduced by incorporating an integral term to the control.

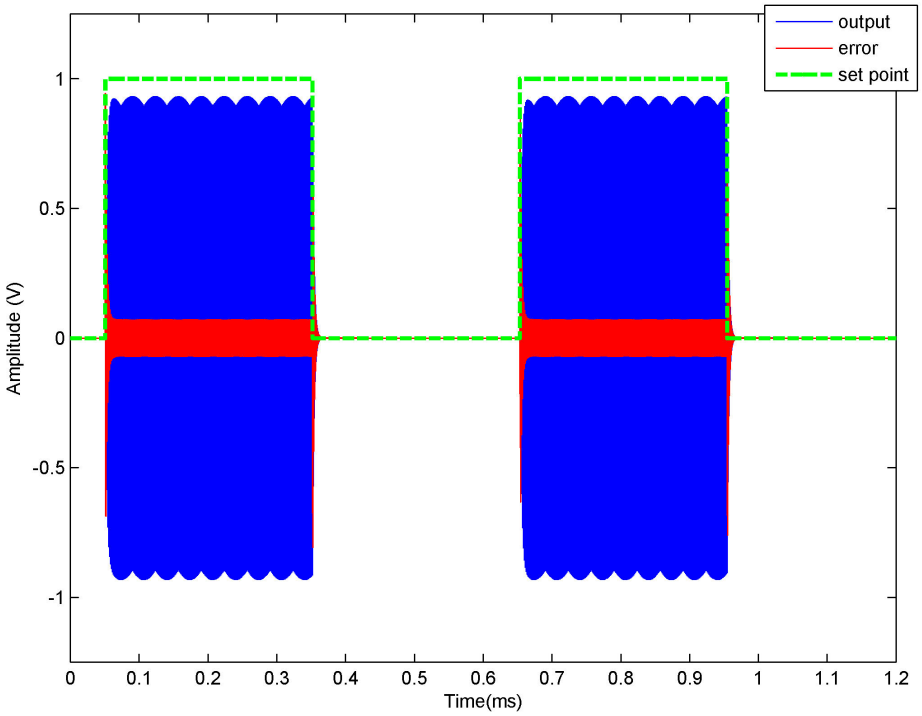

Figure 4.10: Closed-Loop Proportional Controller Response to the Sinusoidal Burst Input

The advantages of integral control, with reduced steady state error, and proportional control, with increased speed of the transient response, is combined in the PI controller. The system response to a sinusoidal burst input using PI control is shown in Figure 4.11. Again, the set point is represented the green-dashed line, the system output is shown in blue, and the error signal is displayed in red.

The addition of the integral control has further improved the response of the magnetic field generating circuit. The error, when comparing proportional control in Figure 4.10 to PI control Figure 4.11, has been reduced. Further increasing PI gain also increases system damping and shifts the circuit natural frequency away from 73 kHz. It will also introduce noise into the system since the quality factor is reduced with increased damping. These influences will become factors when experimentally implementing the controller.

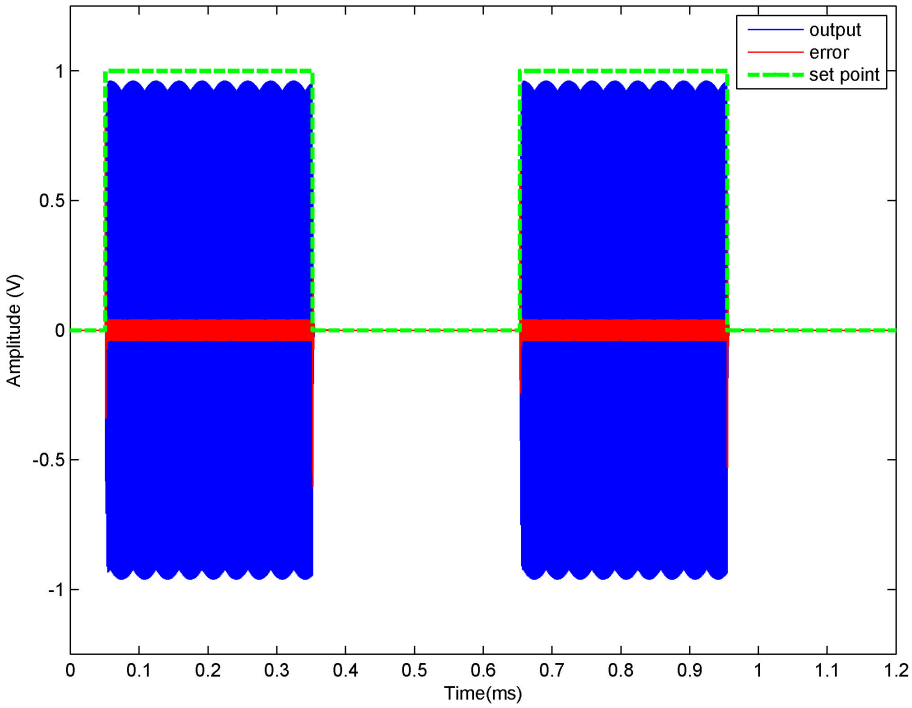

Figure 4.11: Closed-Loop PI Controller Response to the Sinusoidal Burst Input

Chapter 5: Experimental Demonstration of Feedback Control

This chapter will explore the experimental demonstration of a feedback controller that improves the consistency of the magnetic fields used in proximity detection systems. An overview is given of the experimental system implementation. System limitation and implications are discussed. The feedback control system is demonstrated with both proportional and PI controllers. Performance is compared and contrasted to the uncompensated system. Finally, the controller performance is examined in relation to temperature fluctuations. The control system improves the transient magnetic field signal response and reduces the influence of disturbances.

5.1: Experimental Feedback System Implementation

To establish the feedback path, several system connections are made. The system layout is shown in Figure 5.1 to illustrate the feedback connection. The electric current across the ferrite-core antenna of the magnetic field generating circuit is the feedback system output. This signal is measured by the CT and coupled to the PXI controller analog input/output board. The other system connections are similar to the open-loop configuration shown in Figure 3.3. These signals are connected to the host computer for data analysis and post processing.

In order to implement the feedback system, Field Programmable Gate Arrays (FPGA) are used in the controller hardware. Application-specific integrated circuits and processor-based systems components are combined in FPGA reprogrammable silicon chips [94, 95]. Different processing operations do not have to compete for the same resources since FPGA have a parallel processing structure. However, for control system applications, processing speed is still limited by the A/D measurement signal sampling and D/A con-

version of the control signal. The same function can be implemented in an FPGA and executed in hardware rather than executing the function in software. This gives the experimental system the ability to both acquire and produce signals with the same hardware.

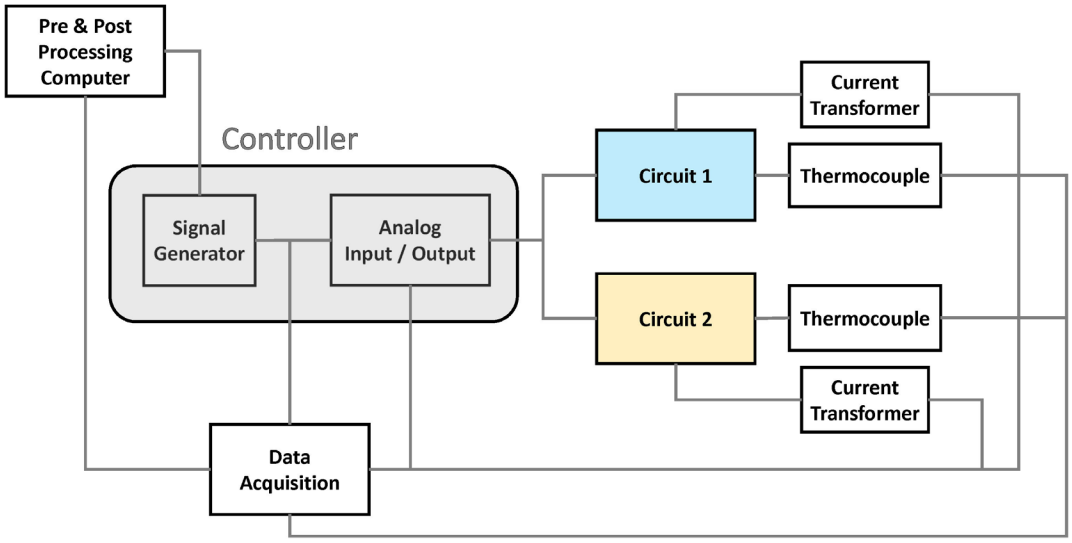

Figure 5.1: Schematic of Experimental Feedback System

Although the experimental system has enhanced capabilities to process the control algorithm, other considerations must be taken into account. The control system hardware should, in general, be capable of acquiring and producing data at least 10 times the circuit resonant frequency. The controller processor has a 2.7 GHz processor with a maximum bandwidth of 8 GB/s. However, the system is limited by the sampling rate of the analog input/output board at 1 MS/s. Significant delay between the feedback and control signal will cause the system to be unstable. Rather than use the unfiltered AC signal from CT, an RMS signal resolves some of the signal sampling concerns and can be implemented digitally.

The experimental feedback controller is realized using LabVIEW programming with FPGA capabilities. The host controller software program is shown in Appendix A. The feedback controller hardware calls for a minimum number of CPU clock ticks to acquire,

process, and produce the signal data. Data are passed through loops for each function using First-In-First-Out (FIFO) data collection and assignment functions in LavVIEW. Each loop processes one point at a time. In order to maintain consistent timing for both input and output signals, separate software loops were programmed for each software function

Another computer program is developed to monitor the experimental magnetic field generating system using LabVIEW software programming language. These programs are shown in Appendix A. The host processor that acquires and produces the magnetic field signal utilizes FPGA programming to maximize computational efficiency. However, this restricts the ability to observe both the magnetic field and temperature signals. The monitoring program examines all control system inputs and outputs, and also the temperature of the ferrite-core generators.

5.2: Experimental Feedback System Results

The performance of the experimental feedback electromagnetic field generating system is evaluated on its ability to improve the circuit disturbance rejection and transient response. The open-loop system is susceptible to internal and external temperature changes, which causes electric current drift from the set point. In Addition, the open-loop system has a poor transient response with a gradual rise time and long settling time decay. This reduces the time that a stable and constant magnetic field can be generated. A controller is implemented in the feedback loop to mitigate these issues and concerns. The performance is compared and contrasted against one another, and also limitations.

Proportional control produces a signal that corresponds to the electric current tracking error. It generally reduces rise time, increases overshoot, and reduces steady-state error. The feedback system output current across the ferrite-core antenna with unity gain is

shown Figure 5.2. The controlled signal (light blue) is overlay on the open-loop uncontrolled signal (orange). Both signals were given the same initial set point of 1 V_{rms}. The poor initial and transient response is improved with the unity feedback control, but an offset error has been introduced.

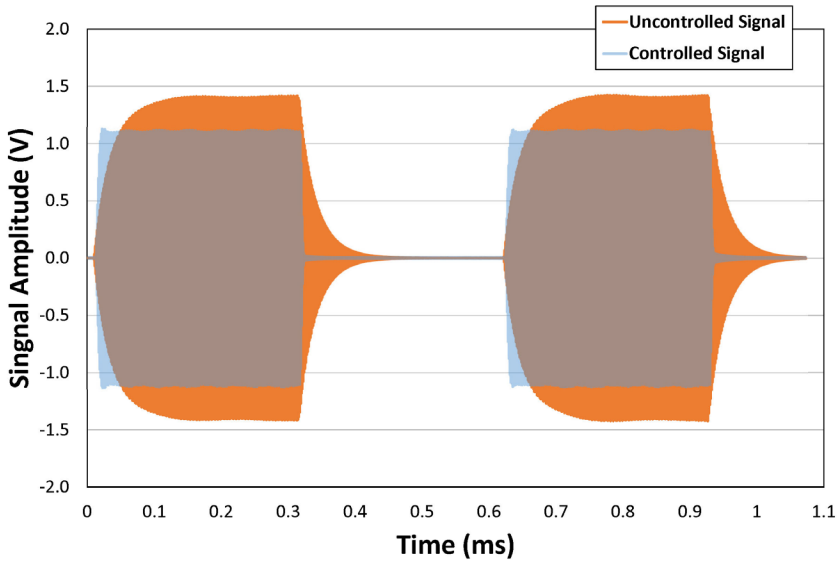

Figure 5.2: Magnetic Field Signal with Unity Gain Feedback

To reduce the offset error, the feedback proportional gain is increased. The results of increasing the proportional gain is shown in Figure 5.3. The steady state error difference between the open-loop (orange) and controlled (light blue) is reduced but not eliminated. Increasing the proportional gain also has the undesirable effect of introducing overshoot. To achieve better controller performance, an integral term is added to the feedback loop.

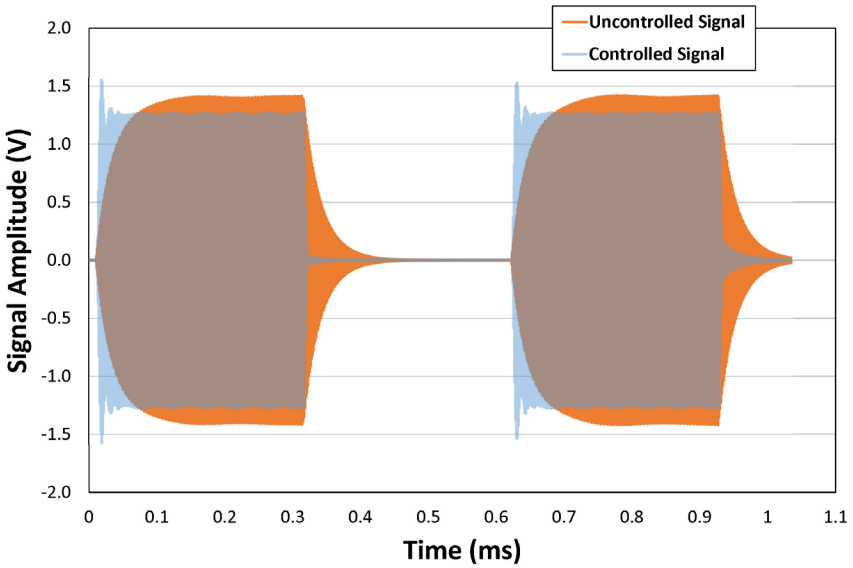

Figure 5.3: Magnetic Field Signal with Increased Proportional Gain Feedback

Integral control decreases the rise time, increases both the overshoot and the settling time, and eliminates the steady-state error. Combined with proportional gain, the PI controller provides acceptable transient response and reduces circuit steady state offset error. Figure 5.4 shows the experimental magnetic field signal with PI control applied. For this experiment, a set point of 2 V_{rms} was used to demonstrate that different values can be chosen. The circuit response of the uncompensated system (orange) is improved by the compensated (light blue) feedback system with PI control. The CT amplitude output across the ferrite-core antenna quickly reaches the set point and rapidly decays to zero, meeting all initial design requirements.

Another way to evaluate the performance of the controller is to examine the RMS signals of the feedback system. Figure 5.5 shows the PI controller RMS input signal (blue line), controller output signal (yellow line), and set point (black-dashed line). The controller tracks the reference input of 1 V_{rms} and provides an immediate response at the beginning and end of the sinusoidal burst signal.

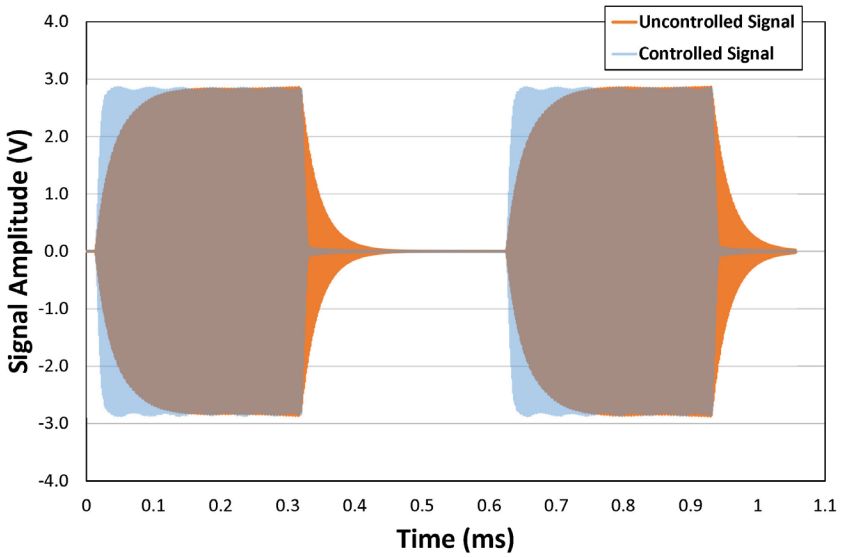

Figure 5.4: Magnetic Field Signal with PI control

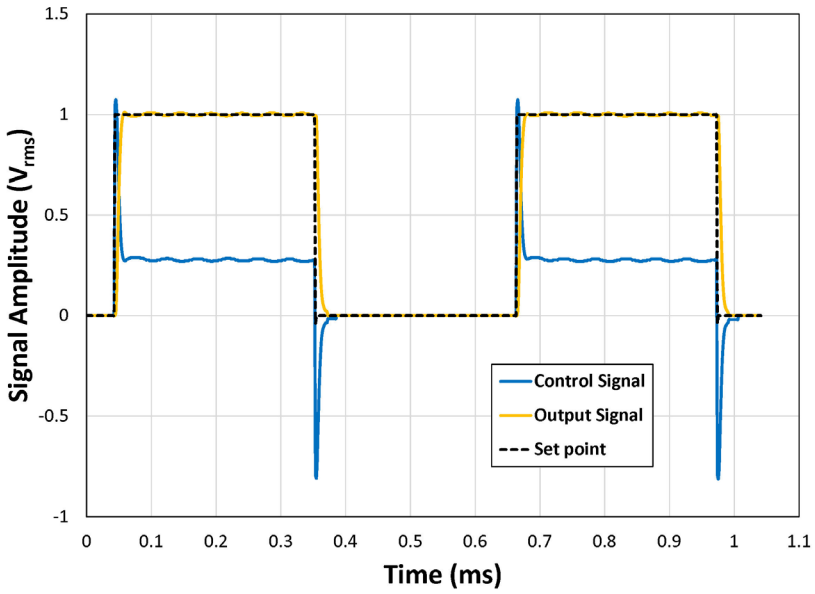

Figure 5.5: RMS Magnetic Field Signal with PI control

These results establish that PI control, when introduced into the feedback loop, can produce a more efficient and stable magnetic field signal for proximity detection systems. The magnetic field signal of the open-loop system has a relatively slow rise time and

gradual exponential decay. By introducing PI control in the feedback loop, these transient characteristics are improved so that a consistent magnetic field signal is transmitted. A consistent and stable magnetic field signal improves the accuracy and performance of electromagnetic proximity detection systems.

5.3: Experimental System Disturbance Rejection

As discussed in Chapter 3, changes in temperature can dramatically affect the performance of the magnetic field generating circuit used in electromagnetic proximity detection systems. The feedback system should eliminate electric current disturbances across the ferrite-core antennas caused by temperature fluctuations. The ability of the feedback system to reject temperature disturbance is assessed by introducing internal and external temperature changes to the ferrite-core antenna.

When electromagnetic proximity detection systems are powered on, the ferrite-core antenna surface has a first-order temperature rise to a steady state. As demonstrated in Figure 3.16, this temperature rise can cause the electric current across the ferrite-core antenna to change significantly. The feedback system eliminates the electric current fluctuations caused by startup temperature rise. Figure 5.6 shows the ferrite-core antenna electric current (orange line) and temperature (blue line) during startup for magnetic field generator 1. During the temperature rise to steady state, the feedback system maintains the electric current set-point (black-dashed line).

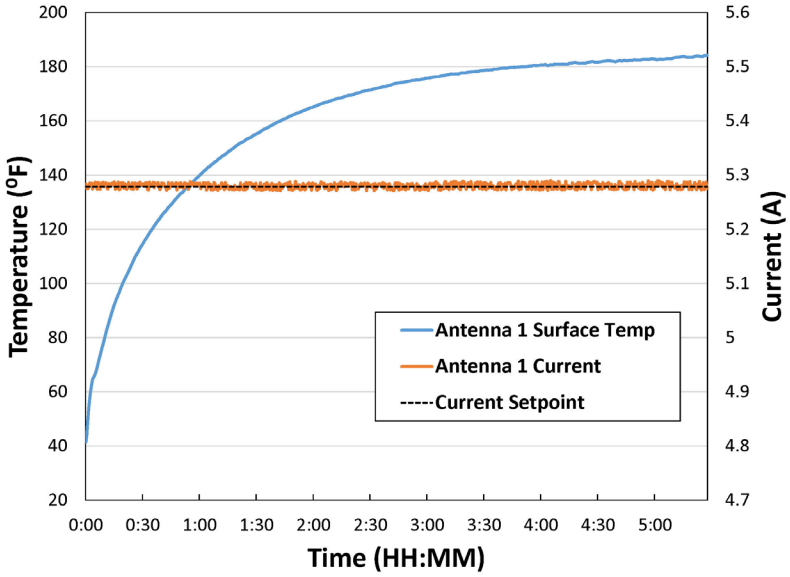

Figure 5.6: Generator 1 Surface Temperature vs Current with Feedback Control

The feedback system must also be able to eliminate external temperature influences that cause the electric current to drift from the initial set-point. To demonstrate the ability of the feedback system to reject external temperature influences, the ferrite-core antenna was heated to a high surface temperature then placed in an environmentally controlled cooler. Similar to the test shown in Figure 3.16 with the open-loop system, a 36-Quart Kool thermoelectric cooler was used to change the ambient temperature. Figure 5.7 shows the ferrite-core surface temperature (blue line) decay and resulting electric current (orange line). The feedback system maintains the electric current set-point (black-dashed line) during the temperature decay to ambient steady state.

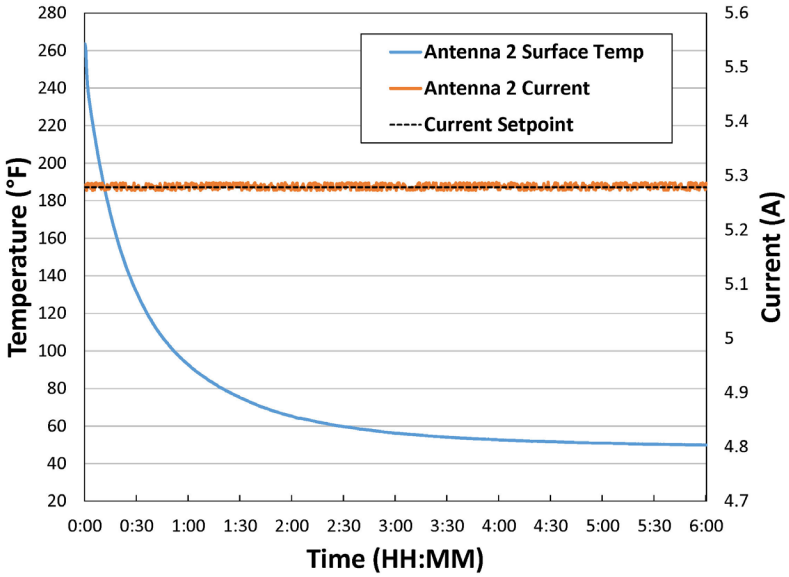

Figure 5.7: Cooling of Generator 2 to Ambient Temperature with Feedback Control

These results demonstrate that incorporating a feedback system into an electromagnetic proximity detection system can reduce the influences of internal and external temperature changes. Temperatures can fluctuate in an underground mine and cause the magnetic fields used in proximity detection systems to be inconsistent. By incorporating a feedback system into the magnetic field generating circuit, the magnetic fields stay uniform and constant despite temperature irregularities throughout an underground mine. This reduces worker position triangulation error and the occurrence of false alarms.

Chapter 6: Summary and Conclusions

6.1: Summary

Much has been done to improve the health and safety of mine workers. However, mine workers are still exposed to hazards and are considered one of the most dangerous occupations in industry. Machine related accidents and injuries continue to be a safety concern, particularly in underground coal mines. Striking and pinning hazards, due to the confined work environment and use of large machinery, continue to cause injuries and fatalities.

Several technologies are available to reduce machine related accidents and injuries within the mining industry. Remote sensing and proximity detection technologies developed for other industries have transitioned into the mining industry. However, technologies such as radar, GPS based localization, and thermal imaging are not conducive to the application of underground mining. Furthermore, there are special considerations for technology being introduced into underground coal mines due to intrinsic safety requirements.

Electromagnetic proximity detection systems have been developed to reduce striking and pinning hazards in underground coal mines. Pinning, striking, and crushing accidents involving underground mobile equipment are of particular safety concern for underground coal mine workers, resulting in an average of 6.5 deaths per year and many more injuries. As a result of these repeated fatalities and injuries, new laws and regulations have been promulgated to help introduce electromagnetic proximity detection systems into underground coal mines. These systems rely on machine-mounted magnetic field generators and worker-worn magnetic field strength sensors to provide warning and shutdown zones

around underground mobile equipment. Enhanced safety features, such as selective machine-function shutdown, is introduced through the development of a magnetic shell-based model.

An experimental system is developed to evaluate the performance of electromagnetic proximity detection systems. A two-generator system is constructed in a laboratory environment, consisting of magnetic field ferrite-core generators and impedance-matching circuits. Although a two-generator system does not have practical application in an underground working environment, it can be used to study and improve electromagnetic proximity detection system performance. The electromagnetic field model is developed through the experimental system to demonstrate position triangulation, which can be used to determine the exact position of workers around underground mining equipment.

The performance of electromagnetic based proximity detection systems can be influenced by the mining environment and internal circuit components. The experimental system is further used to examine the effect of temperature on the magnetic fields produced by the generators. Changes in temperature can influence the electric current across the magnetic field generators used in underground proximity detection systems. These influences can affect the performance of proximity systems by introducing inconsistent magnetic fields.

A control system is developed and demonstrated that reduces the internal and external temperature influences on the magnetic field generating circuit. A numerical model is established of the experimental two-generator system to develop the control system. Initially, a proportional gain feedback controller is investigated through simulation. Integral gain is added to the controller to improve system response and reduce offset error. The controller is implemented into the experimental system. Several scenarios are examined to demonstrate that the effects of temperature are minimized by introducing proportion-integral feedback control.

6.2: Conclusions

The main conclusions of this work are based on the following research results:

- An overview of health and safety surveillance and statistics reveal that machine related injuries and fatalities are a significant concern for the mining industry, despite focused laws and regulations. Striking, pinning, and entanglement hazards are of particular concern for the underground coal mines, where large machinery is used in confined work spaces. Enhanced safety technologies to mitigate these hazards are limited by the intrinsic safety requirements of the environment.

- Electromagnetic proximity detection systems have been implemented in underground coal mines to reduce striking, pinning, and entanglement hazards. While these systems meet the requirements of an underground coal mine, performance is affected by environmental influences. Internal and external temperature changes can have a significant impact on electromagnetic proximity detection accuracy.

- Electromagnetic proximity detection system performance can be improved by implementing feedback control. Proportional control improves the magnetic field signal transient response, but does not improve steady state error. The addition of an integral term to the feedback controller eliminates this error.

6.3: Contributions

The overall impact of this work provides a greater understanding of the performance related to electromagnetic based proximity detection systems. Contributions include:

- The development of the governing equations that describe electromagnetic field generation and detection used in proximity detection systems

- Conception and fabrication of an experimental system that can be used to study electromagnetic proximity detection performance

- Demonstration and quantification of internal and external temperature influences on the performance of electromagnetic proximity detection systems

- A numeric model that can be used to simulate the magnetic field signal used in proximity detection systems

- Design of a simple feedback controller for proximity detection systems can significantly improve performance

- Application of an experimental feedback controller that can eliminate the influence of temperature on proximity detection systems

6.4: Future Work

Subsequent research investigations into electromagnetic proximity detection systems should focus on further improving performance. While this work shows that application of a simple feedback controller can dramatically reduce the influence of temperature, there are other factors that can influence proximity detection systems. The presence of metal in the magnetic field can also influence proximity detection system accuracy. Parameter estimation and classification can be used to detect and correct when metal is introduced into the magnetic field. These methods could be incorporated into the control system. Also, other technologies could be combined with electromagnetics to enhance

performance. Information from alternate sensors would need to be appropriately integrated into the control system.

References

1. Mine Safety and Health Administration (MSHA). *Coal Fatalities for 1900 Through 2014*. 2015 [cited 2015 December]; Available from: http://www.msha.gov/stats/centurystats/coalstats.asp.

2. Bureau of Labor Statistics (BLS). *Injuries, Illnesses, and Fatalities in the Coal Mining Industry*. 2010 [cited 2015 December]; Available from: http://www.bls.gov/iif/oshwc/osh/os/osar0012.htm.

3. National Institute for Occupational Safety and Health (NIOSH). *Worker Health eChartbook*. 2003-2007 [cited 2015 December]; Available from: http://wwwn.cdc.gov/niosh-survapps/echartbook/Chart.aspx?id=7039&cat=74.

4. Humphrey, H.B., *Historical Summary of Coal-mine Explosions in the United States, 1810 [ie 1910]-1958*. 1960: US Government Printing Office.

5. Richmond, J.K., et al., *Historical summary of coal mine explosions in the United States, 1959-81*. 1983: US Department of the Interior, Bureau of Mines.

6. Breslin, J.A., *One hundred years of federal mining safety and health research*. 2010: Department of Health and Human Services, Centers for Disease Control and Prevention, National Institute for Occupational Safety and Health, Pittsburgh Research Laboratory.

7. Murphy, J.N., *Coal mine health and safety research in the USA - the achievements of the US bureau of mines.* Coal international Redhill, 1994. **242**(6): p. 219-226.

8. Schnakenberg, G.H., *US Bureau of Mines coal mining automation research Preprint - Society of Mining Engineers of AIME*. 1990. 12p87-12p87.

9. Grayson, R.L., *Safety vs. productivity and other factors in US underground coal mines.* Mining Engineering, 2001. **53**(8): p. 41-44.

10. Tien, J., *The impacts of MINER Act of 2006 on the U.S. mining industry.* Journal of Coal Science & Engineering(China), 2008. **14**(3): p. 501-506.

11. Anonymous, *MINER Act Ensures First Mine Safety Reform in 28 Years.* Professional Safety, 2006. **51**(8): p. 12.

12. Novak, T., D.P. Snyder, and J.L. Kohler, *Postaccident mine communications and tracking systems.* Industry Applications, IEEE Transactions on, 2010. **46**(2): p. 712-719.

13. Nieto, A. and A. Duerksen, *The effects of mine safety legislation on mining technology in the USA.* International Journal of Mining and Mineral Engineering, 2008. **1**(1): p. 95-103.

14. Kohler, J.L., *Looking ahead to significant improvements in mining safety and health through innovative research and effective diffusion into the industry.* International Journal of Mining Science and Technology, 2015. **25**(3): p. 325-332.

15. Foundation, M.-L.M.R.R. *Historic Mid-Lothian Mines Park*. 2015 [cited 2015 December 20th]; Available from: http://www.midlomines.org/History_EXZH.html.

16. EIA, U., *Annual energy outlook 2015: With Projections to 2040*. 2015.

17. Harris, L., *Annual coal report, 2013.* Washington: Energy Information Administration, Department of Energy (US), 2015.

18. Administration, E.I. *U.S. Coal Reserves*. 2015 [cited 2015 December 20th]; Available from: http://www.eia.gov/coal/reserves/.

19. National Institute for Occupational Safety and Health (NIOSH). *Coal Industry Sector*. 2013 [cited 2015 Dec. 20th]; Available from: http://www.cdc.gov/niosh/mining/statistics/CoalSector.html.

20. Coulson, M., *The History of Mining: The events, technology and people involved in the industry that forged the modern world*. 2012: Harriman House Limited.

21. Graebner, W. and O.A. Historians, *Coal-mining Safety in the Progressive Period: The Political Economy of Reform*. 1976: Organization of American Historians.

22. Hayes, G., *Coal mining*. 2000.

23. Hagley Museum and Library. *Joy Manufacturing Company Records*. 2009 [cited 2015 December 15th]; Available from: http://findingaids.hagley.org/xtf/view?docId=ead/2463.xml.

24. Bise, C., *Modern American Coal Mining*. 2013.

25. Kennedy, B.A., M. Society for Mining, and Exploration, *Surface Mining, Second Edition*. 1990: Society for Mining, Metallurgy, and Exploration.

26. Darling, P., M. Society for Mining, and Exploration, *SME Mining Engineering Handbook, Third Edition*. 2011: Society for Mining, Metallurgy, and Exploration.

27. United Mine Workers of America. *Room and Pillar Mining*. [cited 2015 December 15th]; Available from: http://www.umwa.org/index.php?q=content/room-and-pillar-mining.

28. Burgess-Limerick, R., *Injuries Associated with Underground Coal Mining Equipment in Australia.* Ergonomics Open Journal, 2011. **4**: p. 62-73.

29. Donoghue, A.M., *Occupational health hazards in mining: an overview.* Occupational Medicine, 2004. **54**(5): p. 283-289.

30. Ruff, T., P. Coleman, and L. Martini, *Machine-related injuries in the US mining industry and priorities for safety research.* International Journal of Injury Control and Safety Promotion, 2011. **18**(1): p. 11-20.

31. Camm, T. and J. Girard-Dwyer, *Economic consequences of mining injuries.* Mining Engineering, 2005. **57**(9): p. 89-92.

32. (NIOSH), N.I.f.O.S.a.H. *Statistics: All Mining*. 2106 [cited 2016; Available from: https://www.cdc.gov/niosh/mining/statistics/allmining.html.

33. Groves, W.A., V.J. Kecojevic, and D. Komljenovic, *Analysis of fatalities and injuries involving mining equipment.* Journal of Safety Research, 2007. **38**(4): p. 461-470.

34. Stojadinović, S., et al., *Mining injuries in Serbian underground coal mines–a 10-year study.* Injury, 2012. **43**(12): p. 2001-2005.

35. Chen, H., et al., *Research on 10-year tendency of China coal mine accidents and the characteristics of human factors.* Safety science, 2012. **50**(4): p. 745-750.

36. Sari, M., et al., *Accident analysis of two Turkish underground coal mines.* Safety Science, 2004. **42**(8): p. 675-690.

37. Mine Safety and Health Administration. *Final Rule on Proximity Detection Systems for Continuous Mining Machines in Underground Coal Mines*. 2015 [cited 2015 December 20th]; Available from: http://www.msha.gov/regs/fedreg/final/2015/proximity-detection/.

38. Mine Safety and Health Administration. *Proposed Rule for Proximity Detection Systems for Mobile Machines in Underground Coal Mines to Prevent Deaths and Injuries*. 2015 [cited 2015 December 20th]; Available from: http://www.msha.gov/REGS/FEDREG/PROPOSED/2015/proximity-detection-mobile/index.asp.

39. *Mine Health and Safety Act (29/1996) - Regulations relating to machinery and equipment*, M. Resources, Editor. 2015, The Government Gazette of South Africa: South Africa

40. Huntley, C., *Remote Controlled Continuous Mining Machine Fatal Accident Analysis Report of Victim's Physical Location with Respect to the Machine*, D.o. Labor, Editor. 2002, Mine Safety and Health Administration. p. 11.

41. Hattori, Y., E. Ono, and S. Hosoe, *Optimum vehicle trajectory control for obstacle avoidance problem.* Mechatronics, IEEE/ASME Transactions on, 2006. **11**(5): p. 507-512.

42. Shibata, N., S. Sugiyama, and T. Wada. *Collision avoidance control with steering using velocity potential field*. in *Intelligent Vehicles Symposium Proceedings, 2014 IEEE*. 2014. IEEE.

43. Vahidi, A. and A. Eskandarian, *Research advances in intelligent collision avoidance and adaptive cruise control.* Intelligent Transportation Systems, IEEE Transactions on, 2003. **4**(3): p. 143-153.

44. Lee, K. and H. Peng, *Evaluation of automotive forward collision warning and collision avoidance algorithms.* Vehicle System Dynamics, 2005. **43**(10): p. 735-751.

45. Sun, Z., G. Bebis, and R. Miller, *On-road vehicle detection: A review.* IEEE Transactions on Pattern Analysis and Machine Intelligence, 2006. **28**(5): p. 694-711.

46. Mukhtar, A., L. Xia, and T.B. Tang, *Vehicle Detection Techniques for Collision Avoidance Systems: A Review.* IEEE Transactions on Intelligent Transportation Systems, 2015. **16**(5): p. 2318-2338.

47. *Federal Motor Vehicle Safety Standards: Vehicle-to-Vehicle (V2V) Communications*, N.H.T.S.A. (NHTSA), Editor. 2017: 49 CFR Part 571.

48. Ahmed-Zaid, F., Bai, F., Bai, S., Basnayake, C., Bellur, B., Brovold, S.,, et al., *Vehicle Safety Communications -Application (VSC-A) Final Report*, N.H.T.S. Administration, Editor. 2011.

49. Bellamy, D. and L. Pravica, *Assessing the impact of driverless haul trucks in Australian surface mining.* Resources Policy, 2011. **36**(2): p. 149-158.

50. Magnusson, M., A. Lilienthal, and T. Duckett, *Scan registration for autonomous mining vehicles using 3D-NDT.* Journal of Field Robotics, 2007. **24**(10): p. 803-827.

51. McNab, K. and M. Garcia-Vasquez, *Autonomous and remote operation technologies in Australian mining.* Prepared for CSIRO Minerals Down Under Flagship, Minerals Futures Cluster Collaboration, by the Centre for Social Responsibility in Mining, Sustainable Minerals Institute, The University of Queensland. Brisbane, 2011.

52. Organisation, I.S., *Earth-moving machinery and mining - Autonomous and semi-autonomous machine system safety*, in *ISO/IS 17757*. 2016.

53. Ralston, J., et al., *Longwall automation: Delivering enabling technology to achieve safer and more productive underground mining.* Lnternational Journal of Mining Science and Technology, 2015. **25**(6): p. 865-876.

54. Roberts, J.M., E.S. Duff, and P.I. Corke, *Reactive navigation and opportunistic localization for autonomous underground mining vehicles.* Information Sciences, 2002. **145**(1): p. 127-146.

55. Horberry, T. and D. Lynas, *Human interaction with automated mining equipment: The development of an emerging technologies database.* Ergon. Aust, 2012. **8**: p. 1-6.

56. Ruff, T. and T. Holden, *Preventing collisions involving surface mining equipment: a GPS-based approach.* Journal of safety research, 2003. **34**(2): p. 175-181.

57. Sabniveesu, V., et al., *Use of wireless, ad-hoc networks for proximity warning and collision avoidance in surface mines.* International Journal of Mining, Reclamation and Environment, 2015. **29**(5): p. 331-346.

58. Borthwick, J.R., P.D. Lawrence, and R.H. Hall. *Mining haul truck localization using stereo vision*. in *Proceedings of the IASTED International Conference on Robotics and Applications*. 2009.

59. Kandil, A., M. Hastak, and P.S. Dunston, *Proximity Sensing and Warning Technology for Heavy Construction Equipment Operation.* Bridges, 2014. **10**: p. 9780784412329.099.

60. Ruff, T., *Evaluation of a radar-based proximity warning system for off-highway dump trucks.* Accident analysis and prevention, 2006. **38**(1): p. 92-98.

61. Teizer, J., M. Venugopal, and A. Walia, *Ultrawideband for automated real-time three-dimensional location sensing for workforce, equipment, and material positioning and tracking.* Transportation Research Record: Journal of the Transportation Research Board, 2008. **2081**(1): p. 56-64.

62. Jiang, X., et al. *Design and evaluation of a wireless magnetic-based proximity detection platform for indoor applications*. in *Proceedings of the 11th international conference on Information Processing in Sensor Networks*. 2012. ACM.

63. Rizos, C., et al., *Indoor positioning techniques based on Wireless LAN.* 2007.

64. Nerguizian, C., C. Despins, and S. Affès, *Geolocation in mines with an impulse response fingerprinting technique and neural networks.* IEEE Transactions on Wireless Communications, 2006. **5**(3): p. 603-611.

65. Gerald Homce, J.W., Michael Yenchek, and R.J. Matetic. *A Comparison of U.S. Mining Industry Criteria for Intrinsically Safe Apparatus to Similar IEC-Based Standards*. 2017 [cited 2017 July 1st]; Available from: https://www.cdc.gov/niosh/mining/content/comparisonofminingcriteria.html.

66. Marks, E. and J. Teizer. *Evaluation of the Position and Orientation of (Semi-) Passive RFID Tags for the Potential Application in Ground Worker Proximity Detection and Alert Devices in Safer Construction Equipment Operation"*. in *2013 ASCE International Workshop on Computing in Civil Engineering, Los Angeles, California*. 2013.

67. Dickens, J., M. Van Wyk, and J. Green. *Pedestrian detection for underground mine vehicles using thermal images*. in *AFRICON, 2011*. 2011. IEEE.

68. Chi, S. and C.H. Caldas, *Image-based safety assessment: automated spatial safety risk identification of earthmoving and surface mining activities.* Journal of Construction Engineering and Management, 2011. **138**(3): p. 341-351.

69. Carr, J.L., Li, J., & Smith, A. K.,, *Use of Magnetic Proximity Detection Systems in The Presence Of Coal*, in *SME Annual Meeting and Exhibit*. 2013: Denver, CO.

70. Administration, M.S.a.H. *Proximity Detection Systems approved for use in underground coal mines*. 2016 [cited 2016 Jan. 20th]; Available from: https://arlweb.msha.gov/regs/fedreg/final/2015/proximity-detection/approved-systems.asp.

71. Schiffbauer, W.H., *Active proximity warning system for surface and underground mining applications.* Mining engineering, 2002. **54**(12): p. 40-48.

72. Bartels, J.R., D.H. Ambrose, and S. Gallagher, *Analyzing factors influencing struck-by accidents of a moving mining machine by using motion capture and*

DHM simulations. SAE international journal of passenger cars-electronic and electrical systems, 2008. **1**(2008-01-1911): p. 599-604.

73. Li, J., J. Carr, and C. Jobes, *A shell-based magnetic field model for magnetic proximity detection systems.* Safety science, 2012. **50**(3): p. 463-471.

74. Carr, J.L., C.C. Jobes, and J. Li. *Development of a method to determine operator location using electromagnetic proximity detection*. in *Robotic and Sensors Environments (ROSE), 2010 IEEE International Workshop on*. 2010. IEEE.

75. Bissert, P.T., J.L. Carr, and J.P. DuCarme, *Proximity Detection Zones: Designs to Prevent Fatalities Around Continuous Mining Machines.*

76. Jobes, C., J. Carr, and J. DuCarme, *Evaluation of an Advanced Proximity Detection System for Continuous Mining Machines.* International Journal of Applied Engineering Research, 2012. **7**(6).

77. Haas E.J., R.K.A., *Integrating technology: learning from mine worker perceptions of proximity detection systems*, in *SME Annual Meeting*. 2015, Society for Mining, Metallurgy, and Exploration, Inc: Denver, CO. p. 7.

78. Ducarme, J., Carr, J., Reyes, M., *Smart Sensing: The Next Generation.*, in *Mining Magazine* 2013. p. 58-56.

79. Carr, J.L.J., C.C.; Lutz, T.J.; Yonkey, J.A.,, *Field tests of second generation proximity detection systems on continuous miners* Mining Engineering, 2015. **67**(3): p. 20.

80. Kraus, J.D., *Antennas*. 1988: McGraw-Hill.

81. Stutzman, W.L. and G.A. Thiele, *Antenna Theory and Design, 3rd Edition*. 2012: Wiley.

82. Jackson, J.D., *Classical Electrodynamics*. 1998: Wiley.

83. Li, J., C. Jobes, and J. Carr. *Comparison of magnetic field distribution models for a magnetic proximity detection system*. in *Industry Applications Society Annual Meeting (IAS), 2011 IEEE*. 2011.

84. Griffiths, D.J., *Introduction to Electrodynamics*. 2014: Pearson Education.

85. Fallah, N., et al., *Indoor human navigation systems: A survey.* Interacting with Computers, 2013: p. iws010.

86. Gholami, M.R., *Positioning algorithms for wireless sensor networks.* 2011.

87. Roxin, A.-M., et al. *Survey of wireless geolocation techniques*. in *IEEE globecom workshops*. 2007.

88. Kaemarungsi, K. *Distribution of WLAN received signal strength indication for indoor location determination*. in *Wireless Pervasive Computing, 2006 1st International Symposium on*. 2006. IEEE.

89. Waqar, W., Y. Chen, and A. Vardy. *Exploiting smartphone sensors for indoor positioning: A survey*. in *Proceedings of the Newfoundland Conference on Electrical and Computer Engineering*. 2011.

90. Sunderman, C. and J. Waynert. *An overview of underground coal miner electronic tracking system technologies*. in *Industry Applications Society Annual Meeting (IAS), 2012 IEEE*. 2012. IEEE.

91. Jobes, C.C., et al., *Analysis, Conversion, and Visualization of Survey Postion and Magnetic Flux Density Data for a Proximity Detection System*, in *SME Annual Meeting*. 2016: Phoenix, AZ. p. 5.

92. Li, J., et al., *Environmental impact on the magnetic field distribution of a magnetic proximity detection system in an underground coal mine.* Journal of Electromagnetic Waves and Applications, 2013. **27**(18): p. 2416-2429.

93. Yantek, D.S., et al., *Effects of mine strata thermal behavior and mine initial temperatures on mobile refuge alternative temperature.* Mining Engineering, 2017. **69**(4): p. 41-48.

94. Carter, W.S., et al. *USER PROGRAMMABLE RECONFIGURABLE LOGIC ARRAY*. in *Proceedings of the Custom Integrated Circuits Conference*. 1986.

95. Hsieh, H.-C., et al. *SECOND GENERATION USER-PROGRAMMABLE GATE ARRAY*. in *Proceedings of the Custom Integrated Circuits Conference*. 1987.

Appendix A

LabVIEW Code

The following program and code was developed to produce the open-loop magnetic field and implement the closed-loop feedback controller.

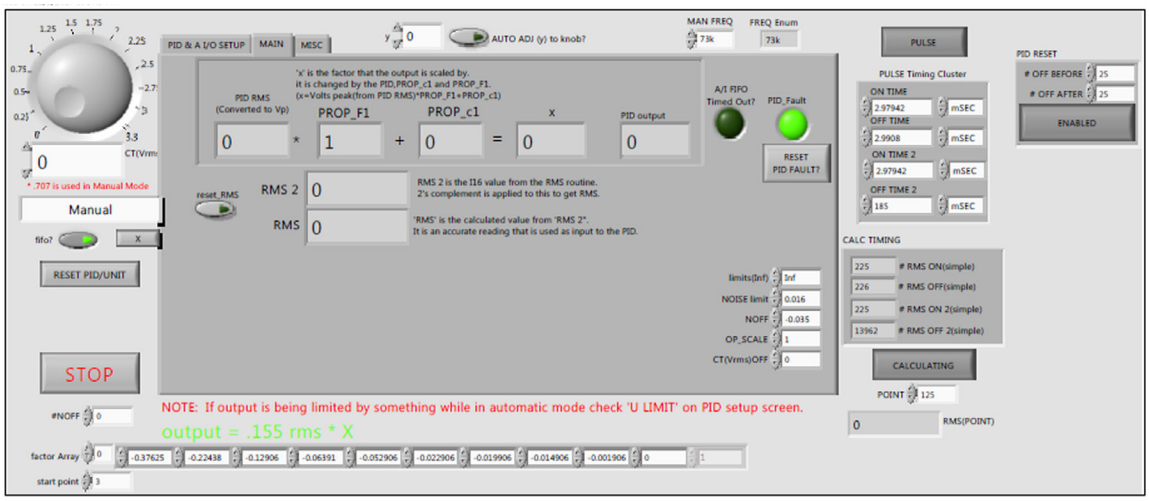

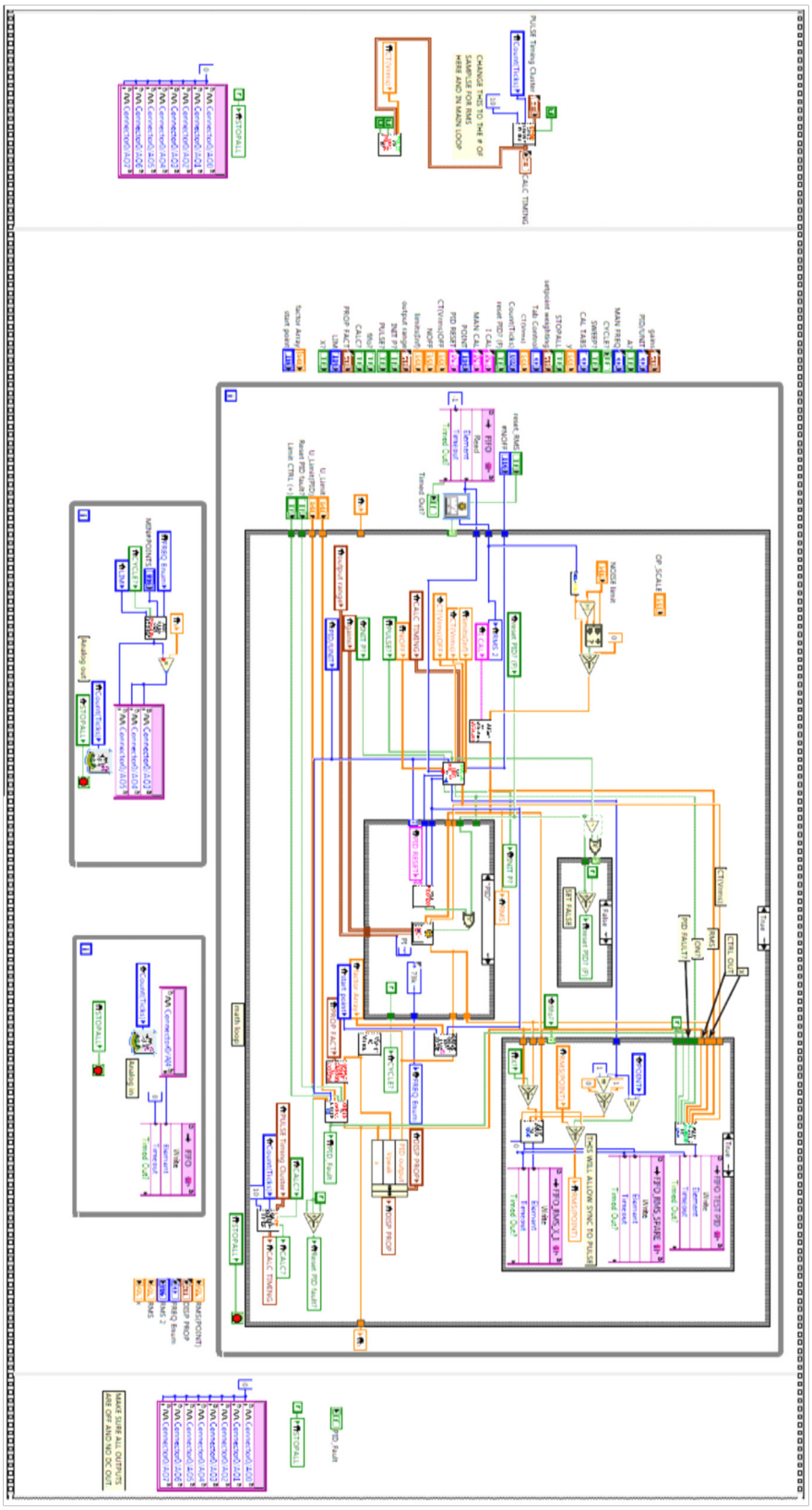

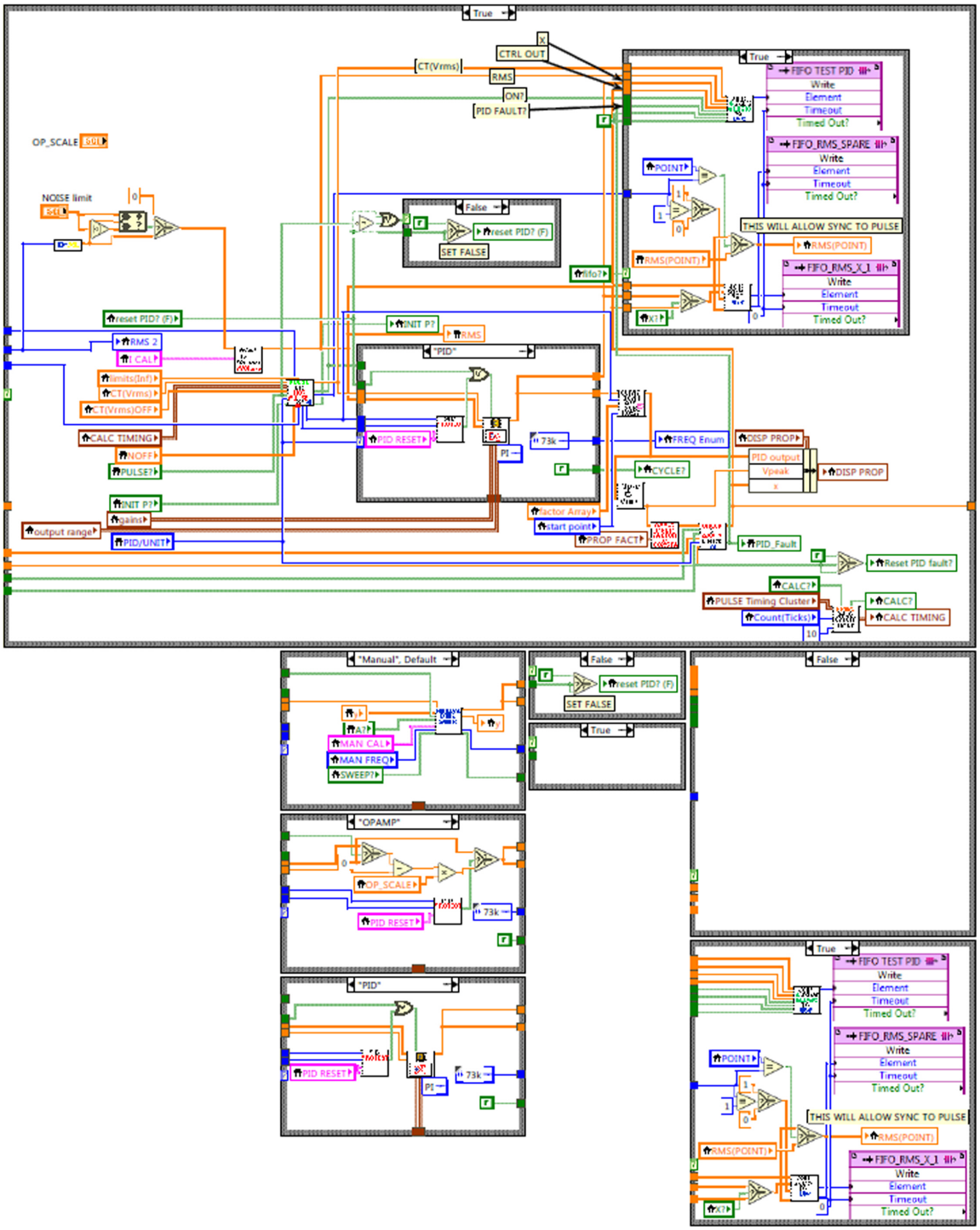

The following program and code was developed to monitor the magnetic field generator circuit.

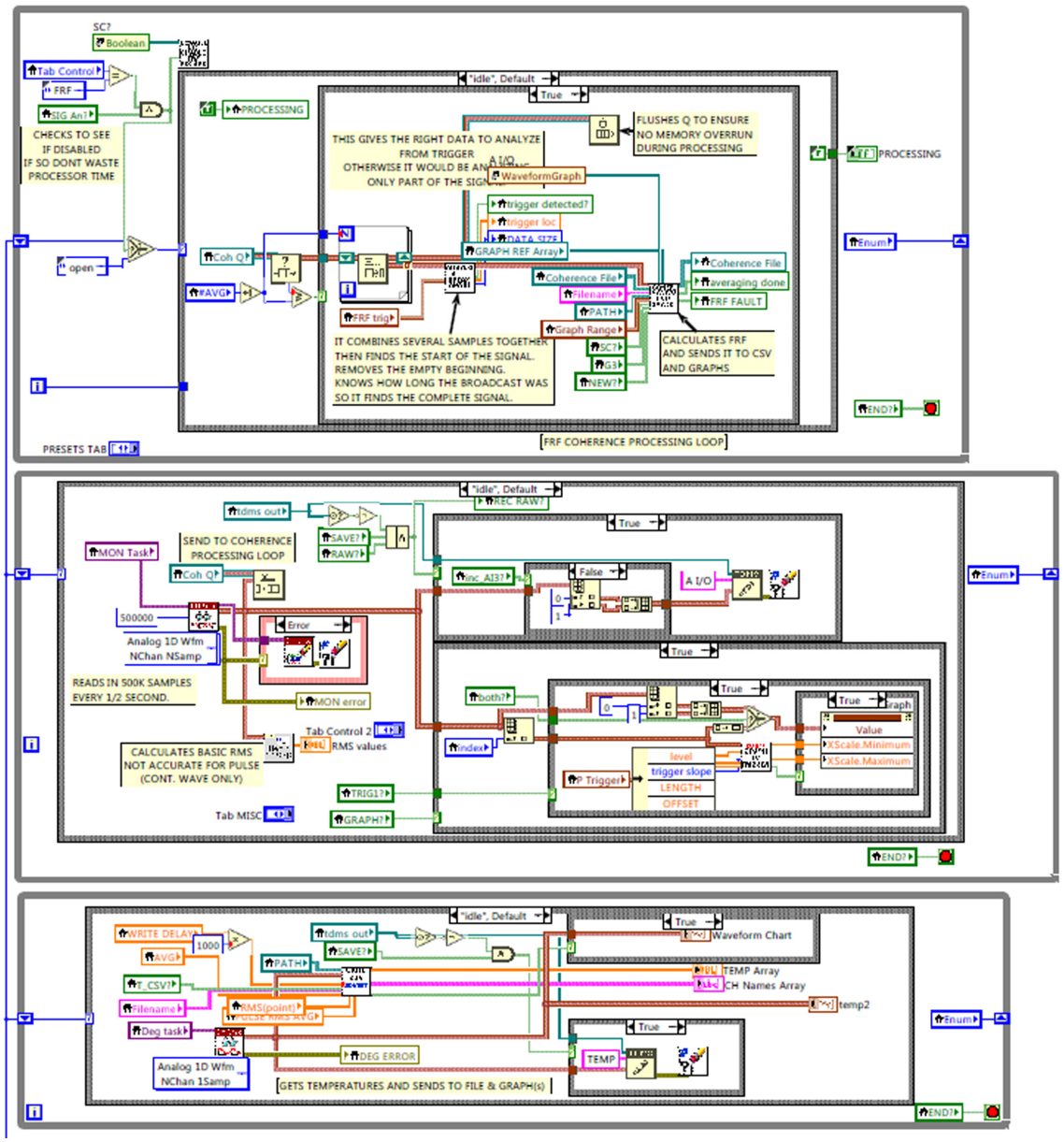

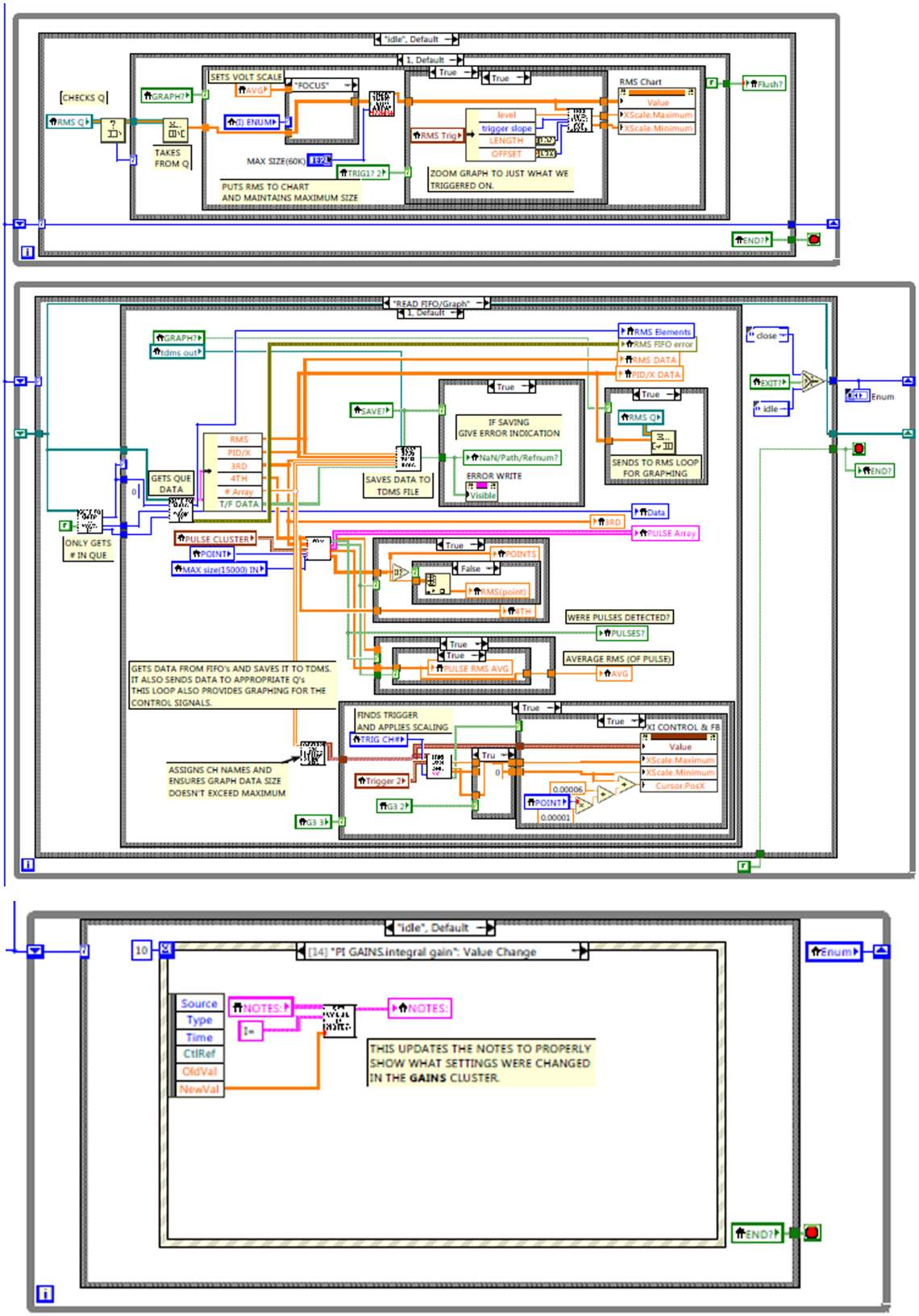

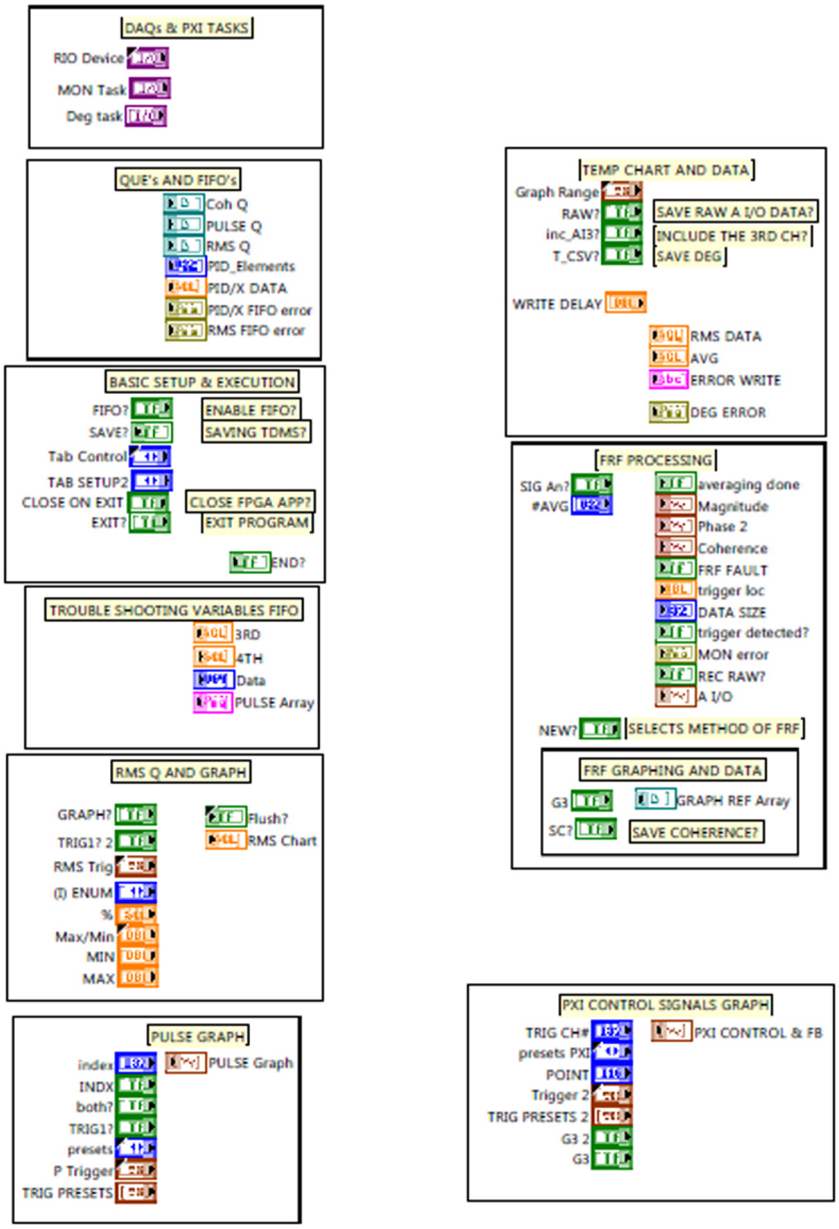

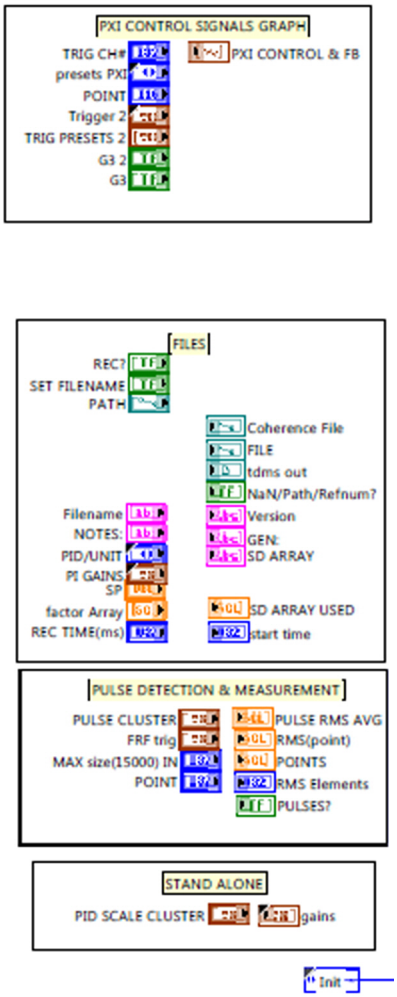

Appendix B

Matlab Code

The following code was developed to model the magnetic field generating circuit and simulate feedback controller performance.

```
clear all
close all

%% Model the Amplifier circuit

% Amplifier - Mult. by 10 for probe and sensor induced gains
K1 = 52.6*10;
K2 = 51.6*10;

% K1 = 1;
% K2 = K1;


% Transformer
R_t1 = 0.2179;
R_t2 = 0.2179;
L_t1 = 1.8177e-6;
L_t2 = 1.8177e-6;
N = 6;

% Antenna
R_g1 = 0.639592;
```

```
R_g2 = 0.758925;
C1 = 2.78204e-8;
C2 = 2.79155e-8;
L_g1 = 170.11e-6;
L_g2 = 168.9e-6;

Plant1 = tf([K1 0],[(L_t1+N^2*L_g1) (R_t1+N^2*R_g1) (N^2)/C1]);
Plant2 = tf([K2 0],[(L_t2+N^2*L_g2) (R_t2+N^2*R_g2) (N^2)/C2]);

[Wn1,Z1,P1] = damp(Plant1);
Wd1 = Wn1(1,:)*sqrt(1-Z1(1,:)^2);

[Wn2,Z2,P2] = damp(Plant2);
Wd2 = Wn2(1,:)*sqrt(1-Z2(1,:)^2);

% frequency vector used for all plots

freqT = linspace(40e3,2*pi*800e3,125e3);
f = freqT/2/pi;

[M_temp,P_temp] = bode(Plant1,freqT);
Mag_sim1 = 20*log10(abs(squeeze(mp2h(M_temp,P_temp))));
PH_sim1 = angle(squeeze(mp2h(M_temp,P_temp)))*180/pi;

[M_temp,P_temp] = bode(Plant2,freqT);
Mag_sim2 = 20*log10(abs(squeeze(mp2h(M_temp,P_temp))));
PH_sim2 = angle(squeeze(mp2h(M_temp,P_temp)))*180/pi;


figure(1);
```

```
set(gcf,'DefaultLineLineWidth',2.0);
subplot(211);
plot(f/1000,Mag_sim1,'-',f/1000,Mag_sim2,'--'); % divide by 1000 for kHz
ylabel('Magnitude (dB)');
legend('Generator 1','Generator 2')
axis([60 90 -40 40])
subplot(212);
plot(f/1000,PH_sim1,'-',f/1000,PH_sim2,'--');
ylabel('Phase (deg)'),xlabel('Frequency (kHz)');
axis([60 90 -180 180])

%% Experimental FRF

FRF = csvread('FRF-Data.csv');

figure(2)
set(gcf,'DefaultLineLineWidth',2.0);
subplot(211);
plot(FRF(:,1),FRF(:,2),'-',FRF(:,1),FRF(:,4),'--')
legend('Generator 1','Generator 2')
ylabel('Magnitude (dB)');
axis([60 90 -40 40])
subplot(212);
plot(FRF(:,1),FRF(:,3),'-',FRF(:,1),FRF(:,5),'--')
ylabel('Phase (deg)'),xlabel('Frequency (kHz)');
axis([60 90 -180 180])



%% Simulate Response OL Response
```

```
figure(3)
[y,t] = step(Plant1);
[Wn,zeta] = damp(Plant1);
Q_o = 1/(2*zeta(1,1))
plot(t*100,y);
ylabel('Amplitude (V)');
xlabel('Time (ms)')
set(gca,'XLim',[0 0.25])


figure(4)
step(Plant2)

a = 0.07;
% a = 0.383
w = 73e3;
% fs = 10*w;
fs = 800000;
nCyl = 900;
t = 0:1/fs:nCyl*1/w;
x = sin(2*pi*w*t);

sqw = square(2*pi*166*t+100);
sqw(find(sqw < 0)) = 0;
x_b = a*sin(2*pi*w*t).*sqw;

t_f = max(t);

figure(5)
```

```
title('Sinusoidal Input Signal');
plot(t, x_b)
xlabel('Time(s)');
ylabel('Amplitude (V)');
axis([0 0.012 -0.2 0.2]);

x_sim_ol = lsim(Plant1,x_b,t);
figure(6)
% Convert to milliseconds
plot(t*100, x_sim_ol, t*100, x_b);
%title('Plant 1 - Sinusoidal Burst Input Response');
xlabel('Time(ms)');
ylabel('Amplitude (V)');
legend('Output Signal','Input Signal')
set(gca,'XLim',[0 1.2])
set(gca,'XTick',(0:0.1:1.2))
axis([0 1.2 -2 2]);

%% Controller Design

figure(7)
h = rlocusplot(Plant1);
p = getoptions(h); % get options for plot
p.Title.String = ''; % change title in options
setoptions(h,p); % apply options to plot


% Choose gain value
CL_u = feedback(Plant1, 1);
[Wn,zeta] = damp(CL_u);
```

```
Q_u = 1/(2*zeta(1,1));
CL_1 = feedback(series(0.5,Plant1), 1);
[Wn,zeta] = damp(CL_1);
Q_1 = 1/(2*zeta(1,1));
CL_2 = feedback(series(1.5,Plant1), 1);
[Wn,zeta] = damp(CL_2);
Q_2 = 1/(2*zeta(1,1));

disp('Q_u ='),disp(Q_u)
disp('Q_1 ='),disp(Q_1)
disp('Q_2 ='),disp(Q_2)

figure(8)
% step(CL_1,CL_u,CL_2)
h = stepplot(CL_1,CL_u,CL_2);
p = getoptions(h); % get options for plot
p.Title.String = ''; % change title in options
p.YLabel.String ='Amplitude (V)';
setoptions(h,p); % apply options to plot
legend('K=0.5','K=1','K=1.5')

figure(9)
h = bodeplot(CL_1,CL_u,CL_2);
p = getoptions(h); % get options for plot
p.Title.String = ''; % change title in options
setoptions(h,p); % apply options to plot
legend('K=0.5','K=1','K=1.5')

% PID Control
```

```
load C_PID2.mat
figure(10)
h = rlocusplot(series(C_PID2, Plant1));
p = getoptions(h); % get options for plot
p.Title.String = ''; % change title in options
setoptions(h,p); % apply options to plot

load C_pi_2.mat
CL_PI = feedback(series(C_pi_2, Plant1),1);
[Wn,zeta] = damp(CL_PI);
Q_PI = 1/(2*zeta(2,1));
disp('Q_PI ='),disp(Q_PI)

figure(11)
h = stepplot(CL_PI);
p = getoptions(h); % get options for plot
p.Title.String = ''; % change title in options
p.YLabel.String ='Amplitude (V)';
setoptions(h,p); % apply options to plot
%legend('K=0.5','K=1','K=1.5')

figure(12)
h = bodeplot(CL_PI);
p = getoptions(h); % get options for plot
p.Title.String = ''; % change title in options
setoptions(h,p); % apply options to plot
%legend('K=0.5','K=1','K=1.5')
```

```
%% Simulate CL response

sqw = square(2*pi*166*t+100);
sqw(find(sqw < 0)) = 0;
%x_b = 1.414*sin(2*pi*w*t).*sqw;
x_b = sin(2*pi*w*t).*sqw;
x_b_rms = rmsrun(x_b);
t2 = linspace(0,max(t),length(x_b_rms));


figure(13) %rms of the signals
xs = lsim(CL_u,x_b,t);
xe = lsim(1/(1+series(1,Plant1)),x_b,t);
xs_rms = rmsrun(xs);
xe_rms = rmsrun(xe);
plot(t2,x_b_rms,t2,xs_rms,t2,xe_rms)
xlabel('Time(s)');
ylabel('Amplitude');
legend('set point','output','error')

figure(14)
plot(t*100,xs,'b',t*100,xe,'r',t*100,sqw,'g')
xlabel('Time(ms)');
ylabel('Amplitude (V)');
legend('output','error','set point')
set(gca,'XLim',[0 1.2])
set(gca,'XTick',(0:0.1:1.2))
axis([0 1.2 -1.25 1.25]);

figure(15)
```

```
xs = lsim(CL_PI,x_b,t);
xe = lsim(1/(1+series(C_PID1,Plant1)),x_b,t);
plot(t*100,xs,'b',t*100,xe,'r',t*100,sqw,'g')
xlabel('Time(ms)');
ylabel('Amplitude (V)');
legend('output','error','set point')
set(gca,'XLim',[0 1.2])
set(gca,'XTick',(0:0.1:1.2))
axis([0 1.2 -1.25 1.25]);
```

The following coded was created to calculate the running RMS average.

```
function [ x_rms ] = rmsrun( sig )
%UNTITLED Summary of this function goes here
%   Detailed explanation goes here
x_rms = NaN(size(sig));
for n = 151:length(sig)-151
  x_rms(n) = rms(sig(n-150:n+150));
end
end
```